ESCUELA POLITÉCNICA NACIONAL

FACULTAD DE INGENIERÍA MECÁNICA

DESIGN AND SIMULATION OF A BLENDED WING BODY (BWB) AIRFRAME FOR AN UNMANNED AERIAL VEHICLE (UAV) USING COMPUTATIONAL FLUID DYNAMICS (CFD).

PROYECTO PREVIO A LA OBTENCIÓN DEL TÍTULO DE INGENIERO MECÁNICO

JORGE AMÉRICO CISNEROS GALLEGOS

jorge.cisneros.gallegos@gmail.com

DIRECTOR: Ing. ESTEBAN ALEJANDRO VALENCIA TORRES, PhD

esteban.valencia@epn.edu.ec

CO-DIRECTOR: Ing. VÍCTOR HUGO HIDALGO DÍAZ, PhD (c)

victor.hidalgo@epn.edu.ec

Quito, noviembre 2015

DECLARACIÓN

Yo, Jorge Américo Cisneros Gallegos, declaro que el trabajo aquí descrito es de mi autoría; que no ha sido previamente presentado para ningún grado o calificación profesional; y, que he consultado las referencias bibliográficas que se incluyen en este documento.

La Escuela Politécnica Nacional, puede hacer uso de los derechos correspondientes a este trabajo, según lo establecido por la Ley de Propiedad Intelectual, por su Reglamento y por la normatividad institucional vigente.

_____

Jorge Américo Cisneros Gallegos

CERTIFICACIÓN

Certifico que el presente trabajo fue desarrollado por Jorge Américo Cisneros Gallegos bajo mi supervisión.

Ing. Esteban Valencia, PhD.
DIRECTOR DEL PROYECTO

Ing. Victor Hugo Hidalgo, PhD(c).
CO-DIRECTOR DEL PROYECTO

AGRADECIMIENTOS

Quiero agradecer a mi madre Georgina Esther y mi padre José Anibal por su amor y por guiarme siempre por el camino del bien, con concentración, inteligencia y sabiduría.

A toda mi familia, mis hermanos Gaby y José, mi padrino Diego, mis tíos y tías, primos y primas, que hacen de mi vida una vida llena de amor y alegría.

Agradecer particularmente a mi director y a mi co-director de esta tesis, Dr. Esteban Valencia e Ing. Victor Hidalgo, respectivamente, por sus consejos y por todo el conocimiento que tuvieron la buena voluntad y paciencia de transmitirme.

A mis amigos a lo largo de estos años de universidad por hacer de esta carrera llevadera y un tiempo inolvidable.

JORGE AMÉRICO CISNEROS GALLEGOS

DEDICATORIA

Para mi hermano José María, con todo el cariño a la distancia para que alcance sus sueños.

JORGE AMÉRICO CISNEROS GALLEGOS

CONTENTS

LIST OF FIGURES

LIST OF TABLES

NOMENCLATURE

SYMBOL	DESCRIPTION
α	Angle of attack
b	Span
c	Chord length
S	Projected planform area
λ	Taper ratio
V	Velocity
A	Axial force
D	Drag force
L	Lift force
M	Moment
N	Normal force
Re	Reynolds number
M	Mach number
p	Pressure
q	Dynamic pressure
Cp	Pressure coefficient
τ	Shear stress
Γ	Circulation
w	Induced velocity

Subscripts

∞	Freestream
i	Induced
eff	Effective
c	Chord length as reference length
r	Wing root
b	Bottom surface
t	Upper surface
$L = 0$	Zero lift

Acronyms

AC	Aerodynamic center

AR	Aspect ratio
AOA	Angle of attack
BL	Boundary layer
BLI	Boundary layer ingestion
BWB	Blended Wing body
CFD	Computational fluid dynamics
CG	Center of gravity
CP	Center of pressure
LE	Leading edge
MAC	Mean aerodynamic chord
MH	Martin Hepperle
NACA	National Advisory Committee for Aerodynamics
TE	Trailing edge
TL	Thorsten Lutz
UAV	Unmanned aerial vehicle
UAS	Unmanned aerial system

ABSTRACT

In recent years, the use of UAVs in different areas such as agriculture, surveillance, medicine and others, have contributed to the growth of these industries and have produced an overall positive economic impact in the society. In Ecuador, this technology is currently being used for agricultural and surveillance purposes. In the present work the aerodynamic design of a Blended Wing Body airframe to be used in a UAV for applications in agriculture, medicine, surveillance, cartography and other uses has been conducted. Two-dimensional aerodynamic and longitudinal stability analyses were performed with three airfoils to be used in the 3D design. The designed airframe was then tested via CFD using the Spalart-Allmaras turbulence model. The simulation results were validated by comparing them to similar works. The design process used in this thesis resulted in a preliminary airframe of near 50 kilograms of lift force.

Keywords: Blended Wing Body, CFD, Lift, Drag.

RESUMEN

En años recientes, se han utilizado UAVs en distintas áreas productivas como la agricultura, vigilancia, medicina y otras, permitiendo que estas industrias crezcan y se produzca un impacto económico positivo en la sociedad. En el Ecuador, esta tecnología está siendo utilizada en la agricultura y en vigilancia. En el presente trabajo, se realizó el diseño aerodinámico de un Fuselaje de Ala Integrada (BWB) para un dron con aplicaciones en los campos de la agricultura, medicina, vigilancia, cartografía y demás. Se realizaron análisis bidimensionales para las características aerodinámicas y para la estabilidad longitudinal de tres perfiles aerodinámicos utilizados en el diseño tridimensional. El fuselaje diseñado fue evaluado mediante Mecánica de Fluidos Computacional (CFD), con el modelo de turbulencia de Spalart-Allmaras. Los resultados de esta simulación fueron validados al compararlos con publicaciones similares. Al seguir el proceso de diseño utilizado en esta tesis, se obtuvo un fuselaje preliminar con capacidad de sustentación de 50 kilogramos de fuerza.

Palabras clave: Fuselaje de Ala Integrada, Mecánica de Fluidos Computacional, Sustentación, Arrastre.

1 INTRODUCTION

Ever since the beginning of the XX century, aerodynamics principles and effects around bodies has been a science with an increasing influence in multiple industrial fields. The experimental works conducted by the Wright brothers, which led to the first flight (or glide) back in 1902, showed the importance of the aerodynamic effects around a given geometry. Effectively, they conducted a large amount of tests with different airfoils and gliders until they succeeded in their dream of flying.
The automotive industry has also grown hand-by-hand with corresponding aerodynamic studies. The aerodynamic innovations from the Formula One industry, noticeably the most advanced field of automotive research, have reached the motorcar industry in every level, from everyday family cars to million-dollars super-sport cars, even to the heavy transporting lorries.
However extensive the application field of aerodynamics is, the aerospace industry is the one that has conducted the most investigations and experiments over the years. The present work focuses in this area of knowledge, seeking to solve and/or improve some of the techno-economic and social issues with an innovative answer that has been investigated recently, the *Blended Wing Body airframe for an Unmanned Aerial Vehicle*.
The BWB airframe configuration has been used in studies and prototypes for massive transport, proving to be an efficient solution for airplane design (Liebeck, 2004). These studies have established a starting point for more innovative applications, namely, for unmanned aerial vehicles.

1.1 MOTIVATIONS AND OPPORTUNITIES

There are three major motivations for the present work. These motivations have been adapted from spotted opportunities of development and application of the unmanned aerial technology.

In the last decade, unmanned aerial systems (UAS) have been applied to a wide range of industries with a global economic impact. The technological breakthroughs that have been achieved in the last decades have contributed to the technification of a different areas of production, such as: agriculture, medicine, security, vigilance, cartography among others.
Nowadays, there exists a wide variety of drones that are being currently used in agriculture for various purposes. They can be fitted with auxiliary systems such as multi-spectral cameras or fertilizer spraying devices, in order to scan plantations

looking for health problems and diseases, growth registry, selective spraying and more (AUVSI, 2013, p. 2). These technological solutions are expected to generate nearly 80% out of a $82 billion market due to new highly-skilled jobs, tax revenue and market share (Blanks, 2014, p. 50).
The implementation of autonomous systems in the industry of the U.S.A. is expected to have big economic and job generation impacts in that country, due to direct, indirect and induced effects of total spending in UAS. For the period 2015-2025, 103 776 new jobs are expected to be generated, of which 34 000 are high paying manufacturing jobs and 70 000 other jobs in the first three years. The application of UAS in public safety will generate $3.2 billion (AUVSI, 2013, p. 20).

The insertion of a country in the aerospace industry shows a very promising economic picture in the mid-and-long term. Ecuador saw this opportunity and has been seeking to develop this area of knowledge with numerous projects. In 2007, seven UAVs *Heron* were acquired from Israel at $20 million. These drones are used for surveillance tasks, such as border patrol and drug traffic control (ElUniverso, 2014). Recently, in 2013, the Ecuadorian government signed a technological agreement with Belarus in order to develop and produce UAVs in Ecuador (LaRepública, 2015). Furthermore, the Ecuadorian Air Force (FAE) has produced three UAVs locally, mainly made of carbon fibre and wood. It is expected that a serial fabrication will begin in 2016. They are currently being used for surveillance and monitoring purposes (Calero, 2014).
Currently, there is an undergoing technification of the agriculture. The use of drones with auxiliary multi-spectral cameras have helped in the coastal region of the country to improve a sugarcane plantation's production (Paspuel, 2014).
Other potential fields of application for unmanned systems in Ecuador are the oil industry (oil well monitoring), volcano monitoring, fauna surveillance (Galapagos), cartography, mining among many others.

Finally, the research of innovative technologies such as the Blended Wing Body (BWB) herein presented, is a goal that must be pursued by any academic institution of excellence such as the *Escuela Politécnica Nacional*. This institution has proposed various projects involving the integration of a BWB airframe with innovative propulsion technologies, such as: Boundary Layer Ingestion and Distributed Propulsion.

1.2 SCOPE

The present work is focused on establishing an approach on the aircraft development in the Faculty. As such, the model did not go through the process of optimization, iterations and resizing.
The main considered variables for the design where the location of the transitions between the different airfoils and the chord lengths of the selected aerodynamic profiles.
There were not considered any control surfaces, control and navigation equipment nor cabin sizing. These must be set in a further iteration of the optimization process.
As figure of merit, the lift force was studied, in correlation with an elliptical distribution for the wing loading.
The flight stage studied in this work is the cruise stage.

1.3 THESIS STRUCTURE

This work is divided into four additional chapters (other than the introduction).

The second chapter covers the Literature Research, where theoretical concepts are explained, covering the fields of aerodynamics, boundary layer and viscous effects and static stability analysis. The Blended Wing Body airframe and its characteristics are also portrayed in this chapter. These concepts will be later applied in the development of the different types of analysis herein performed.
The third chapter is about the 2D Airframe Performance Assessment, where two-dimensional concepts are applied to analyse the effects of the flow around the BWB. It begins with an explanatory section about the airfoil selection and the operating conditions used in the analysis. Then, the results of the aerodynamic performance and the static longitudinal stability analysis of the different airfoils are presented and discussed. It ends with a brief 2D analysis about a boundary layer ingestion system to be applied in the model.
The fourth chapter deals with the 3D Analysis, Numerical Methods and CFD, where the final 3D model of the BWB is defined and analysed. The design process begins with some design considerations taken from the Litterature Research, to establish a baseline configuration that accomplish with the requirements set by the operating conditions. Once obtained the final BWB model, a CFD analysis is conducted to obtain accurate results about the model characteristics.
The fifth chapter is where the Conclusions and Recommendations are presented.

Additionally, six appendices are available in this work:

1. Atmospheric Properties
2. Numerical Methods Applied in Aerodynamics
3. Navier-Stokes and Boundary Layer Equations
4. NACA 2412 experimental results
5. The XFOIL Program
6. CFD Simulation Process

1.4 LIST OF PUBLICATIONS

The results of this thesis have been presented in the following publications:

- *Parametric Study of a Distributed Propulsion System with Boundary Layer Ingestion for Unmanned Aerial Vehicles used for Agriculture and Mapping in the Andean Zone.*, Revista Politécnica, Escuela Politécnica Nacional, Quito, Sept. 2015, *Under evaluation*
- *III CONCURSO DE RECONOCIMIENTO A LA INVESTIGACIÓN UNIVERSITARIA ESTUDIANTIL, GALARDONES NACIONALES, CONVOCATORIA 2015*, Senescyt, Quito, July 2015, *Under evaluation*

2 LITERATURE RESEARCH

2.1 THEORETICAL AERODYNAMICS CONCEPTS

In the following sections, the basic concepts of aerodynamics are studied.

2.1.1 FORCES ON AERODYNAMIC BODIES

On an aerodynamic system, the interaction between the body and the air around it cause a generation of different forces and moments on the body. Particularly, these forces and moments are due to two sources: pressure distribution p and shear stress τ distribution over the body surface, which can be seen in figure 2.1. The pressure acts normal to the surface and the shear stress acts tangentially to it, as the surface geometry changes, so do p and τ (Anderson Jr., 1991, p. 16).

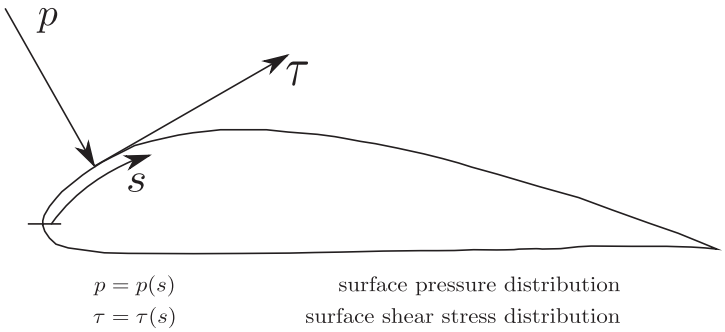

Figure 2.1: Illustration of surface pressure and surface shear stress on an aerodynamic body.

The resultant aerodynamic force R and moment M on the body can be found by integrating p and τ over the entire body. The aerodynamic resultant on an airfoil can be split into two sets of components, perpendicular and parallel to the freestream velocity V_∞ and perpendicular and parallel to the airfoil chord c. These two sets of components are (Anderson Jr., 1991, p. 17):

- – L: Lift: component of R perpendicular to V_∞
  – D: Drag: component of R parallel to V_∞
- – N: Normal force: component of R perpendicular to c
  – A: Axial force: component of R parallel to c

In aerodynamics, the lift and drag components are most widely used and are subject of more intensive studies, however, both sets can be associated in a geometrical

relation through the angle of attack α of the airfoil. The angle of attack is defined as the angle between V_∞ and c, hence it is also the angle between L and N and between D and A. The geometrical relation is portrayed in figure 2.2 and it is explicitly presented in equations 2.1a and 2.1b for lift and drag calculation, respectively (Anderson Jr., 1991, p. 17):

$$L = N\cos\alpha - A\sin\alpha \tag{2.1a}$$

$$D = N\sin\alpha + A\cos\alpha \tag{2.1b}$$

The normal and axial forces can also be written as a function of the lift and drag force and the angle of attack α, in equations 2.2a and 2.2b, respectively (Mulder, 2007, p. 156):

$$N = L\cos\alpha + D\sin\alpha \tag{2.2a}$$

$$A = D\cos\alpha - L\sin\alpha \tag{2.2b}$$

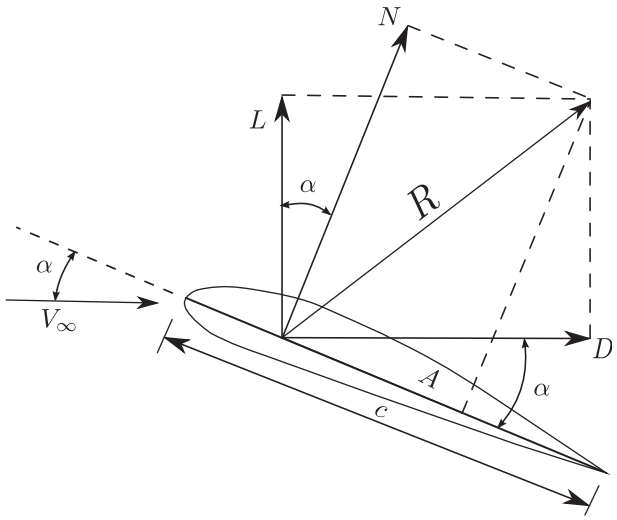

Figure 2.2: Aerodynamic resultant force and its components located at an arbitrary point.

The effects of pressure and shear stress distribution over an aerodynamic body can be visualized clearly while integrating them from the leading edge LE to the trailing edge TE to obtain the aerodynamic forces. In figure 2.3, a two dimensional airfoil is considered for such calculations, where the distance from the leading edge to an arbitrary point A on the upper surface is s_u and the distance to another arbitrary point B on the lower surface is s_l. The sub-indexes u and l represent magnitudes from the

upper and lower surfaces, respectively, for pressure and shear stress. The angle θ is the orientation of p and τ relative to the normal and axial forces respectively, and its sign convention is positive when measured clockwise from the vertical or the horizontal line. Considering an airfoil of a span equal to the unity, the forces obtained are per unit span, i.e. N' and A' . The forces on both surfaces of the body are given in equations 2.3a to 2.4b (Anderson Jr., 1991, p. 18).

$$dN'_u = -p_u ds_u \cos\theta - \tau_u ds_u \sin\theta \tag{2.3a}$$

$$dA'_u = -p_u ds_u \sin\theta + \tau_u ds_u \cos\theta \tag{2.3b}$$

$$dN'_l = -p_l ds_l \cos\theta - \tau_l ds_l \sin\theta \tag{2.4a}$$

$$dA'_l = -p_l ds_l \sin\theta + \tau_l ds_l \cos\theta \tag{2.4b}$$

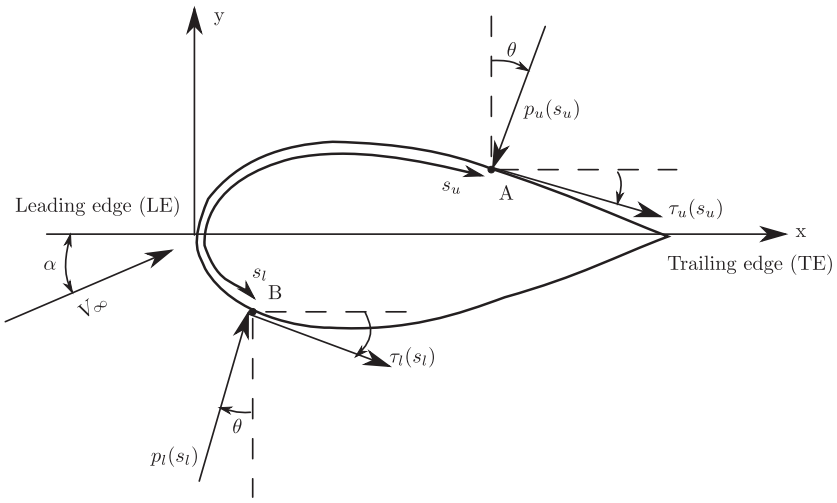

Figure 2.3: Nomenclature for the integration of pressure and shear stress distributions over a two-dimensional airfoil surface (Anderson Jr., 1991, p. 18).

The integral expressions for normal and axial forces per unit span are as follow, and expressions for lift and drag forces per unit span can be obtained through the

geometrical relation in equations 2.5a and 2.5b (Anderson Jr., 1991, p. 19).

$$N' = \int_{LE}^{TE} (p_u \cos\theta + \tau_u \sin\theta)\, ds_u + \int_{LE}^{TE} (-p_l \cos\theta - \tau_l \sin\theta) ds_l \tag{2.5a}$$

$$A' = \int_{LE}^{TE} (-p_u \cos\theta - \tau_u \sin\theta)\, ds_u + \int_{LE}^{TE} (-p_l \sin\theta + \tau_l \cos\theta) ds_l \tag{2.5b}$$

2.1.2 MOMENTS ON AERODYNAMIC BODIES, CENTER OF PRESSURE, AERODYNAMIC CENTER

As a result of the distributed loads that act on the aerodynamic body, a moment is generated. Nevertheless, this moment depends on the point about which moments are calculated and they depend on sign conventions. A simple and useful calculation is to take moments about the leading edge and considering positive moments those which tend to increase α (pitch up) and negative those which decrease α (pitch down). The elemental moment per unit span for upper and lower surfaces can be written as equations 2.6a and 2.6b (Anderson Jr., 1991, p. 19):

$$dM'_u = (p_u \cos\theta + \tau_u \sin\theta)\, x\, ds_u + (-p_u \sin\theta + \tau_u \cos\theta)\, y\, ds_u \tag{2.6a}$$

$$dM'_l = (-p_l \cos\theta + \tau_l \sin\theta)\, x\, ds_l + (p_l \sin\theta + \tau_l \cos\theta)\, y\, ds_l \tag{2.6b}$$

Integrating both equations from leading edge to trailing edge yields a total moment per unit span about the leading edge. The integral expression of such moment is given in equation 2.7 (Anderson Jr., 1991, p. 20).

$$\begin{aligned} M'_{LE} = &\int_{LE}^{TE} \left[(p_u \cos\theta + \tau_u \sin\theta)\, x - (p_u \sin\theta - \tau_u \cos\theta)\, y\right] ds_u \\ &+ \int_{LE}^{TE} \left[(-p_l \cos\theta + \tau_l \sin\theta)\, x + (p_l \sin\theta + \tau_l \cos\theta)\, y\right] ds_l \end{aligned} \tag{2.7}$$

The center of pressure is the point located on the chord at such a distance that the resultant of the distributed loads act effectively on the body. The resultant force R generate the same moment about the leading edge as the one produced by the distributed forces calculated at 2.5a. On an airfoil, the normal force N' must be located at a distance x_{cp} in such a way that all the moments are balanced out. An expression allowing to find the center of pressure x_{cp} is given in equation 2.8 (Anderson Jr., 1991, p. 29):

$$M'_{LE} = -x_{cp} \cdot N'$$
$$x_{cp} = -\frac{M'_{LE}}{N'} \tag{2.8}$$

The distance x_{cp} is the distance from the leading edge to the center of pressure. If the angle of attack is small, $L' \approx N'$, thus, the equation 2.8 can be rewritten in equation 2.9 in terms of the lift on the airfoil (Anderson Jr., 1991, p. 29).

$$x_{cp} = -\frac{M'_{LE}}{L'} \tag{2.9}$$

The force-and-moment system of an aerodynamic body can be defined by placing the resultant at any point on the body along with the moment about that point. It is common practice in aerodynamic bodies to place said point at the quarter chord, the moment about that point being known. The relation between moments at different points can be seen in the figure 2.4, and it is defined as shown in equation 2.10 (Anderson Jr., 1991, p. 30):

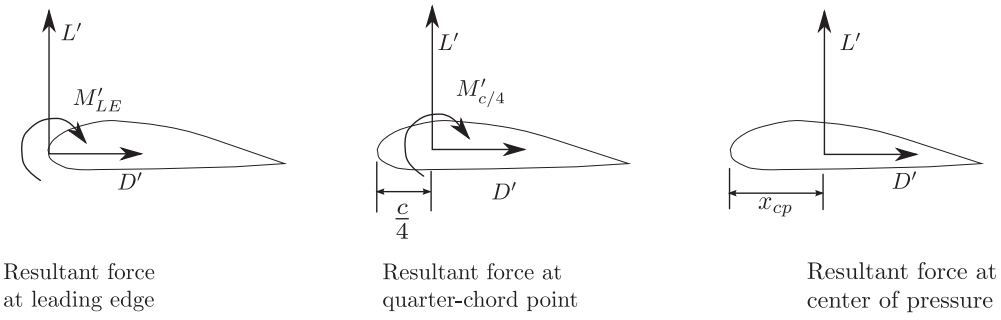

Figure 2.4: Equivalent force-and-moment systems on an airfoil.

$$M'_{LE} = -\frac{c}{4}L' + M'_{c/4} = -x_{cp}L' \tag{2.10}$$

It has been shown that forces and moments on aerodynamic bodies depend on the pressure and shear stress distributions, which are functions of the geometry of the body. Aerodynamics theory aim to calculate $p(s)$ and $\tau(s)$ for any given body shape and freestream conditions, in order to obtain the acting aerodynamic forces and moments (Anderson Jr., 1991, p. 20).

Another important point along the chord is the aerodynamic center, the point for which the moment is constant and does not depend from the lift force in the aerodynamic body. Generally, it is located close to 23% and 25% of the chord line behind the leading edge. This is the reason for finding the moments about the quarter

chord, since it gives an approximation of moment about the aerodynamic center for angles of attack up to 10°or so (Houghton, 2013, p. 44).

The method for finding the aerodynamic center is through the calculation of moments about an arbitrary point located at a distance a from the leading edge. Such method is explained in equation 2.11 (Houghton, 2013, p. 44).

$$M_a = M_{AC} - L \cdot (\frac{x_{AC}}{c} - \frac{a}{c}) \tag{2.11}$$

Differentiating 2.11 with respect to the lift force and applying the aerodynamic center definition (moment independent of lift) yields equation 2.12.

$$\frac{x_{AC}}{c} = \frac{a}{c} - \frac{d}{dL}(M_a) \tag{2.12}$$

The aerodynamic center position x_{AC} is found implicitly, by plotting M_a against L, measuring the slope of the curve and subtracting it from a/c.

A schematic representation summarizing the forces and moments acting on an aerodynamic body is presented in figure 2.5 (Houghton, 2013, p. 40).

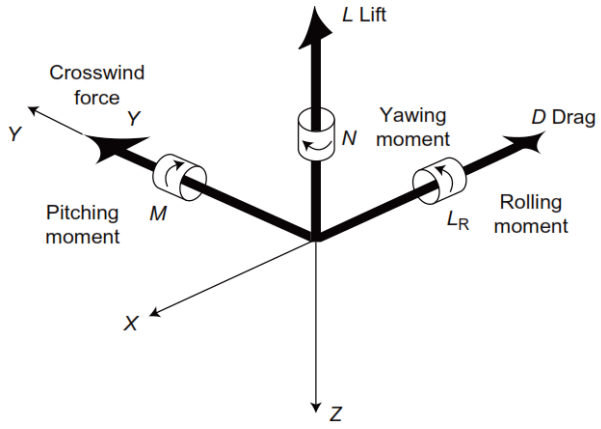

Figure 2.5: Systems of coordinates, forces and moments acting on a body (Houghton, 2013, p. 40).

2.1.3 AERODYNAMIC COEFFICIENTS

The dimensional analysis methods such as the Buckingham Pi Theorem (White, 1998, p. 286) & (Anderson Jr., 1991, p. 30), offer a very useful tool in aerodynamic studies, namely, the non dimensional coefficients for forces and moments.

The resultant force R on the aerodynamic body depend on five parameters: freestream velocity V_∞, freestream density ρ_∞, dynamic viscosity of the air μ_∞, a reference length of the body (chord length) c and the compressibility effects given by the speed of sound a_∞, yielding the functional relation given in equation 2.13 (Anderson Jr., 1991, p. 21).

$$R = f(\rho_\infty,\, V_\infty,\, \mu_\infty,\, c,\, a_\infty) \tag{2.13}$$

The non dimensional π products are the Reynolds number 2.14a, the Mach number 2.14b and a force coefficient 2.14c. This last coefficient can be multiplied by a number without losing its non dimensional characteristics (Anderson Jr., 1991, p. 34).

$$Re = \frac{\rho_\infty V_\infty c}{\mu_\infty} \tag{2.14a}$$

$$M = \frac{V_\infty}{a_\infty} \tag{2.14b}$$

$$\pi_3 = \frac{R}{\rho_\infty V_\infty^2 c^2} \tag{2.14c}$$

The dynamic freestream pressure can be defined as q_∞ in equation 2.15, and introducing this quantity in equation 2.14c, with S as the reference area, the resultant force coefficient can be computed as shown in equation 2.16 (Anderson Jr., 1991, p. 20).

$$q_\infty = \frac{1}{2}\rho_\infty V_\infty^2 \tag{2.15}$$

$$C_R = \frac{R}{\frac{1}{2}\rho_\infty V_\infty^2 c^2} = \frac{R}{q_\infty S} \tag{2.16}$$

The non dimensional force and moment coefficient can be obtained from equations 2.17a to 2.17e, with l as a reference length (Anderson Jr., 1991, p. 20).

$$C_L = \frac{L}{q_\infty S} \qquad \text{Lift coefficient} \tag{2.17a}$$

$$C_D = \frac{D}{q_\infty S} \qquad \text{Drag coefficient} \tag{2.17b}$$

$$C_N = \frac{N}{q_\infty S} \qquad \text{Normal force coefficient} \tag{2.17c}$$

$$C_A = \frac{A}{q_\infty S} \qquad \text{Axial force coefficient} \tag{2.17d}$$

$$C_M = \frac{M}{q_\infty S l} \qquad \text{Moment coefficient} \tag{2.17e}$$

2.1.4 AIRFOIL THEORY

The airfoil theory is the study of a section of a wing and the interaction between this aerodynamic surface with the flow around it(Roskam, 1997, p. 52). An airfoil is shown in figure 2.6 (Anderson Jr., 1991, p. 249):

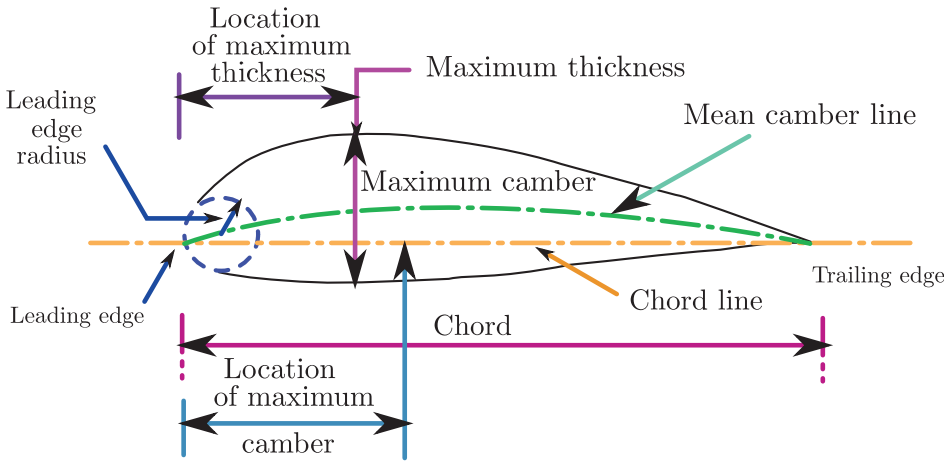

Figure 2.6: Airfoil terminology. Adapted from (Dynamic Flight, 2002).

2.1.4.1 Lift generation .

On aerodynamic bodies, the causes that produce the lifting force have been determined as the net imbalance of the surface pressure distribution around it. This imbalance of pressure in an airfoil, for example, determines another important concept in aerodynamics called circulation (Anderson Jr., 1991, p. 218).

The circulation concept has been used since the beginning of the XX century, and it is a kinematic property that depends on an arbitrarily chosen closed curve A and flow velocity V. It is defined as the negative of the line integral of velocity around the close curve. It can also be related to flow vorticity, the circulation is equal to the vorticity integrated over any open surface bounded by A. In aerodynamics studies, the circulation is considered positive in a clockwise direction. Both expressions of circulation are shown in equation 2.18 (Anderson Jr., 1991, p. 136).

$$\Gamma = -\oint_A \vec{V} \cdot d\vec{s} = -\iint_s (\vec{\nabla} \times \vec{V}) \cdot d\vec{s} \tag{2.18}$$

In figure 2.7, a lifting airfoil enclosed by a curve A is shown. The velocity field around the airfoil must be such that the circulation about A is finite. The concept of circu-

lation is used in the Kutta-Joukowski theorem and therein underlays its importance. This theorem states that on a two dimensional body, such as an airfoil, lift per unit span L' is directly proportional to the circulation around the body, as shown in equation 2.19 (Anderson Jr., 1991, p. 216).

$$L' = \rho_\infty V_\infty \Gamma \tag{2.19}$$

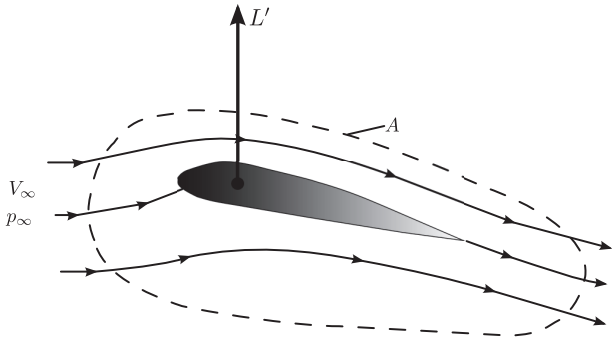

Figure 2.7: Circulation around a lifting airfoil.

The Kutta-Joukowski is an important observation, but for practical purposes, additional conditions for the lifting flow must be provided. Such conditions are called the Kutta conditions that state that for an airfoil at a given angle of attack, there is a single value of Γ for steady flow, i.e., flow leaving top and bottom surfaces of the airfoil at the trailing edge. Another condition is established for the behaviour of the flow at the trailing edge, by distinguishing two types of trailing edge geometry, finite angle an cusp. Both representations with the velocity at trailing edge can be seen in figure 2.8. For finite angle TE, point a is a stagnation point, and for cusp TE, the leaving flow velocity is equal in both magnitude and direction for top and bottom surfaces (Anderson Jr., 1991, p. 262).

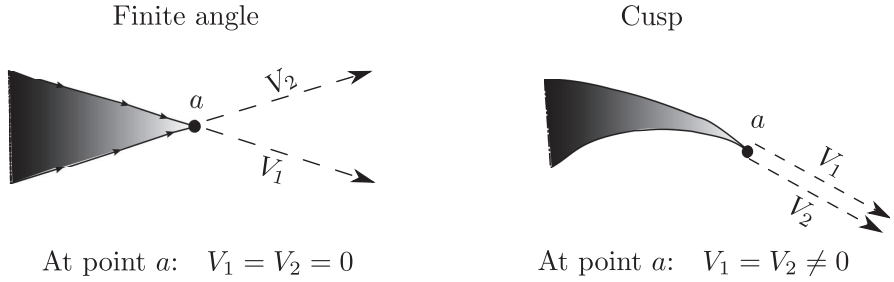

Figure 2.8: Finite angle (left) and cusp (right) configurations of trailing edge.

A vortex sheet of strength $\gamma(s)$ can be distributed around an airfoil, the Kutta condi-

tion applied at the trailing edge of this airfoil is as follows:

$$\gamma(TE) = 0$$

This condition, along the panel methods discussed in the appendices are a very useful tool for calculating lift on any two dimensional bodies and is used in numerous computational programs. The XFOIL program is a computational tool for airfoil aerodynamic assessment and design and it is widely used. This software uses the panel methods and the theory herein presented for calculation purposes. The panel methods and a more thorough description of the XFOIL program can be found in appendices B.2 and E, respectively.

2.1.4.2 NACA and reflex airfoils .

The National Advisory Committee for Aeronautics (NACA, predecessor of NASA) started the development of airfoils using the Langley variable-density wind tunnel in 1929. Ever since, the study of different families of airfoils by this institution has provided the aeronautical field with a large database of publicly available airfoils, called the NACA airfoils. Their geometries are obtained by combining a mean line and a thickness distribution, both of them vary for the different families (Abbot I. H., 1945, p. 2).

The first set of NACA airfoils were the four-digit series, where the first digit is the maximum camber, the second digit is the location of maximum camber along the chord and the last two digits give the maximum thickness, all expressed in hundredths of chord (Anderson Jr., 1991, p.250). An example of this airfoil is the NACA 2412, used in the Cessna 150 airplane (Anderson Jr., 1991, p. 251). This series have good stall characteristics, small center of pressure movement and roughness has little effect on drag. However, these airfoils present high pitching moment and low maximum lift coefficient (Marzocca, 2003, p. 5).

The second family is the five-digit series, where the first digit multiplied by $3/2$ indicates the design lift coefficient in tenths. The design lift coefficient is the theoretical lift coefficient at an angle of attack such tat the slope of the mean cmaber line at the leading edge is parallel to the freestream velocity. The two following digits divided by 2 give the location of the maximum camber along the chord from the leading edge and the final two digits represent the maximum thickness, all in hundredths of chord (Anderson Jr., 1991, p. 250). They possess a higher lift and lower moment coefficients than the four-digit series, however they also produce an increase in drag (Marzocca, 2003, p.5).

The 6-series is one of the most widely used of NACA airfoils, they are the laminar flow airfoils developed during World War II. The first digit identifies the series, the second gives the location of the minimum pressure in tenths of chord from the leading edge, the third digit represents the design lift coefficient in tenths and the last digits, in hundredths of chord, give the maximum thickness of the airfoil. War aircraft such as the famous General Dynamics F-16 use the 6-series NACA 64-204 (Anderson Jr., 1991, p. 251). These airfoils are optimized for high speed, high lift and very low drag over a small range of operating conditions. However, outside the optimum conditions, drag increases largely (Marzocca, 2003, p. 5).
There exist the 1-series, 7-series and modifications of the four and five-digit series, however, their application is very rare. The nomenclature and characteristics of these series can be found in ref. (Abbot I. H., 1945) & (Abbot I.H., 1959). The NACA airfoils are the most widely used and also the better studied, however, any aeronautic company such as BOEING, designs and uses its own airfoils.

There is a type of airfoil that has a trailing edge geometry called reflex. This means that the mean camber line goes from a negative slope to a positive slope near the trailing edge, curving up the airfoil. A schematic representation of a MH45 reflex airfoil with its reflexed trailing edge is shown in figure 2.9. The camber line for such an airfoil can be obtained with a cubic camber line (Houghton, 2013, p. 245). They are used mostly in tailless aircraft to increase stability (almost 0 pitching moment) (Abbot I.H., 1959, p. 116).

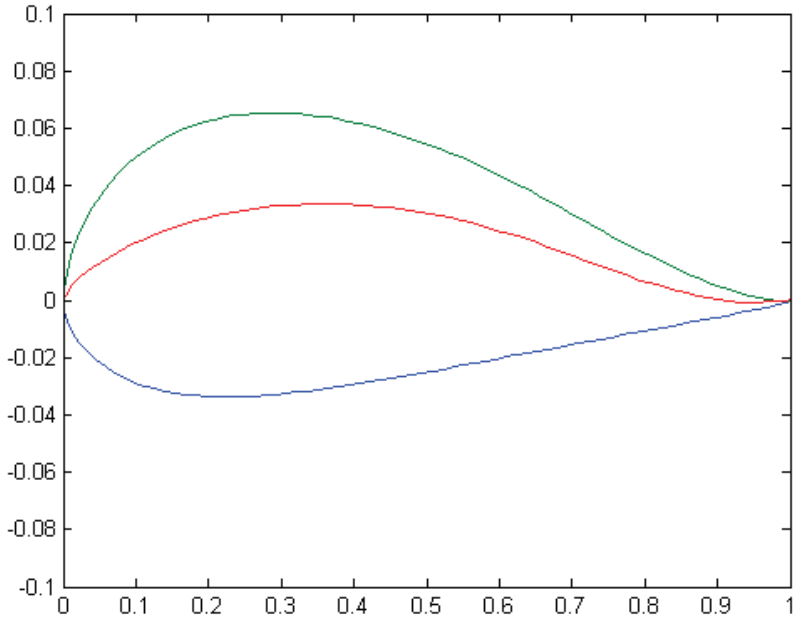

Figure 2.9: Relfexed trailing edge, the thickness is exaggerated in order to show the change of slope of the mean camber line (in red). The upper surface is shown in green and the bottom one is in blue.

2.1.5 FINITE WING THEORY

The difference between wing theory and airfoil theory is the consideration of a wing of finite span. In airfoil theory, it was assumed that the airfoil had an infinite span. However, all aircrafts have wings of finite span, for which a number of different effects occur around it.

2.1.5.1 Definition of wing properties .

The geometric nomenclature of a typical, straight, tapered wing planform of span b is shown in fig. 2.10. The wing planform area S is the projection of the wing onto a plane of reference, usually, the wing root chord plane. For this type of aircraft, the area S can be defined as (Roskam, 1997, p. 96):

$$S = \frac{b}{2}(c_r + c_t) \tag{2.20}$$

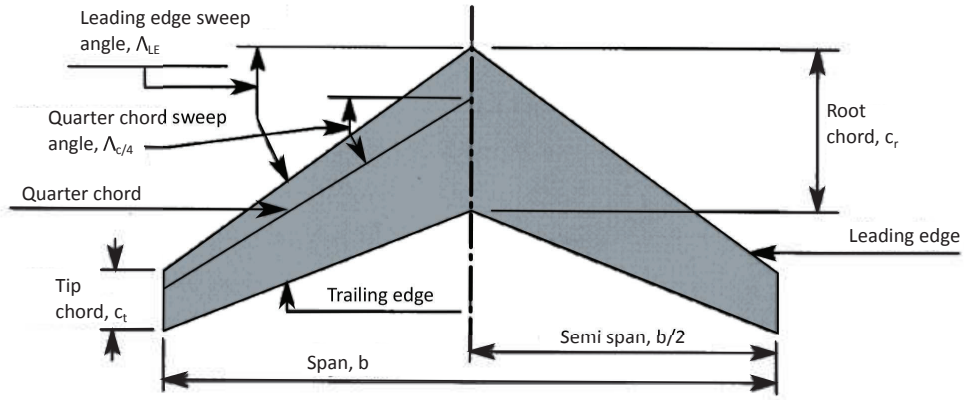

Figure 2.10: Wing nomenclature (Roskam, 1997, p. 95).

The wing aspect ratio AR and the taper ratio λ are defined as (Roskam, 1997, p. 96):

$$AR = \frac{b^2}{S} \tag{2.21}$$

$$\lambda = \frac{c_t}{c_r} \tag{2.22}$$

In order to use the aerodynamic coefficients defined in previous sections, a reference length is needed, the mean geometric chord is defined as $\overline{c}$ (Roskam, 1997, p. 96):

$$\overline{c} = \frac{2}{S}\int_0^{b/2} c^2 dy \tag{2.23}$$

There are additional geometric characteristics that are involved in wing design, geometric twist and aerodynamic twist (Anderson Jr., 1991, p. 324):

- *Geometric twist*: when the local wing section's angle of attack changes from the wing root to the tip. If the tip is at a lower α than the root, the wing has washout; if the tip is at a higher α than the root, the wing has washin.
- *Aerodynamic twist*: in a wing, when airfoil sections vary along the span, i.e., different values of zero lift angle $\alpha_{L=0}$.

2.1.5.2 Downwash and induced drag .

The net pressure imbalance between the top and bottom surface is what creates lift around a body. However, in a three-dimensional scenario, the flow near the wing tips tend to curl around them, being forced from the high pressure on the bottom surface

to the low pressure region on top. This results in a spanwise component of flow from the root toward the tip, establishing a circulatory motion which trails downstream of the wing, a trailing vortex (Anderson Jr., 1991, p. 316). This effect is illustrated in figure 2.11

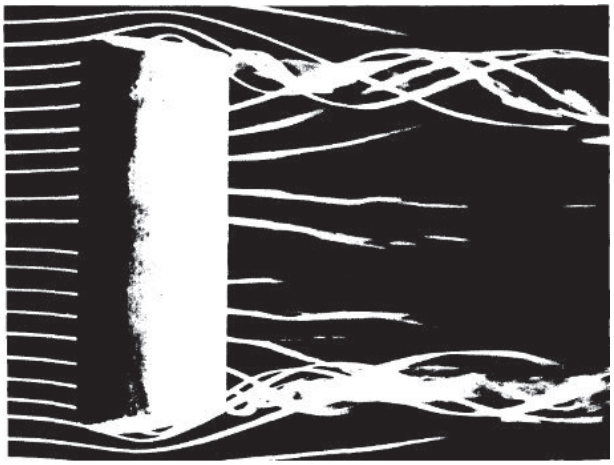

Figure 2.11: Wing tip vortices from a rectangular wing (Anderson Jr., 1991, p. 317).

A small downward component of air velocity is induced by these vortices, this phenomenon is called downwash, denoted w. The downwash is combined with the freestream velocity V_∞ and produce a local relative wind, canted downward in the vicinity of each airfoil section of the wing. In figure 2.12, this occurrence is illustrated. The local relative wind is inclined below the freestream direction by the induced angle of attack, α_i (Anderson Jr., 1991, p. 318).

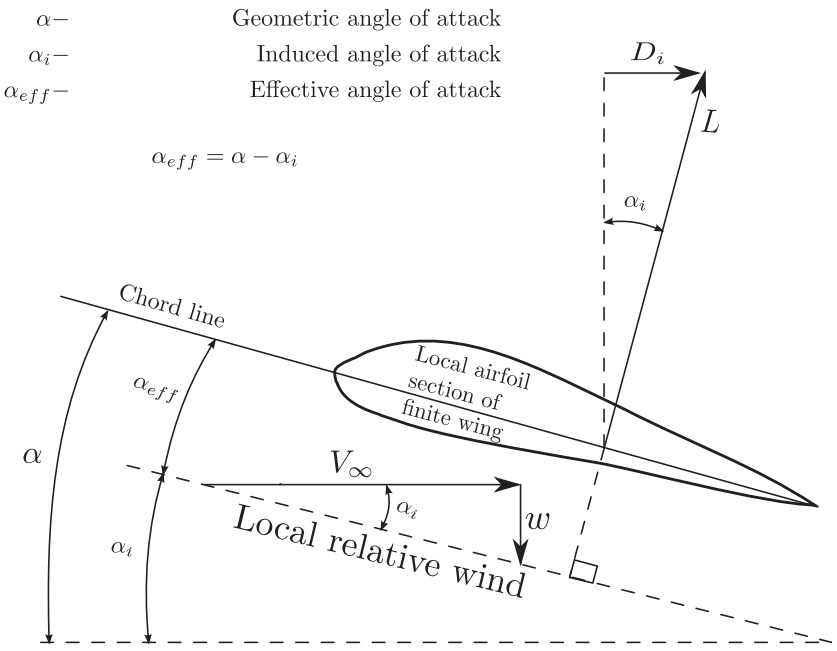

Figure 2.12: Effect of downwash on the local flow over an airfoil.

The local airfoil section is orientated at an angle of attack α, however, the actual angle of attack seen by the local airfoil is called the effective angle of attack α_{eff}, defined as:

$$\alpha_{eff} = \alpha - \alpha_i \tag{2.24}$$

The local lift vector is perpendicular to the relative wind, and it is inclined behind the vertical by α_i. A component of the lift is then created in the direction of V_∞, this component is the induced drag D_i.
The induced drag is then a consequence of the trailing vortex, a three-dimensional effect around wings, which reduces the aerodynamic performance of a wing from that of the equivalent airfoil. A larger wing aspect ratio (AR) has then better performance of a wing with a lower aspect ratio(Houghton, 2013, p. 302).

2.1.5.3 Laws of vortex motion .

A vortex filament is a line or a curve composed of an infinity of vortices of constant strength Γ, as shown in figure 2.13. The strength is equal to the product of the vorticity and cross sectional area of the filament (or tube). As a consequence, a vortex line or tube cannot end in the fluid but it must form a closed loop or terminate in a discontinuity such as a solid body or surface. This is known as the Helmholtz's

theorem of vortex continuity (Houghton, 2013, p. 275).

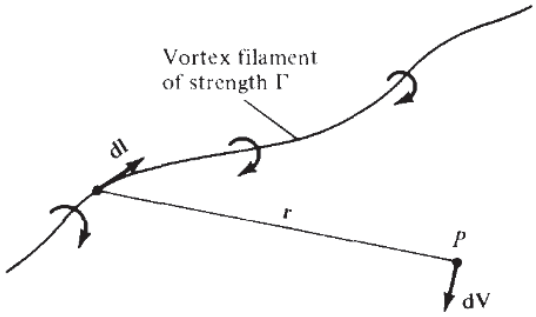

Figure 2.13: Vortex filament and the induced velocity around it (Anderson Jr., 1991, p. 321).

The vortex filament induces a velocity field around it, defined in equation 2.25, known as the Biot-Savart law, one of the most fundamental relations in the theory of inviscid, incompressible flow (Anderson Jr., 1991, p. 321).

$$d\vec{V} = \frac{\Gamma}{4\pi}\frac{\vec{dl} \times \vec{r}}{|\vec{r}|^3} \tag{2.25}$$

The velocity induced at any point can be found via eq. 2.25. For semi-infinite vortices, the velocity induced is related to the vortex circulation Γ and the distance h from the point to the filament, and the velocity can be written as (Anderson Jr., 1991, p. 323):

$$V = \frac{\Gamma}{4\pi h} \tag{2.26}$$

The Hemholtz's theorems are, in summary (Anderson Jr., 1991, p. 323):

- The strength of a vortex filament is constant along its length.
- A vortex filament must extend to the boundaries of the fluid or form a closed path. It cannot end in a fluid.

2.1.5.4 Lift distribution .

As the local sections of a wing varies along the spanwise direction y (local chord c, local angle of attack α and local airfoil shape), so do the lift per unit span L' and the circulation Γ. The lift goes from zero lift at the tips ($y = -b/2$ and $y = b/2$) due to

pressure equalization from the bottom to the top surfaces and reaches a maximum at the center of the wing ($y = 0$), as shown in figure 2.14.

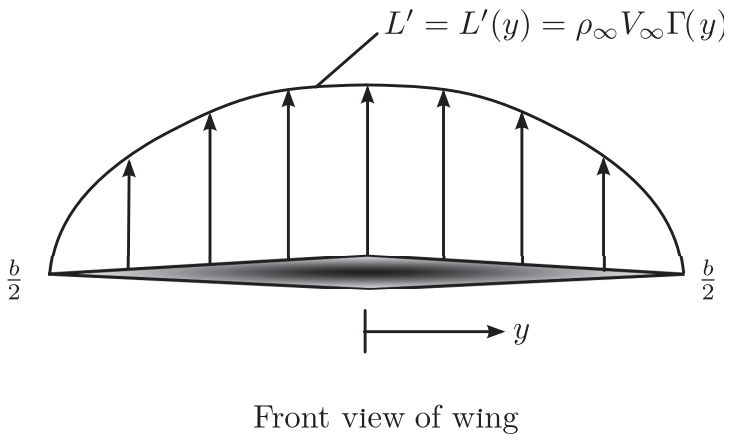

Figure 2.14: Schematic representation of the lift distribution in spanwise direction.

The main objective in a three-dimensional analysis is to obtain the induced drag, total lift and lift distribution for a finite wing (Anderson Jr., 1991, p. 324).

A theory was developed by Ludwig Prandtl, during the WWII for preliminary calculations of wing characteristics. It consists in fixing a vortex filament of strength Γ to a location in a flow (bound vortex), experiencing a force $L = \rho_\infty V_\infty \Gamma$. This bound vortex is combined with a free vortex moving with the fluid elements throughout a flow. A finite wing of span b can be modelled as a bound vortex with free-trailing vortices from the tips to infinity, in accordance to Helmholtz's theorem. This combination of vortices is called a horseshoe vortex, as can be seen in figure 2.15 (Anderson Jr., 1991, p. 324).

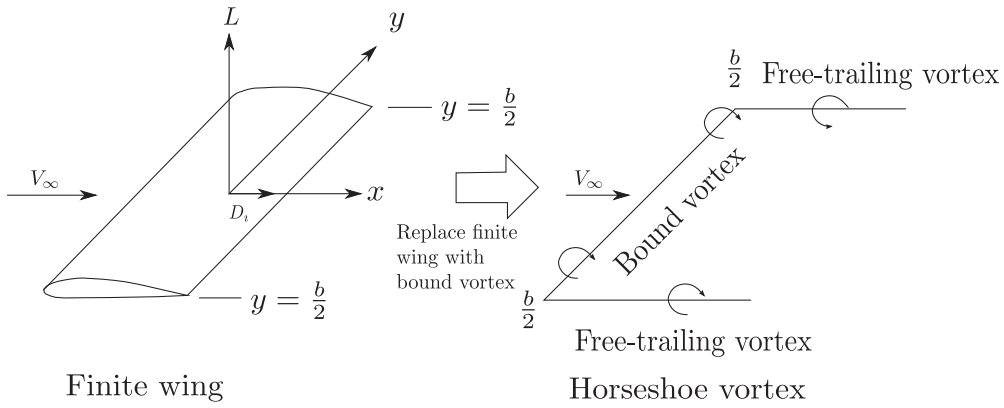

Figure 2.15: Representation of a finite wing replaced with a horseshoe vortex.

The downward velocity w induced by the bound semi-infinite vortices is the contribution from the left trailing vortex and the right trailing vortex. The velocity can be written as, from eq. 2.26:

$$w(y) = -\frac{\Gamma}{4\pi(b/2+y)} - \frac{\Gamma}{4\pi(b/2-y)} = -\frac{\Gamma}{4\pi}\frac{b}{(b/2)^2 - y^2} \tag{2.27}$$

A singularity is obtained at the tips, where the downwash reaches an infinite value. The solution to this problem is to superimpose a large number of horseshoe vortices coincident along a single line, called the lifting line. In figure 2.16, a superposition of thee vortices of strengths $d\Gamma_1$. $d\Gamma_2$ and $d\Gamma_3$, from A to F, B to E and C to D, respectively. In each portion of the lifting line, the strengths of the vortices are summed, which makes the circulation vary along the lifting line (Anderson Jr., 1991, p. 427).

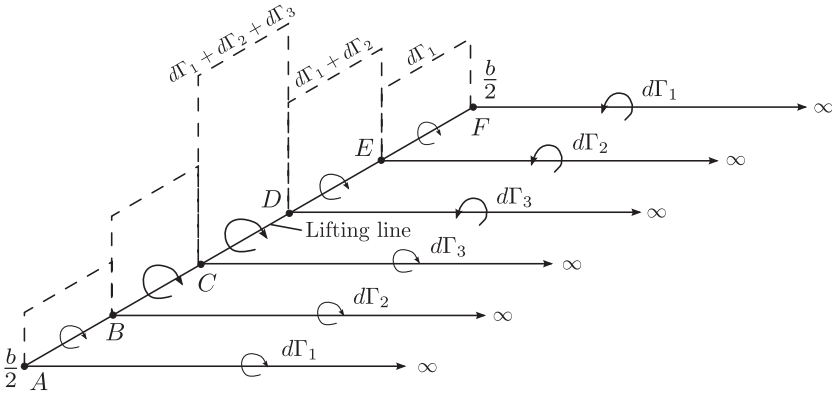

Figure 2.16: Superposition of three horseshoe vortex along the lifting line.

If the number of superimposed vortices increases to infinity, with each vortex varying in strength of $d\Gamma$, the distribution of $\Gamma(y)$ becomes a continuous distribution with Γ_0 the value of circulation at the origin. Additionally, as can be seen in figure 2.17, the trailing vortices become a continuous vortex sheet parallel to V_∞ (Anderson Jr., 1991, p. 327).

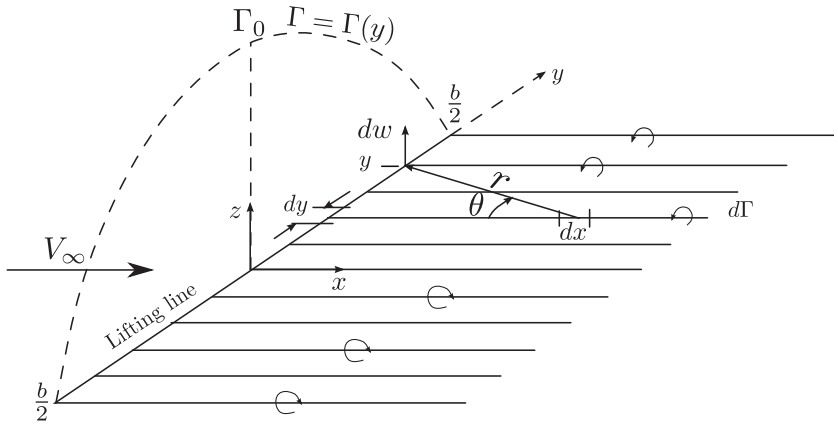

Figure 2.17: Superposition of infinite horseshoe vortex along the lifting line.

In figure 2.17, a small segment of the lifting line dy located at the coordinate y is shown. The circulation at y is $\Gamma(y)$ and the variation in circulation over the segment dy can be written as $d\Gamma = (d\Gamma/dy)dy$. As observed in fig. 2.16, the strength of the trailing vortex at y must be equal to the change in circulation $d\Gamma$ along the lifting line. An arbitrary point y_0 along the lifting line and a trailing vortex of strength $d\Gamma$ which intersects the lifting line at y are also shown in figure 2.17. Any segment dx of the trailing vortex induces a velocity at y_0, consistently with the Biot-Savart law (eq. 2.25). The velocity dw induced at y_0 by a the entire semi-infinite trailing vortex located at y is (Anderson Jr., 1991, p. 327):

$$dw = -\frac{(d\Gamma/dy)dy}{4\pi(y_0 - y)} \tag{2.28}$$

The total velocity w induced at y_0 by the entire trailing vortex sheet is the summation of dw (eq. 2.28) over the wing span (Anderson Jr., 1991, p. 328):

$$w(y_0) = -\frac{1}{4\pi}\int_{-b/2}^{b/2} \frac{(d\Gamma/dy)dy}{y_0 - y} \tag{2.29}$$

By replacing of a wing with the model of a lifting line with a constantly varying circulation $\Gamma(y)$, the expression for the downwash along the lifting line has been obtained. However, in order to calculate and obtain the circulation distribution for a given finite wing, with its corresponding total lift and induced drag, additional considerations must be made.

Assuming that the local airfoil section of a finite wing (shown in fig. 2.12) is located at the arbitrary spanwise coordinate y_0, the induced angle of attack α_i can be written

as (Anderson Jr., 1991, p. 328):

$$\alpha_i(y_0) = -\arctan\left(\frac{-w(y_0)}{V_\infty}\right) = -\frac{w(y_0)}{V_\infty} \tag{2.30}$$

The induced angle of attack is generally a small angle, since w is much smaller than V_∞ and thus, the simplification made in eq. 2.30 is possible. Furthermore, eq. 2.28 can be substituted in 2.30 as follows (Anderson Jr., 1991, p. 329):

$$\alpha_i(y_0) = -\frac{1}{4\pi V_\infty}\int_{-b/2}^{b/2}\frac{(d\Gamma/dy)dy}{y_0 - y} \tag{2.31}$$

The geometric angle of attack is the sum of the effective angle plus the induced angle of attack. In eq. 2.32, the effective angle is expressed in terms of the circulation and the induced angle in terms of an integral containing $d\Gamma/dy$. This integro-differential equation is known as the fundamental equation of Prandtl's lifting-line theory (Anderson Jr., 1991, p. 330).

$$\alpha(y_0) = \frac{\Gamma(y_0)}{\pi V_\infty c(y_0)} + \alpha_{L=0}(y_0) + \frac{1}{a\pi V_\infty}\int_{-b/2}^{b/2}\frac{(d\Gamma/dy)dy}{y_0 - y} \tag{2.32}$$

Three main aerodynamic characteristics of a finite wing can be obtained from eq. 2.32: the lift distribution (2.33a), the total lift force (2.33b) and coefficient (2.33c) and the total induced drag force (2.33d) and coefficient (2.33e) (Anderson Jr., 1991, p. 330).

$$L'(y_0) = \rho_\infty V_\infty \Gamma(y_0) \tag{2.33a}$$

$$L = \int_{-b/2}^{b/2} L'(y)dy = \rho_\infty V_\infty \int_{-b/2}^{b/2}\Gamma(y)dy \tag{2.33b}$$

$$C_L = \frac{L}{q_\infty S} = \frac{2}{V_\infty S}\int_{-b/2}^{b/2}\Gamma(y)dy \tag{2.33c}$$

$$D_i = \int_{-b/2}^{b/2} L'(y)\alpha_i(y)dy = \rho_\infty V_\infty \int_{-b/2}^{b/2}\Gamma(y)\alpha_i(y)dy \tag{2.33d}$$

$$C_{D,i} = \frac{D_i}{q_\infty S} = \frac{2}{V_\infty S}\int_{-b/2}^{b/2}\Gamma(y)\alpha_i(y)dy \tag{2.33e}$$

The solution of eq. 2.32 yields the distribution of the circulation around a wing, which is used to obtain the aerodynamic characteristics of a wing. A good approximation of wing load for symmetric flight is the elliptic distribution for circulation, where the spanwise variation in circulation is represented by a semi-ellipse with the span as the major axis and the circulation at mid-span Γ_0 as the semi-minor axis. The circulation

distribution is (Houghton, 2013, p. 302):

$$\Gamma(y) = \Gamma_0 \sqrt{1 - \left(\frac{2y}{b}\right)^2} \tag{2.34}$$

The downwash for elliptic distribution can be found using eq. 2.29. The variation of lift in the spanwise direction $d\Gamma/dy$ is (Anderson Jr., 1991, p. 331):

$$\frac{d\Gamma}{dy} = -\frac{4\Gamma_0}{b^2} \frac{y}{\sqrt{1 - 4y^2/b^2}} \tag{2.35}$$

Substituting eq. 2.35 into eq. 2.29, with the corresponding mathematical simplifications (see (Anderson Jr., 1991, p. 331) or (Houghton, 2013, p. 304)), the downwash distribution is found constant over the span for an elliptical lift distribution (Anderson Jr., 1991, p. 332):

$$w(y) = w = -\frac{\Gamma_0}{2b} \tag{2.36}$$

The total lift for elliptic distribution can be calculated from eq. 2.33b, yielding (Houghton, 2013, p. 303):

$$L = \frac{\rho_\infty V_\infty \Gamma_0 \pi b}{4} \tag{2.37}$$

Thus, the circulation in the origin is:

$$\Gamma_0 = \frac{4L}{\rho_\infty V_\infty \pi b} = \frac{2V_\infty S C_L}{b\pi} \tag{2.38}$$

The induced angle of attack can also be found from eq. 2.30:

$$\alpha_i = -\frac{w}{V_\infty} = \frac{\Gamma_0}{2bV_\infty} \tag{2.39}$$

Or, in terms of lift:

$$\alpha_i = \frac{SC_L}{\pi b^2} = \frac{C_L}{\pi AR} \tag{2.40}$$

The induced drag coefficient is obtained from eq. 2.33e:

$$C_{D,i} = \frac{C_L^2}{\pi AR} \tag{2.41}$$

The aspect ratio (eq. 2.21) is a very useful geometric definition. The induced drag is inversely proportional to aspect ratio, therefore, to minimize induced drag, a high aspect ratio is desired. However, structural requirements must be met, so a balance

point between aerodynamics and structure must be reached (Anderson Jr., 1991, p. 325).

The general lift distribution for circulation can be found in (Anderson Jr., 1991, p. 331) & (Houghton, 2013, p. 304).

2.2 BOUNDARY LAYER AND VISCOUS EFFECTS

The boundary layer is a thin region adjacent to the surface of a body moving in a fluid where the flow is retarded due to the friction between the solid region and the fluid. This effect is caused by an important property of the fluid called viscosity which has an enormous influence on drag and heat transfer (Anderson Jr., 1991, p. 712). It can be also defined as the region where viscous action predominates. A schematic representation of the boundary layer around an aerodynamic body is given in figure 2.18 (Houghton, 2013, p. 479).

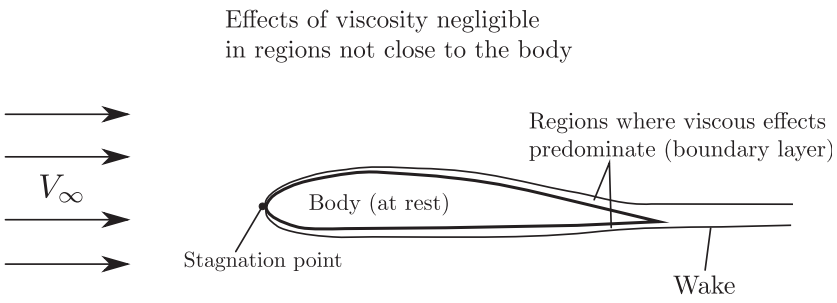

Figure 2.18: Boundary layer around a moving aerodynamic body.

In its conception, the boundary layer definition was used to reduce the Navier-Stokes equations into a set of real-flow equations, called the boundary layer equations, which are presented in appendix C. A difference is then made between inviscid flow, for which the theory of velocity potential is valid, and viscous flows, where the fluid viscosity and its effects are of major importance (Houghton, 2013, p. 479).

2.2.1 FLOW SEPARATION

The flow over an airfoil creates lift via a pressure difference between the upper and bottom surfaces of the body. On the forward section of an airfoil, the increasing velocity of the flow generates a decreasing pressure with distance, which helps the boundary layer to remain attached to the body. This pressure gradient is called *favourable*, as can be seen in figure 2.19. On the rear section of the airfoil, the air velocity decreases and pressure increases downstream. This is called an *adverse*

pressure gradient. The boundary layer particles have to endure the increasing pressure and, if they do not have enough energy to reach the trailing edge, they will separate from the surface, creating a *wake*. A turbulent boundary layer possesses more energy and remain attached over larger distances (Roskam, 1997, p.40).

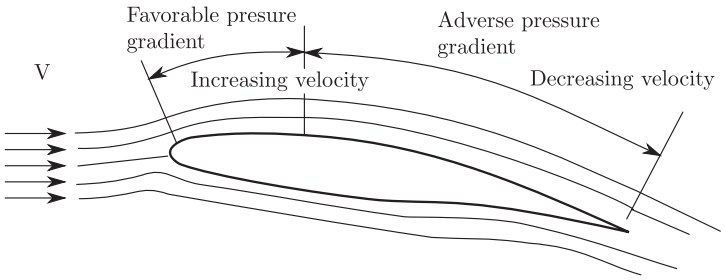

Figure 2.19: Velocity and pressure variation over an airfoil (Roskam, 1997, p. 40).

The separation will occur at a point where the velocity gradient at the surface is zero, due to the slowing effect of viscous shear stress at the wall. The separation on the rear half of an airfoil increases the thickness of the wake flow. The pressure drag of the airfoil increases. Separation may also occur not far downstream if the angle of attack is large enough. The separation herein generates a large wake over the airfoil and greatly reduces the area of low pressure near the leading edge, and consequently, the lift also reduces. This type of separation is called *stall* (Houghton, 2013, p. 499).

2.2.2 DRAG

The drag force or total drag is the force in the direction of the freestream and opposed to the movement. There are many contributions to total drag, they can be classified into two categories, *pressure* and *skin-friction* drag (Houghton, 2013, p. 48).

Skin-friction drag is generated by viscosity effects and it acts tangentially at all points on the body surface. Since it is directly involved with viscosity, this type of drag can only be computed with viscous theory. It has a component aligned with but opposing the freestream flow. The total effect of these components, integrated over the entire surface of the body is the skin-friction drag (Houghton, 2013, p. 48).

The pressure drag is the effect of the flight-path components of the forces generated by the pressure acting on the airfoil surfaces. This type of drag is the summation of

induced drag, wave drag and form drag (Houghton, 2013, p. 49).

The induced drag is a three-dimensional effect due to the downwash. It is further explained in section 2.1.5.2.
Wave drag is the drag associated with the formation of shock-waves in high-speed flight.
Form drag, or boundary-layer pressure drag, is caused by the difference between the pressure distribution over a body in viscous flow and that in an inviscid, ideal flow. The summation of the forces on the leading edge, the upper surface and the trailing edge results in an overall rearward force, the form drag.
Profile drag is the sum of the skin-friction and the form drags (Houghton, 2013, p. 50).

2.3 STATIC STABILITY ANALYSIS

Assumptions have to be made in order to establish correct reference frames for the stability analysis. These assumptions are (Mulder, n.d., p. 1):

- The Earth's curvature is negligible.
- No Coriolis acceleration is accounted from Earth's rotation.
- The aircraft has constant mass and it is a rigid symmetric body.
- Gyroscopic effects due to rotating masses (like turbines and so on) are ignored.
- Turbulence and gusts are ignores, a constant wind is considered.

2.3.1 THE VEHICLE REFERENCE FRAME

The aircraft reference frame F_r is used, which is a left-handed orthogonal axis system, generally used by manufacturers and annalists for specifying the location of important parts of the aircraft. A representation of this reference frame is shown in fig. 2.20. The X_r axis is fixed parallel to the plane of symmetry and it points to the rear of the aircraft. The Y_r axis is perpendicular to the plane of symmetry, it points to the left. Finally, the Z_r axis is perpendicular to the $)_r X_r Y_r$ plane and it points upwards (Mulder, 2007, p. 32).

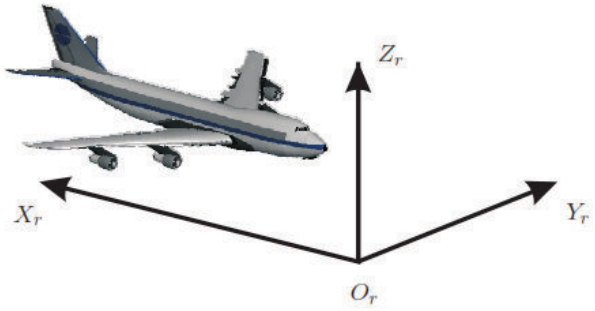

Figure 2.20: Aircraft reference frame F_r(Mulder, 2007, p. 32).

2.3.2 LOCATION OF METACENTRES ON AN AIRFOIL

As it has been shown in precedent sections, the moment coefficient and the slope of the moment-α depend both on the angel of attack and on the selected reference point. In fact, the moment coefficient about an arbitrary point (x_2, z_2) can be found as a function of a known moment coefficient about a point (x_1, z_1) for some angle of attack, as shown in equation 2.42, using F_r coordinates (Mulder, 2007, p. 157).

$$C_{m_{(x_2,z_2)}} = C_{m_{(x_1,z_1)}} + C_N \frac{x_2 - x_1}{c} - C_A \frac{z_2 - z_1}{c} \tag{2.42}$$

The resultant force can also be written as a nondimensional coefficient C_R (equation 2.43). The line of action of the resultant follows the angle χ_1 (equation 2.44), all the points on this line have $C_m = 0$. The point where the line of action crosses the chord is the center of pressure, at x_{cp}. The center of pressure is then the point where the distributed forces are applied. It can be found with equation 2.45 by knowing the moment about an arbitrary point (x_1, z_1) on the airfoil (Mulder, 2007, p. 169).

$$C_R = \sqrt{C_L^2 + C_D^2} = \sqrt{C_N^2 + C_A^2} \tag{2.43}$$

$$\chi_1 = \arctan \frac{C_A}{C_N} \tag{2.44}$$

$$C_{m_{(x_1,z_1)}} + C_N \frac{x_{cp} - x_1}{c} = 0 \tag{2.45}$$

By setting the reference point at the leading edge, eq. 2.45 becomes eq. 2.9.
The neutral line is a set of points for which $dC_m/d\alpha = 0$, oriented at an angle χ_2 (eq. 2.47). This line can be constructed as the direction of the difference vector between two resultants C_R of two consecutive angles of attack. The intersection point between the neutral line and the line of action of C_R is called the first metacenter M_1. The neutral point is the intersection between the neutral line and the mean chord

line, found at a distance x_n behind the leading edge located at x_0 (eq. 2.46) (Mulder, 2007, p. 171).

$$\frac{x_n - x_0}{c} = -\frac{dC_{m_{(x_0,z_0)}}}{dC_N} \tag{2.46}$$

$$\chi_2 = \arctan\frac{dC_A}{dC_N} \tag{2.47}$$

Two vectors dC_R at two infinitesimally close angles of attack form two neutral lines. The intersection point between these two is called the second metacenter, where $dC_m/d\alpha = 0$. This point represents the aerodynamic center ac, whose position is assumed constant for different α. This is valid for airfoils at angles of attack with no separation and for finite wings over a wide range of angles of attack and for moderate to large aspect ratios and small to moderate sweep angles (Mulder, 2007, p. 172). The analytical method to find the aerodynamic center consists in establishing a set of two equations and two unknowns, whilst knowing the properties of this particular point. The equations are as shown in equations 2.48a and 2.48b, the unknowns are the aerodynamic center's coordinates (x_{ac}, z_{ac}). Equation 2.42 can be written in terms of the aerodynamic center. A schematic representation of the moments in an airfoil is shown in (Mulder, 2007, p. 173).

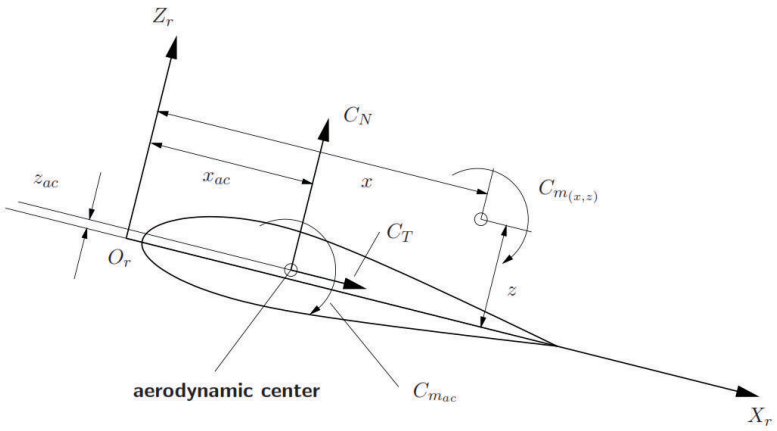

Figure 2.21: Moment about an arbitrary point on airfoil. The position of the ac and the $C_{m_{ac}}$ are known (Mulder, 2007, p. 176).

$$\frac{dC_{m_{ac}}}{d\alpha} = 0 = \frac{dC_{m_{(x_0,z_0)}}}{d\alpha} + \frac{dC_N}{d\alpha}\frac{x_{ac} - x_0}{c} - \frac{dC_A}{d\alpha}\frac{z_{ac} - z_0}{c} \tag{2.48a}$$

$$\frac{d^2C_{m_{ac}}}{d\alpha^2} = 0 = \frac{d^2C_{m_{(x_0,z_0)}}}{d\alpha^2} + \frac{d^2C_N}{d\alpha^2}\frac{x_{ac} - x_0}{c} - \frac{d^2C_A}{d\alpha^2}\frac{z_{ac} - z_0}{c} \tag{2.48b}$$

Usually, the effect of the axial force is neglected and the aerodynamic center is located on the mean chord line ($z_{ac} = z_0$). The equations 2.48a and 2.48b are then simplified yielding only one equation (eq. 2.49) (Mulder, 2007, p. 174).

$$\frac{x_{ac} - x_0}{c} = -\frac{dC_{m_{(x_0,z_0)}}}{dC_N} \tag{2.49}$$

2.3.3 EQUILIBRIUM CONDITIONS

The longitudinal stability is assessed via equations 2.50a and 2.50b, where $\frac{dC_N}{d\alpha}$ is always positive (Mulder, 2007, p. 177).

$$C_m = C_{m_{ac}} + C_N \frac{x - x_{ac}}{c} = 0 \tag{2.50a}$$

$$\frac{dC_m}{d\alpha} = \frac{dC_N}{d\alpha}\frac{x - x_{ac}}{c} \tag{2.50b}$$

The center of gravity plays an important role in stability, a stable aircraft is when $\frac{dC_{m_{cg}}}{d\alpha} < 0$. The equation of stability 2.50b can be written in terms of the center of gravity cg as shown in equation 2.51 (Mulder, n.d., p. 16).

$$\frac{dC_{m_{cg}}}{d\alpha} = \frac{dC_N}{d\alpha}\frac{x_{cg} - x_{ac}}{c} \tag{2.51}$$

The three conditions of stability regarding the center of gravity are (Mulder, n.d., p. 17):

- *Unstable*
  If the change in moment $dC_{m_{cg}}$ is in the same direction as $d\alpha$, i.e., $\frac{dC_{m_{cg}}}{d\alpha} > 0$.
- *Stable*
  When the change in moment is directed oppositely to $d\alpha$, having $\frac{dC_{m_{cg}}}{d\alpha} < 0$, the condition for stability.
- *Neutrally stable or indifferent*
  There is no change in moment ($dC_{m_{cg}} = 0$), thus $\frac{dC_{m_{cg}}}{d\alpha} = 0$.

As a result of these conditions, the center of gravity should be placed in front of the aerodynamic center and the center of pressure of the aircraft.

2.4 THE BLENDED WING BODY AIRFRAME

The Blended Wing Body is an airframe that combines different airfoils not only for the wings, as a conventional airplane, but for the center body as well, thus generating lift

throughout the whole airframe, not only on the wings. This concept has been studied as an alternative to the typical tube-and-wings configuration for massive transport, by NASA and BOEING, obtaining a working prototype in 2007, the X-48-B (fig. 2.22).

Figure 2.22: The X-48-B airframe (Creech, 2010).

The studies performed by BOEING showed a 15% reduction in TOW (take-off weight), with 27% reduction in energetic consumption for a BWB subsonic transport for 800 passengers (Liebeck, 2004, p. 10). These milestones were achieved due to the superior aerodynamic characteristics of the BWB, noticeably, to the fact that there are non-lifting surfaces in the BWB, as is demonstrated in figure 2.23.

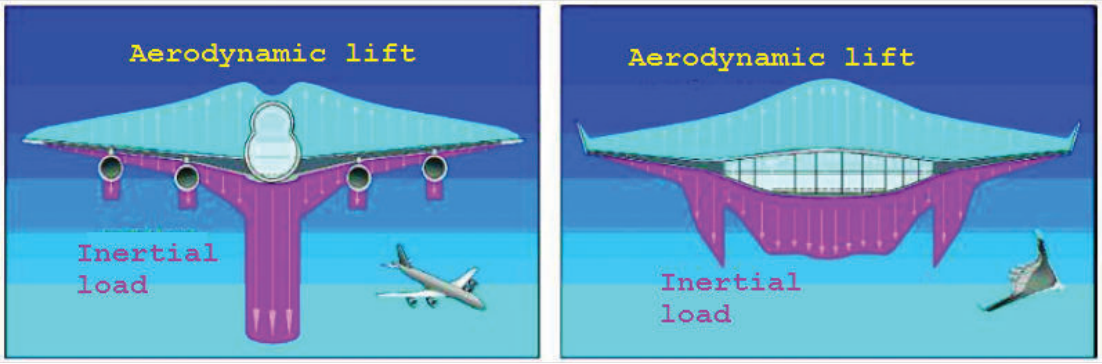

Figure 2.23: Lift and load comparison between a conventional aircraft and a BWB (Liebeck, 2004, p. 17).

The BWB airframe has a large amount of benefits in aerodynamic performance, in

propulsion and in energetic consumption. Effectively, all the cross sections of the BWB are airfoils that have high lift capabilities with low drag, giving a high lift-to-drag ratio of the airplane. A reduction in drag translates into less power needed to move the aircraft, hence less fuel consumed. The center section of the BWB can generate up to 60% of the total lift of the airframe, a major advantage compared to the conventional aerial vehicles.
Furthermore, the BWB can be fitted with laminar flow and boundary layer technology (Smith, 2000, p. 114.7), such as: Thrust Vectoring (TV), Boundary Layer Ingestion (BLI) and Distributed Propulsion (DP).
The BLI technology consists in absorbing the boundary layer flow over the airframe through a propulsor, in order to improve fuel consumption efficiency. The benefits of BLI integration to a BWB airframe can be as big as a 7% saving in power and an increase of 2.2% in propulsive efficiency (Plas, 2006, p. 29).

However, he benefits of the BWB configuration come at a cost. The lack of a tail in the airplane translates into difficulties in flight stability. This issues can be solved by the proper use of reflex airfoils in the center section and with the use of control surfaces (Thompson, 2011, p. 3). Another challenge in the design of a BWB lies in the power module integration with the airframe, since the installation of engines produce a decrease in the aerodynamic characteristics of the aircraft.

3 2D AIRFRAME PERFORMANCE ASSESSMENT

The methodology used to evaluate the two-dimensional aerodynamic performance and stability of the different airfoils consists in an XFOIL and MATLAB integration. The XFOIL program provides the raw data in a text format, which is then used in Matlab for the analytic data treatment. The different parameters that are involved and how they interact are shown in figure 3.1.

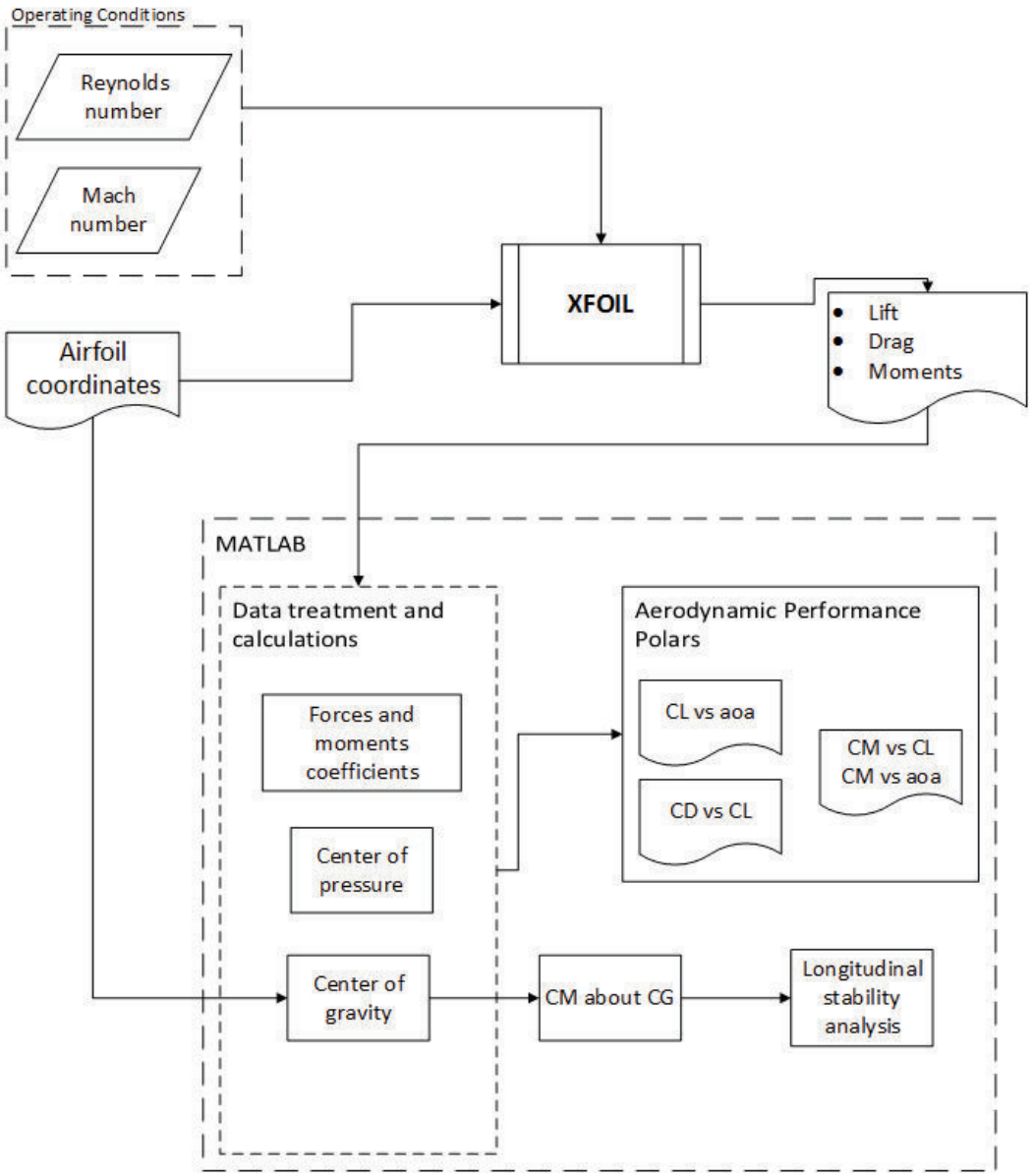

Figure 3.1: Two-dimensional methodology to obtain the aerodynamic performance and the stability characteristics of a chosen airfoil.

The operating conditions (altitude and cruise speed) are obtained from different drones that are being currently deployed for similar applications. The geometries of the different airfoils are obtained in coordinates in a .dat or .txt format file.

3.1 AIRFOIL SELECTION

The airfoils used in the present investigation are selected based on the design of a BWB UAV used for surveillance and reconnaissance and supplies transport (Thompson, 2011). Therein, low cambered airfoils are used to reduce aerodynamic moment to a minimum and custom airfoils are designed with high lift-to-drag ratio with very low moment. The lack of a tail in the BWB is a stability issue which can be solved by using airfoils with reflexed trailing edge, such as the MH45 and TL54 airfoils. The airfoil used for wings is a NACA 2412 with angle of attack of 2° and a washout of 6°. The root of the wing with higher α will stall first, preventing the airplane to spin. They have positive dihedral, a sweep angle of 33° and winglets at wing tips to eliminate wing tip vortices. A transition to custom “upside-down” airfoil is set at the wing tip, creating negative lift when flying at steady level, improving stability, reducing drag compared to a standard airfoil with more negative angle twist (Thompson, 2011).

The TL 54 airfoil was developed by Thorsten Lutz using the Eppler Code. It provides a moderately high lift, despite a low camber $(2,41\%)$ with reduced drag. The application of this airfoil is wide, with recent applications to tailless wings. The information about this airfoil, including its coordinates can be found in ref. (Siegmann, 2015a).

The MH 45 has relatively small lift coefficient, which can be corrected with appropriate design of wings and wing loading. it has a high reflexed trailing edge, which can help to increase stability of a tailless plane. The airfoil’s coordinates and additional literature can be found in (Siegmann, 2015b).

The NACA 2412 airfoil was developed by the National Advisory Committee for Aeronautics or NACA, the predecessor of NASA. The numbering of the airfoil indicates that it has 2% maximum camber and maximum thicknes of 12% at 40% chord length (Abbot I. H., 1945). The coordinates of this airfoil can be obtained in (*Airfoil Tools*, 2015).

The geometries of the different airfoils can be observed in figure 3.2.

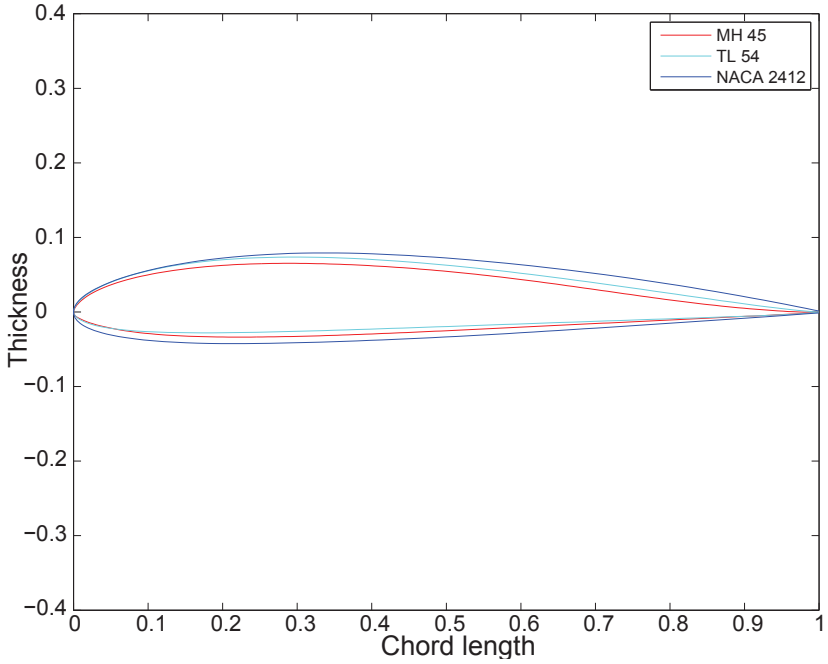

Figure 3.2: Geometries of the studied airfoils.

3.2 OPERATING CONDITIONS

A preliminary analysis is performed for steady level at operating conditions of two drones with applications comparable to the ones in this work. One of them is a surveillance drone operated by the Ecuadorian Air Force FAE (Calero, 2014), which operates at $20,000$ feet above sea level, nearly $6,250$ meters above sea level. The other drone was developed recently by the Florida Institute of Technology. It is a blended wing body for applications in agriculture, surveillance and cargo transport at a maximum operating speed of 36 meters per second (Thompson, 2011).

In the present work, the applications of the UAV are in agriculture, surveillance among others, as mentioned. The flight altitude is 7000 meters above sea level, at which the FAE drones operate at the Andean region. The speed is 50 meters per second, a subsonic speed which is the operating speed of similar drones in similar applications.

The flow characteristics at the selected altitude and speed can be computed using the appendix A. The air properties at the selected operating conditions are shown in table 3.1.

Table 3.1: Air properties, adapted from (Roskam, 1997).

Altitude	Temperature	Temp. Ratio	Pressure	Press. Ratio	Density	Dens. Ratio	Dynamic Viscosity	Speed of Sound
h $[m]$	T $[K]$	θ	p $[N/m^2]$	δ	$\rho\,[kg/m^3]$	σ	$\mu \cdot 10^5\,[N.s/m^2]$	$V_a[m/s]$
7000	$242,7$	8421	41060	$0,4052$	$0,5895$	$0,4812$	$1,561$	$312,4$

The consequent Reynolds and Mach numbers are show in table 3.2.

Table 3.2: Flow characteristics

Reynolds number	Mach number	Chord length [m]
$5.7e6$	0.16	3

3.3 AERODYNAMIC PERFORMANCE

The lift curves of three different airfoils are represented in figure 3.3. The range of variation of α is from an angle below the zero lift angle to a positive angle above the stall of the airfoil.

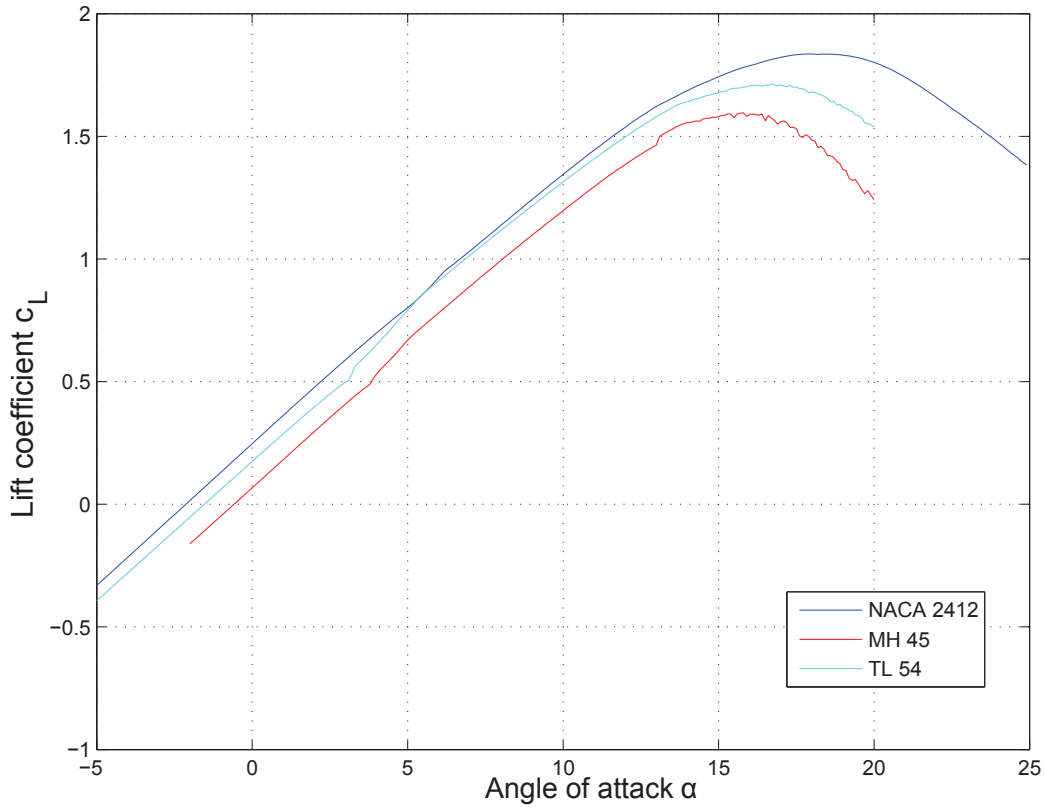

Figure 3.3: Lift curves of the airfoils.

The NACA 2412 airfoil has the better lifting characteristics in the studied range, particularly in small angles (up to $5°$). It is also the airfoil that stalls later than the others, around $19°$ (TL 54 stalls around $17°$ and MH 45 around $16°$). The maximum lift coefficients from highest to lowest are those of the NACA 2412, TL 54 and MH 45 (1.85, 1.75 and 1.55, respectively).
This performance superiority is due to the fact that the NACA 2412 airfoil is optimized for lift and the TL 54 and MH 45 airfoils have geometries that reduce lift in order to improve stability, namely their reflexed trailing edges.

The distribution of pressure coefficients around the different airfoils is presented in figure 3.4. The NACA 2412 airfoil is set at a 2° angle of attack at the wing root, ensuring root stalling (Thompson, 2011). The other airfoils are set at 0° for cruise conditions.

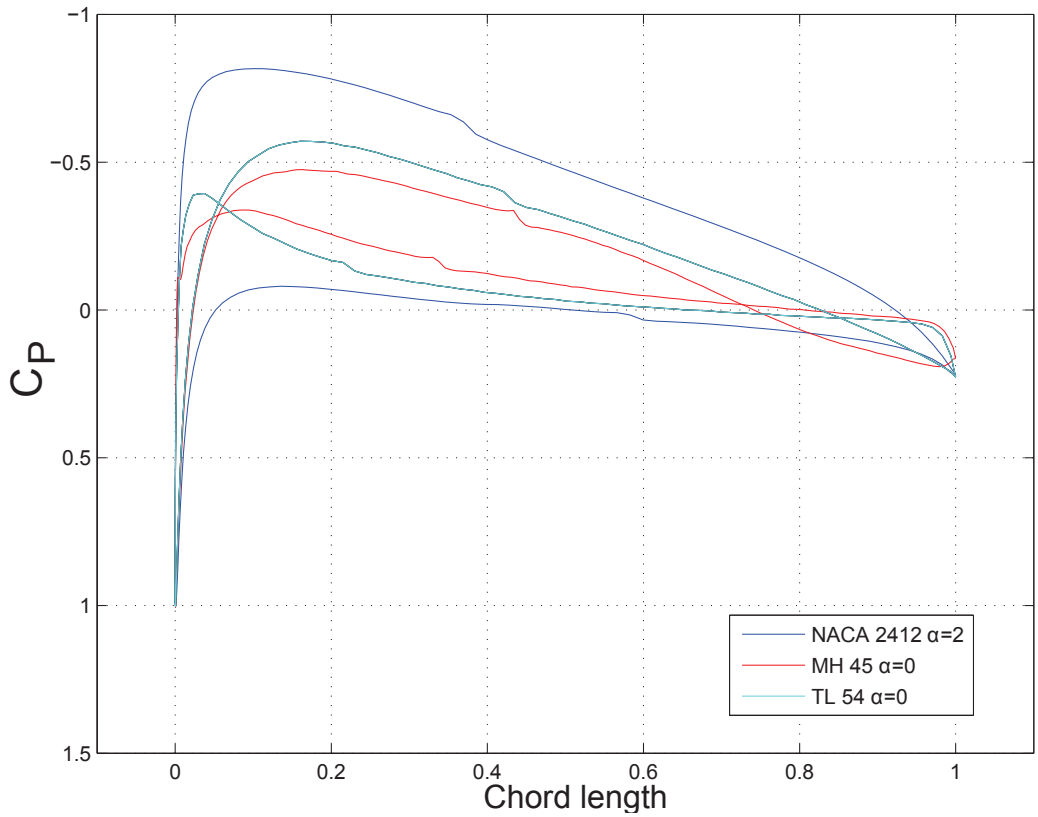

Figure 3.4: Pressure distribution around the three studied airfoils: NACA 2412, MH 45 & TL 54.

From the pressure distribution, no separation is observed, only a small ”bump” around 40% chord length on the upper surfaces of the airfoils, which indicates only the laminar-to-turbulent transition. There is no shock indications either, which is con-

sistent with the flow conditions (subsonic Mach number of 0.16).
The largest pressure difference is around the surfaces of the NACA airfoil, since it has a larger angle of attack than the other airfoils and its overall better lifting characteristics (as seen in fig. 3.3).
The effect of the reflexed trailing edge can be clearly observed in the distribution from around 75% and 82% chord for the MH 45 and TL 54 airfoils, respectively. The pressure on the bottom surface remains nearly constant whereas on the upper surface, the pressure increases overtaking the value on the bottom surface. This generates a negative lift that stabilizes the airfoil.
The net pressure difference between both surfaces of the airfoils explains the lifting characteristics seen in figure 3.3. A larger area between curves means better lift.

The drag characteristics of the studied airfoils are presented in figure 3.5. The drag coefficient variation with lift coefficient is presented in figure 3.5a and the lift-to-drag (glide) ratio is polar is shown in figure 3.5b.

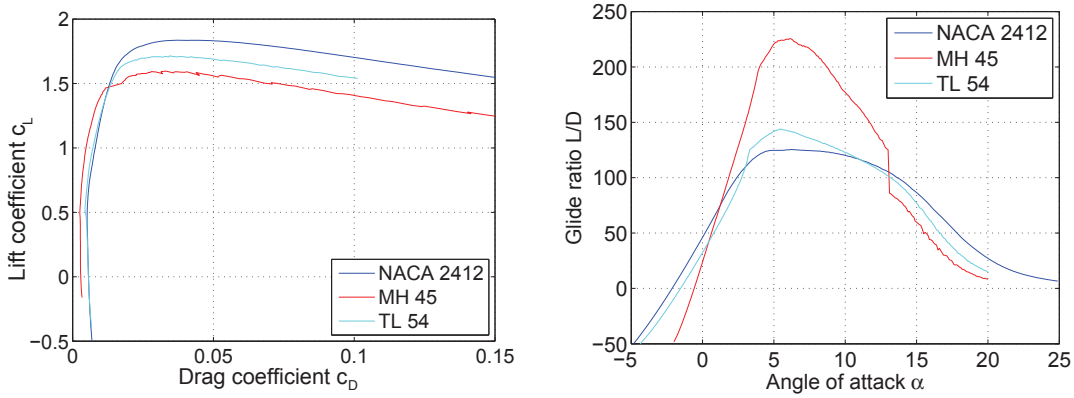

(a) Drag vs. lift variation of the airfoils.

(b) Glide ratio vs. angle of attack.

Figure 3.5: Drag polars of the different airfoils

The MH 45 airfoil has lower drag for lift coefficients below 1.5 (fig. 3.5a). The steady flight study conducted in this work means that the angles of attack are near zero, hence, as seen in figure 3.3, at low lift coefficients. The MH 45 airfoil has the lowest drag for operating conditions, followed by the TL 54 and the NACA 2412 airfoils, in that order.
However, for very small angles of attack (0 to $2.5°$), the MH 45 airfoil has the lowest lift-to-drag ratio. This tendency changes nevertheless from $3°$ and it reaches a significantly higher maximum glide ratio of 225 (vs. 140 of the TL 54 and 125 of the NACA 2412). This means that more lift may be produced by increasing the angle of attack, speed or chord length, with very low increase in drag.

The relatively high drag characteristics of the NACA 2412 is a clear example of one of the sacrifices that must be made in aerodynamic performance. Effectively, the larger thickness of the NACA 2412 (as seen in fig. 3.2) translates in more lift, but also in more drag. This is why the less thick airfoil (the MH 45) has relatively low lift but even lower drag.

The moments produced by the distributed forces around the different airfoils are shown in figure 3.6.
The aerodynamic center is set to be at quarter chord length of the MH 45 and TL 54 airfoils, which is an accurate approximation as demonstrated in a previous section (Houghton, 2013, p. 44). For the NACA 2412 airfoil however, specific information can be found where the aerodynamic center is located at 23.4% chord length from the leading edge, and at 0.4% below the chord line (Abbot I. H., 1945, p. 136).

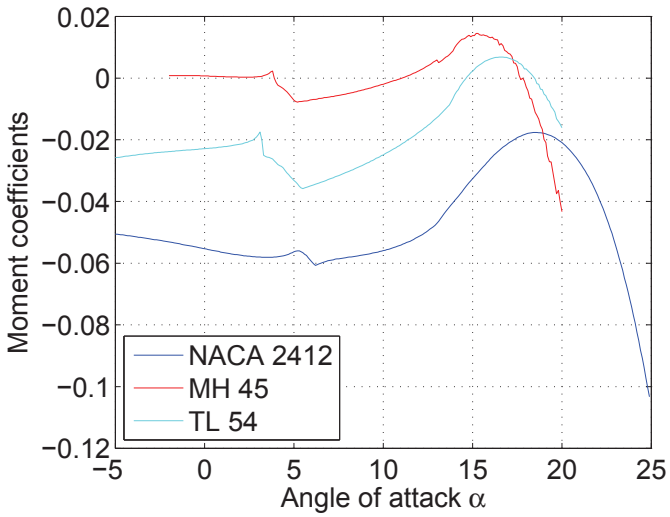

Figure 3.6: Moment coefficients vs. angle of attack, calculated respect to the aerodynamic center.

For small angles of attack (0 to $10°$) and small lift coefficients (up to 1), the MH 45 airfoil is the one with the moment closest to zero. More negative values are reached with the TL 54 and NACA 2412 airfoils, respectively. It can be readily seen the stabilizing effect of the reflexed trailing edges of the MH 45 and TL 54, since less absolute value of moment means a more stable airfoil. A further analysis regarding stability is conducted in a latter section.

3.3.1 DISCUSSION

As expected, the NACA 2412 airfoil produces more lift due to its thicker geometry. However, this increase in thickness comes with increased drag and more negative moment about the aerodynamic center. It has a higher lift coefficient and it stalls at a higher angle of attack than the other airfoils. The NACA 2412 is then better suited for the wing, since it provides good lift with small chord lengths and varying angles of attack (twist) reducing the drag around the airfoil to a minimum.

The MH 45 airfoil has the lowest lifting characteristics due to it pronounced reflexed trailing edge. Nevertheless, this airfoil produces the less drag and it has the higher glide ratio and the less moment. It is then optimal airfoil for the center body of the blended wing body, where a larger chord length will be used and the drag will not increase as much as if using any other of the airfoils for the center body.

The TL 54 reflex airfoil is a intermediate point between the MH 45 and the NACA 2412 airfoils, it can be used as a transition in the blended wing body from inboard to the wings.

3.4 STATIC LONGITUDINAL STABILITY ANALYSIS

The curves used to determine the static stability of the different airfoils are presented in figures 3.7 and 3.8. In the first one, the location of the center of gravity, center of pressure and aerodynamic center is presented for the studied airfoils at different angles of attack. The aerodynamic center is invariant as is the center of gravity (x_{cg}). To determine the latter, a numerical area integral method was employed, using the coordinates of the airfoils. The center of gravity is the centroid of the section and it is calculated as follows (Protter, 1970, p. 528):

$$A = \int_{LE}^{TE} y_t(x) - y_b(x) dx \tag{3.1a}$$

$$x_{cg} = \frac{1}{A} \int_{LE}^{TE} x(y_t - y_b) dx \tag{3.1b}$$

Where A is the area of the airfoil, y_t and y_b are the ordinate of the upper and bottom surfaces, respectively.

The center of gravity herein calculated is that of the airfoils alone, considering a uniform weight distribution. The location of additional equipment (payload, propulsors

and electronics) may shift the center of gravity, therefore, they were not considered.

The center of pressure is calculated using eq. 2.45, with the leading edge as the reference point ($x_1 = 0$):

$$x_{cp} = -\frac{C_{m_{LE}}}{C_N} \tag{3.2}$$

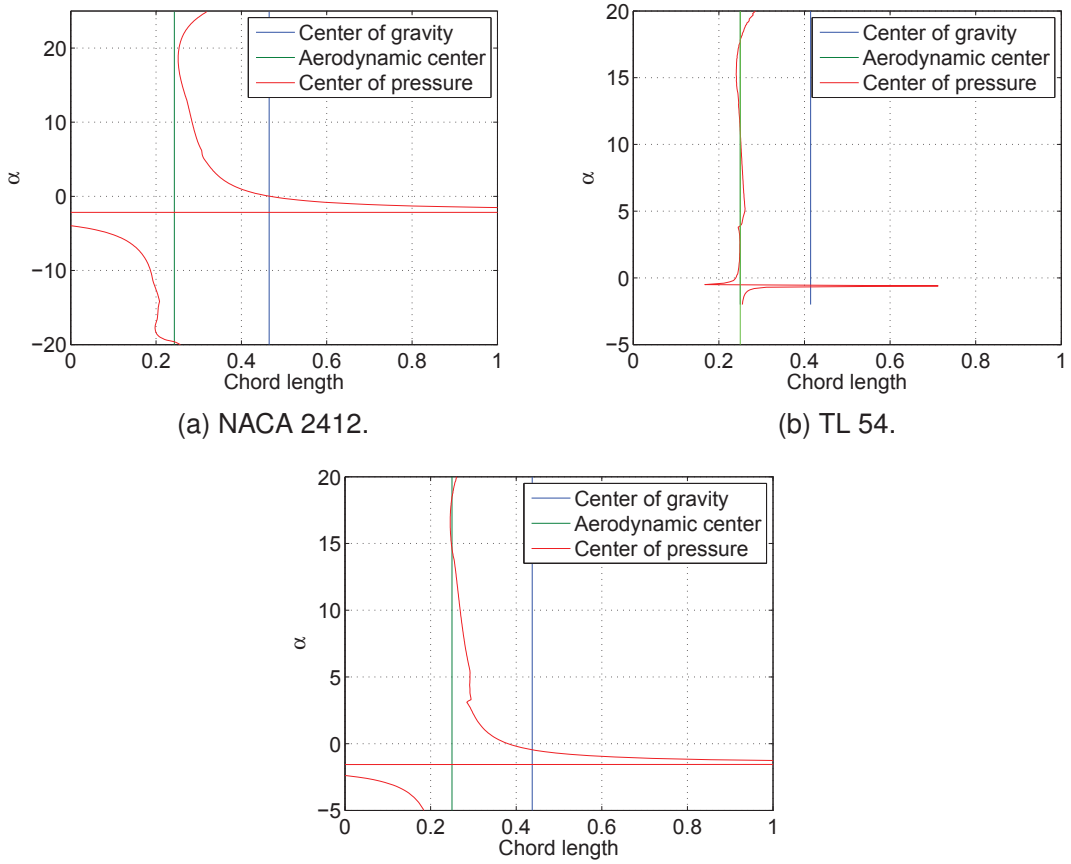

(a) NACA 2412.

(b) TL 54.

(c) MH 45.

Figure 3.7: Location of the metacentres on the airfoils at different angles of attack

The steady flight analysis is for small angles of attack (in the vicinity of $0°$). The center of pressure is the only metacenter that changes its location widely with the angle of attack, since it is the location where the resultant force is applied. In figures 3.7, asymptotes can be observed for the three airfoils at their respective angle of zero lift.

The general location of the centres of gravity is behind the center of pressure, except for angles near the zero-lift angle. Furthermore, at the design operating angles of attack ($2°$ for the NACA 2412 and $0°$ for the MH 45 and TL 54), the center of pressure is noticeably in front of the center of gravity.

When the center of pressure is closer to the aerodynamic center, the moment about the latter will be reduced, improving the stability of the arifoil. In the MH 45, both metacentres are practically coincident and the result is a reduced moment in comparison with the other airfoils (as seen in fig. 3.6). The metacenters in the NACA 2412 are not coincident in any angle of attack, which explains the higher value of the moments on this airfoil. The TL 54 is, once again, a sort of middle point between the NACA 2412 and the MH 45.

The conditions of stability introduced in section 2.3.3 are herein applied, using figure 3.8.

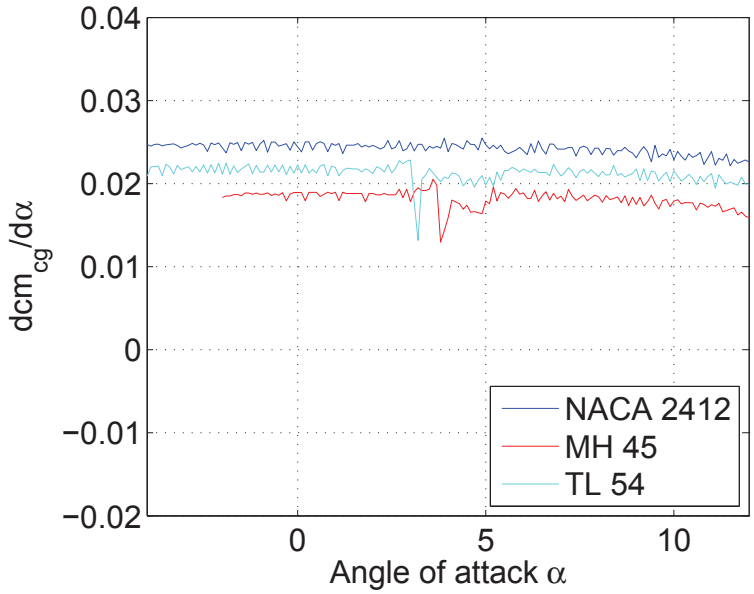

Figure 3.8: Stability curves comparison.

As explained in section 2.3.3, an airfoil is stable when the change of moment about the center of gravity $dC_{m_{cg}}/d\alpha$ is negative or equal to zero. However, none of the three airfoils accomplish this condition, this derivative is positive in all the studied range (fig. 3.8). Anyhow, the airfoil with the derivative closest to zero is the MH 45, followed by the TL 54 and, finally, the NACA 2412.

3.4.1 DISCUSSION

The result of the stability analysis, using the criteria introduced in section 2.3.3, is that the airfoils are not stable by themselves. In a conventional airplane, this issue is commonly fixed by adding a tail. However, in a tailless aircraft such as the BWB,

this fix cannot be applied. There are, anyhow, other solutions for moving the center of pressure behind the center of gravity, such as adequate sweep angle and taper ratio.
These solutions will be explored in the three-dimensional design of the aircraft.
For this analysis, the weight and location of auxiliary components and equipments of the aircraft were not considered. However, these components can weigh up to 45 pounds and they must be carefully located in the future (Gundlach, 2011).

3.5 BOUNDARY LAYER INGESTION ANALYSIS

The concept of the Blended Wing Body airframe has been developed along with ground-breaking solutions in terms of propulsion. The N3-X Hybrid Wing Body has been coupled with boundary layer ingestion and distributed propulsion systems as a field of investigation at NASA (Kim, 2013).

In this section, a preliminary analysis of boundary layer availability is performed for the center-body airfoil. The application of a boundary layer ingesting system may increase propulsive efficiency and lower energetic consumptions (Plas, 2006).

The system will be set at a height that would allow to *ingest* the turbulent boundary layer from a specified chord offset to the trailing edge as suggested in ref. (Felder, 2011). The inlet is set at 80% chord length, a distance beyond the laminar-turbulent transition (around 60% chord length at the upper surface) (Valencia, 2015).

The chord Reynolds and Mach numbers of the center airfoil is calculated using the air properties from table 3.1, as follows:

$$Re_c = \frac{\rho_\infty V_\infty c}{\mu} = \frac{0.5895 * 50 * 2.6}{1.561 * 10^{-5}}$$

$$Re_c = 4\,900\,000 \tag{3.3}$$

$$M = \frac{V_\infty}{V_a} = \frac{50}{312.4}$$

$$M = 0.16 \tag{3.4}$$

An XFOIL analysis will be performed using these parameters to the center body airfoil (MH 45 of 2.6 meters chord length) in order to obtain the boundary layer properties. The Blasius solution for a flat plate will be used to compute the boundary layer thickness (δ) from the displacement thickness (δ^*), as follows (Anderson Jr., 1991, p. 728):

$$\delta = \frac{5.0}{1.72}\,\delta^* \tag{3.5}$$

The boundary layer thickness distribution along the MH 45 airfoil can be seen in figure 3.9.

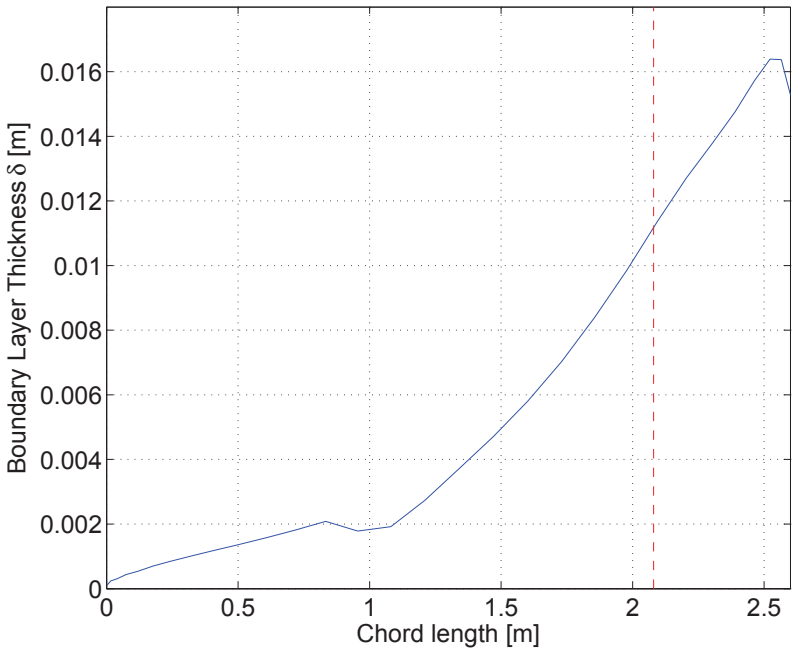

Figure 3.9: Boundary layer thickness at the center body. The red line indicates the 80% chord location of the boundary layer ingesting system.

The boundary layer thickness reaches a maximum value close to 1.6 centimeters near the end of the airfoil. This value is not enough to consider the inclusion of a BLI system in the present BWB airframe since the propulsive systems are significantly larger than the height of the boundary layer and thus practically eliminating the benefits of installing this system.

Nevertheless, additional configurations or solutions can be applied to obtain the benefits of the BLI systems. In ref. (*Propulsive Wing Technology*, 2015), cross-flow fans can be distributed in a spanwise direction of an aircraft of sizes that range from small UAVs to large cargo planes. This solution allows to ingest a larger amount of the flow around the body, resulting in higher lift, lower drag and almost zero stall. However, these solutions are not in the scope of this work and may be explored in future works.

4 3D ANALYSIS, NUMERICAL METHODS AND CFD

The three-dimensional analysis is carried out using two programs, open-source XFLR5 and ANSYS. The first a user-friendly interface for XFOIL with an extension for wing design, which will be used in this part. The XFLR5 program is used as a starting point for obtaining the model and for fast calculations and results. The ANSYS FLUENT module is then used to obtain more accurate results.

4.1 DESIGN CONSIDERATIONS

As explained in (Kuntawala, 2011, p. 35), the main limitation in the design of a Blended Wing Body is the lack of relevant data or practical information about this subject. Furthermore, in the most advanced studies in the BWB subject, such as refs.: (Liebeck, 2004), (Baier, 2015), (Kuntawala, 2011), (Bradley, 2004) and (Lyu, 2013), the size of the aircraft is significantly larger to the one in the present work, which means that some general aerodynamic concepts may be adapted, but the main design considerations (sizing, weight, range) do not apply.

For this work, the baseline configuration is adapted from ref. (Thompson, 2011), since it is a BWB with similar function and applications. In that publication, the wingspan is set at 5 meters, the take-off weight is 50 kilograms and they use customized airfoils based on the NACA 2412, MH 45 and TL 54. These airfoils are a good starting point, since their relative thickness do not surpass 17%, optimizing the energetic consumption of a BWB (Baier, 2015, p. 32).

The sweep angle moves the center of pressure backwards and it increases the maximum lift coefficient. A non-adequate sweep angle may translate into a tendency to tip stall since an outboard spanwise flow is generated (boundary layer thickens as it approaches the tips) (Roskam, 1997, p. 115). The sweep angle of the BWB model is set at 50° in the center body and 33° in the wings, as suggested in (Bradley, 2004), (Baier, 2015) and (Thompson, 2011).

As a countermeasure for tip stall, negative twist is set. Washout in a wing delays tip stall and benefits elliptical distribution (Roskam, 1997, p. 116). For the center body and wing root, no twist is set for maximum available space (Kuntawala, 2011). The wings start at a 2° angle of attack and end at -4°, as suggested as optimal in (Thompson, 2011).

The elliptical distribution for lift is used as the optimal wing loading distribution (Baier, 2015, p. 31), (Roskam, 1997, p. 115), (Kuntawala, 2011) & (Lyu, 2013). The present work is focussed on the cruise stage, i.e., stable flight, for which the overall summation of forces is null. The weight of the plane is then equal to the total lift and the thrust force is equal to the drag force.

In the first approach studied in (Liebeck, 2004, p. 14), the main deck is set to be 125 ft long, near 40% of the total span (280 ft). This parameter will be conserved in the preliminary design made in this work.

The selection of the airfoils for the different airplane sections is made according to the criteria established in the aerodynamic performance and static stability two-dimensional analyses. The MH 45 airfoil is set as the center body airfoil, at an angle of attack of 0°. The TL 54 airfoil at 0° section begins at 50 centimetres from the center body and it is used for the transition of the center body to the wing root. The NACA 2412 is used for the wings, starting at 1 meter from the center body to the semi-span length of 2,5 metres. The wings have negative twist, starting at a local 2° to $-4°$ at the outboard.

The airfoil spanwise configuration explained above is shown in table 4.1.

Table 4.1: Spanwise configuration

Body	Root	Wing	Wing tip
MH 45	TL 54	NACA 2412	NACA 2412
y_0	y_1	y_2	$b/2$
0	$0,5$	1	$2,5$
α_0	α_1	α_2	α_3
0	0	2	-4

The circulation around the center body airfoil Γ_0 is calculated using eq. 2.38, which gives:

$$\Gamma_0 = \frac{4L}{\rho_\infty V_\infty \pi b} = \frac{4W}{\rho_\infty V_\infty \pi b} = \frac{4 * 50 * 9,81}{0,5895 * 50 * \pi * 5} = 4,2377\,[m^2/s] \tag{4.1}$$

The elliptical distribution of circulation for the BWB model is then:

$$\Gamma(y) = \Gamma_0 \sqrt{1 - \left(\frac{2y}{b}\right)^2} = 4,2377 \sqrt{1 - \left(\frac{2y}{5}\right)^2} \tag{4.2}$$

The sought-after elliptic circulation and lift distributions can be seen in figure 4.1.

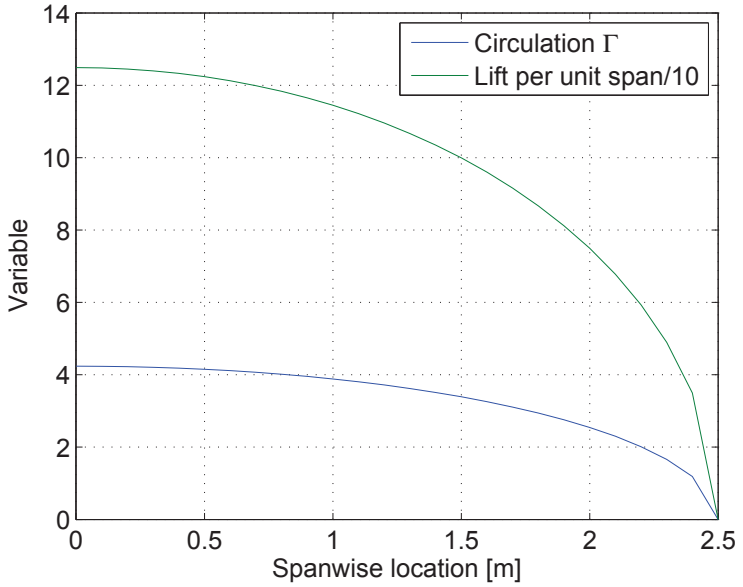

Figure 4.1: Circulation and lift elliptic distribution.

To obtain the chord length c_0 of the origin airfoil, the Kutta-Joukowski theorem (eq. 2.19) and the lift per unit span coefficient c_{l_0} are used as follows:

$$
\begin{aligned}
L'_0 &= \rho_\infty V_\infty \Gamma_0 \\
L'_0 &= \frac{1}{2}\rho_\infty V_\infty^2 c_{l_0} c_0 \\
c_0 &= \frac{2\Gamma_0}{c_{l_0} V_\infty}
\end{aligned}
\tag{4.3}
$$

Eqs. 4.3 and 4.2 can be used to obtain the chord length c of the airfoil located at any spanwise location y as follows:

$$
c(y) = \frac{2\Gamma(y)}{c_l(y) V_\infty} \tag{4.4}
$$

The lift coefficients are obtained from the operation points of each airfoil. The chord lengths of each airfoil change (c_0, c_1 and c_2 located at y_0, y_1 and y_2, respectively) are shown in table 4.2

Table 4.2: Calculated chord lengths, in meters

c_0	c_1	c_2
$2,53$	$0,95$	$0,33$

4.2 BASELINE CONFIGURATION

The preliminary design (Mark 1) of the defined blended wing body is shown in figure 4.2. It was constructed using the XFLR5 wing analysis tool according to the data shown in table 4.3.

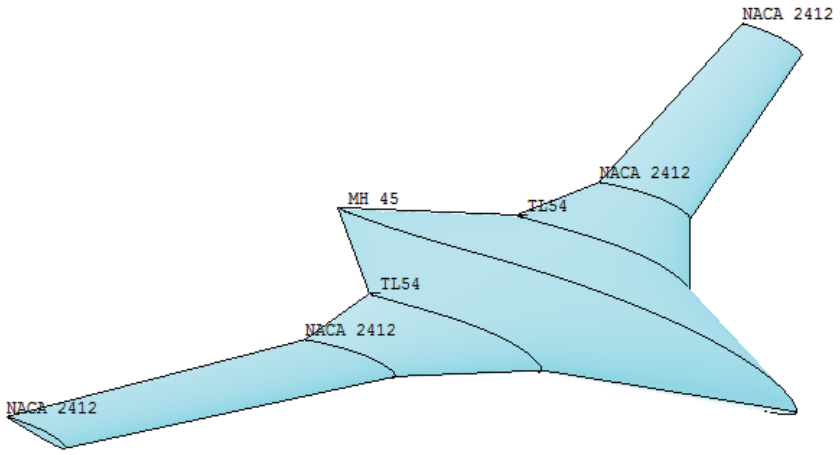

Figure 4.2: BWB mark 1.

The wing edition interface is shown in table 4.5. The first column (y (m))is the spanwise location from the center body. The second column is where the chord length of the section is set. The offset is the chordwise distance between the leading edges of two consecutive airfoil sections. In the third column, the offset is established to obtain the desired sweep angle values (50° and $33°$ at the leading edge and wing root, respectively). The dihedral, twist and foil columns are self explanatory. The first three columns represent the y, c and o parameters shown in figure 4.3, in the same order.

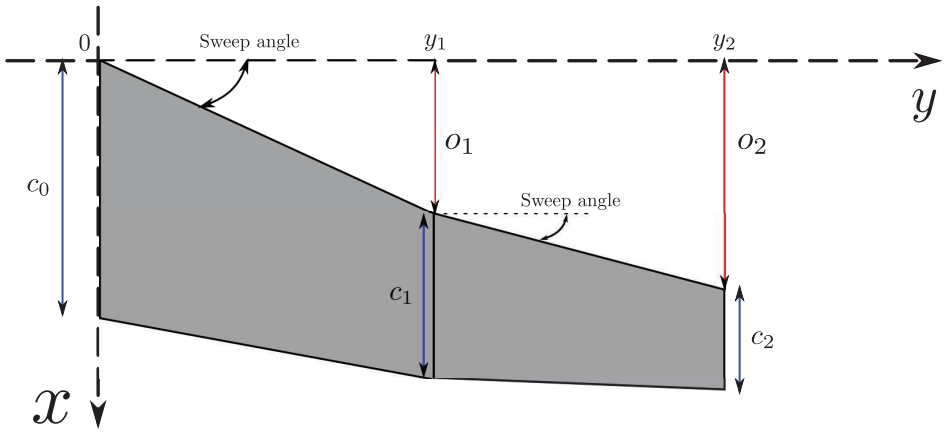

Figure 4.3: Wing edition parameters.

In the same wing edition interface, the panelling configuration is set in the columns X-panels, X-dist, Y-panels and Y-dist of table 4.3. The X-panels and Y-panels columns define the number of divisions the section will have in the x and y directions in fig. 4.3, respectively. In the X-dist and Y-dist columns, the distribution of the divisions along the x and y directions are set, respectively.
There are two distributions available in the x direction (uniform and cosine) and four in the y direction (uniform, cosine, sine and -sine). These four types of distributions can be seen in figure 4.4.

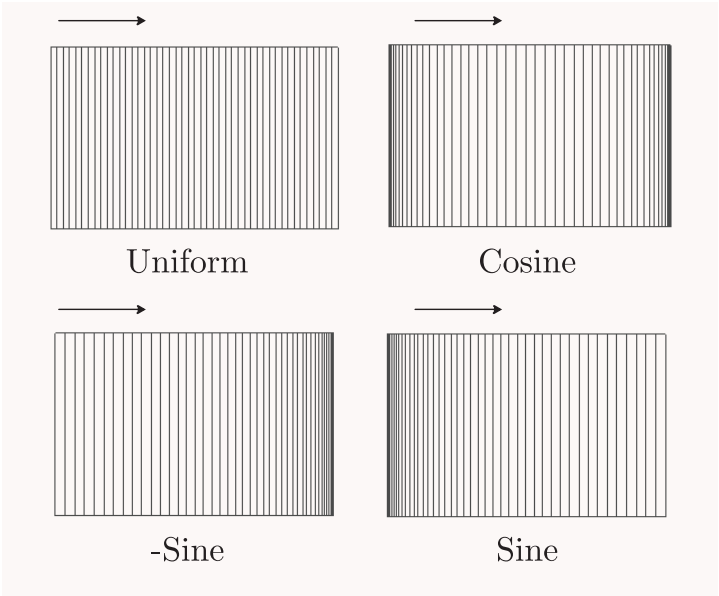

Figure 4.4: Y panel distribution.

In the *uniform* distribution the divisions are equally spaced. The *cosine* distribution

refines the grid close to both beginning and ending boundaries of the section. The *sine* distribution results in a mesh refinement around the inboard boundary. The *-sine* distribution is the opposite of the *sine* distribution, the refinement is close to the outboard boundary.

This way, an appropriate panel distribution can be configured, as shown in table 4.5.

Table 4.3: BWB mark 1 definition

No.	y [m]	Chord [m]	Offset [m]	Dihedral [°]	Twist [°]	Foil	X-panels	X-dist	Y-panels	Y-dist
1	0,0	2,53	0,0	0,0	0,0	MH 45	35	Cosine	25	-Sine
2	0,5	0,95	1,0	0,0	0,0	TL 54	35	Cosine	15	Sine
3	0,75	0,725	1,2	0,0	0,0	TL 54	35	Cosine	15	-Sine
4	1	0,5	1,4	0,0	2,0	NACA 2412	35	Cosine	28	Sine
5	2,5	0,33	2,0		-4,0	NACA 2412				

In the panelling process, the problems that may be encountered are in the airfoil transitions, where the panels may not be aligned properly. To solve this issue, the same number of panels in the X direction has been set for all sections. Additionally, a combination of *sine* and *-sine* panel distribution has been given to consecutive panels to increase the panel density in the transitions. An additional section has been added (section 3) before the transition from TL54 to NACA2412 in order to achieve the panel refinement at said transition.

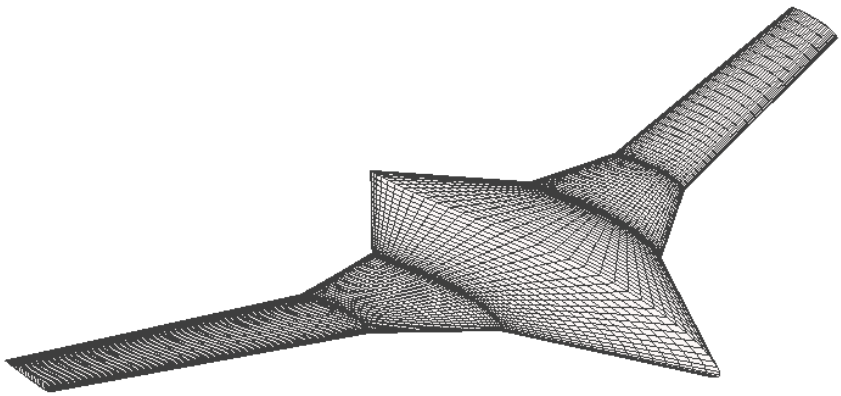

Figure 4.5: BWB mark 1 panelling.

The geometric properties of the BWB mark 1 are shown in table 4.4.

Table 4.4: BWB mark 1 properties

Wing Span	=	5,0 [m]
Wing Area	=	3,71 [m^2]
Plane Mass	=	50,0 [kg]
Wing Load	=	13,48 [kg/m^2]
Root Chord	=	2,53 [m]
MAC	=	1,16 [m]
Aspect Ratio	=	6,739
Taper Ratio	=	7,667
Root-Tip Sweep	=	30,114 [°]

The XFLR5 program offers a variety of analysis methods, including a 3D panel method with Dirichlet boundary conditions, which is used for the present analysis, as recommended in (Deperrois, 2013). The analysis conditions used are as shown in table 4.5.

Table 4.5: 3D analysis conditions

$V_\infty[m/s]$	$\rho_\infty[kg/m^3]$	$\nu_\infty[m^2/s]$	α	Dynamic pressure $q_\infty[kg/m.s^2]$
50	$0,589$	$2,6 \cdot 10^{-5}$	$0°$	$736,88$

The aerodynamic performance results of the BWB mark 1 can be seen in table 4.6.

Table 4.6: BWB mark 1 aerodynamic performance results

```
Type 1 (Fixed speed)
3D-Panels
Tilted geometry

VInf  = 50.000 m/s  CL  =  0.13146
Alpha =  0.00°      CD  =  0.00706
Mass  =  0.000 kg   VCD =  0.00596
XCP   =  1.561 m    ICD =  0.00110
YCP   =  0.000 m    Cm  = -0.03258
ZCP   =  0.103 m    ICm = -0.03247
                    VCm = -0.00011
```

The lift vs. drag polar, lifting curve, moment curve and lift-to-drag curve are presented in figure 4.6, from left to right, up to down, respectively.

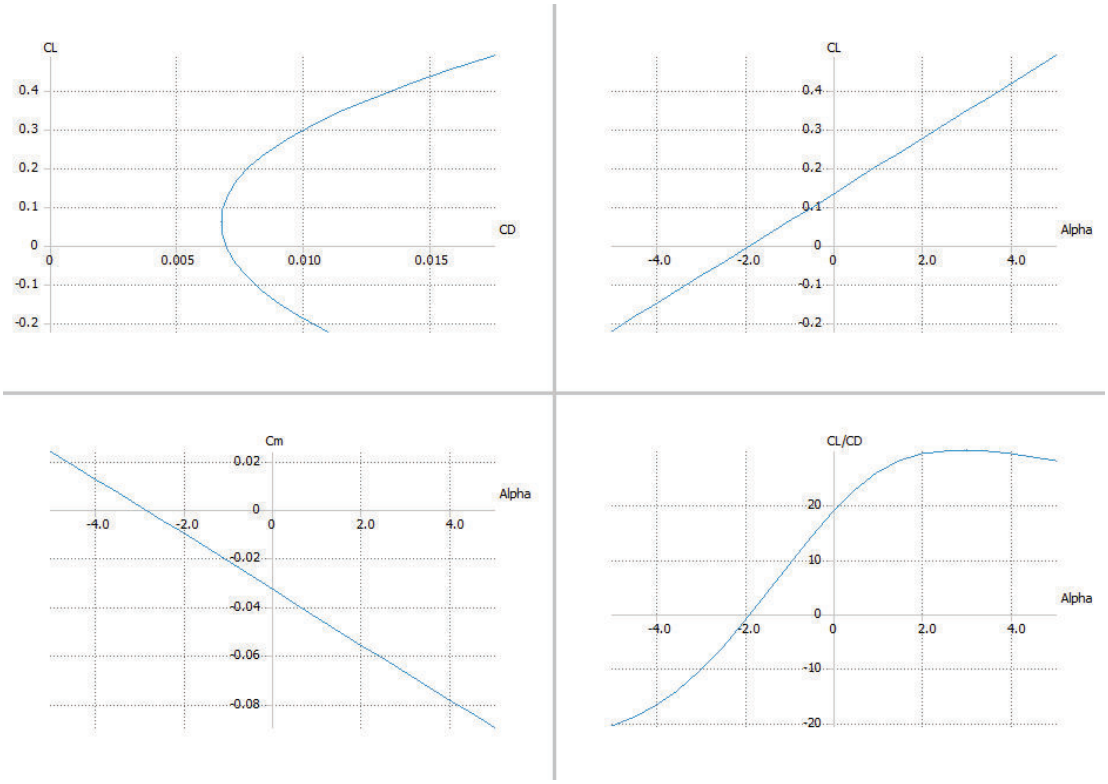

Figure 4.6: BWB Mark 1 polars and curves.

The pressure coefficients around the upper and bottom surfaces of the plane can be seen in figure 4.7.

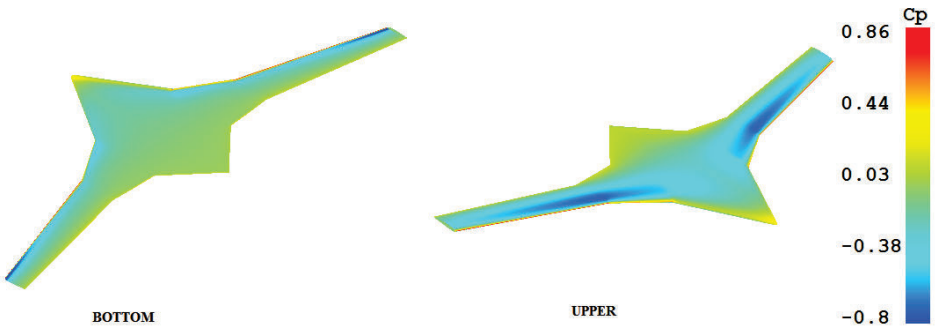

Figure 4.7: Pressure coefficients around the BWB Mark 1.

A noticeable pressure difference can be spotted between the upper and bottom surfaces of the wings and center body. On the core of the BWB, the pressure difference is not very large and at the trailing edge, the pressure is larger on the upper surface. This is due to the charactersitics of the MH45 and TL54 airfoils, they have a reflexed trailing edge and low thickness, which reduces lift but helps for pitching stability. The

negative pressure on the upper section of the wings reduces from the root to the wing tips, showing the effect of the washout.
Furthermore, the pressure diminishes from the center body to the wing tip and reaches a minimum near the wing root, at the TL54-NACA2412 transition. The pressure then increases to the wing tips. A spanwise flow is generated due to the 3D effects, however, this flow does not reach the wing tip. If this flow would reach the tips, the plane would have a tendency to tip stall and a loss in overall stability.

In figure 4.8, the viscous drag (left) and the summation of viscous and induced drag (right) are presented in a spanwise distribution.

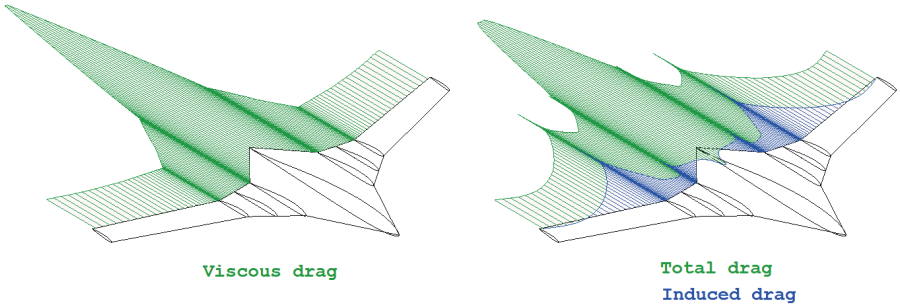

Figure 4.8: BWB Mark 1 drag distribution. In the left figure, only the viscous drag is shown (green), in the right one, the total drag is in green and the induced drag is in blue.

Notice that induced drag reduces total drag in the wing tip and in the center of the body.

The spanwise lift distribution around the plane can be seen in figure 4.9. The target of elliptical distribution is not completely reached, the core section of the BWB reduces lift due to the MH45 airfoil characteristics (low lift, reflexed trailing edge). Furthermore, the lift augmentation on the edge of the center body is due to the fact that the chord length of the NACA 2412 airfoil section at the wing tip is larger than that calculated ($0,5$ vs $0,33$ meters).

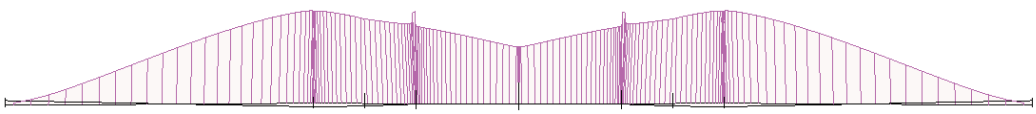

Figure 4.9: BWB Mark 1 lift distribution.

The total lift force can be calculated using eq. 2.17a and the data obtained from tables 4.4 and 4.6.S is the wing area. The lift is then:

$$L = C_L * S * q_\infty = 0,13146 * 3,71 * 736,88$$

$$L = 359,4\,[N] = 36,6\,[kg] \tag{4.5}$$

This preliminary design does not generate enough lift force to carry the 50 kilogram payload. This is due to the reduction in lift on the center body, as seen in figure 4.9.

An alternate configuration must be set (Mark 2), one that fits the payload requirements. The Mark 1 loss of lift in the center body may be corrected by increasing the chord length of the corresponding MH45 airfoils. To increase lift, the NACA 2412 must have more surface, the center body can be reduced from 1 to 0.5 meters, allowing more area for the wings. The reduction of the center body is necessary, since the parameters set for the Mark 1 were similar to those of a transporting BWB, where more space is needed in the center of the plane.

The wing properties of the BWB Mark 2 are shown in table 4.7

Table 4.7: BWB mark 2 definition

No.	y [m]	Chord [m]	Offset [m]	Dihedral [°]	Twist [°]	Foil	X-panels	X-dist	Y-panels	Y-dist
1	0,0	2,6	0,0	0,0	0,0	MH 45	25	Cosine	3	Sine
2	0,05	2,4	0,1	0,0	0,0	TL 54	25	Cosine	7	-Sine
3	0,25	1,2	0,7	0,0	0,0	TL 54	25	Cosine	6	-Sine
4	0,5	0,75	1,0	0,0	2,0	NACA 2412	25	Cosine	21	Sine
5	2,5	0,1	2,33		-4,0	NACA 2412				

The same panelling criteria are applied to define the mesh structure in the new model, shown in figure 4.10

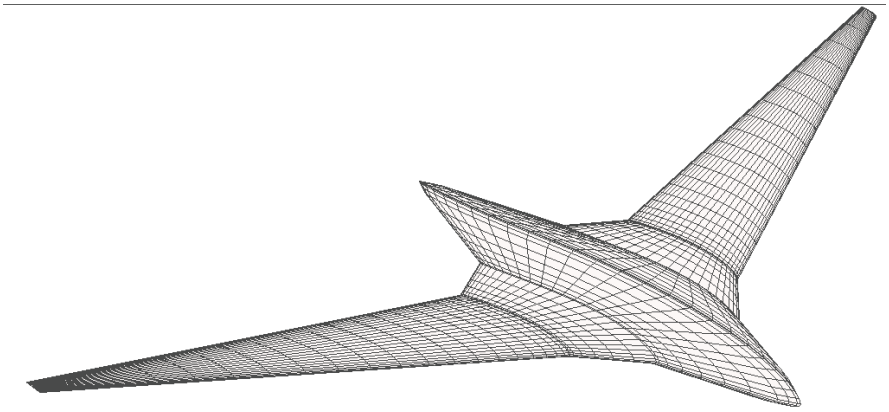

Figure 4.10: BWB mark 2 panelling.

The geometric properties of the Mark 2 are shown in table 4.8.

Table 4.8: BWB mark 2 properties

Wing Span	=	5,0 [m]
Wing Area	=	3,157 [m^2]
Plane Mass	=	50,0 [kg]
Wing Load	=	15,835 [kg/m^2]
Root Chord	=	2,6 [m]
MAC	=	1,05 [m]
Aspect Ratio	=	7,918
Taper Ratio	=	26,0
Root-Tip Sweep	=	34,294 [$^\circ$]

The same conditions are applied in the analysis, which gives the aerodynamic performance results shown in table 4.9.

Table 4.9: BWB mark 2 aerodynamic performance results

Type 1 (Fixed speed)
3D-Panels
Tilted geometry

	CL = 0.22902
VInf = 50.000 m/s	CD = 0.00837
Alpha = 0.00°	VCD = 0.00595
Mass = 0.000 kg	ICD = 0.00242
XCP = 1.562 m	Cm = -0.06548
YCP = 0.000 m	ICm = -0.06537
ZCP = 0.059 m	VCm = -0.00011

An increase in the lift coefficient of the model can be readily noticed. The total lift

can be calculated in the same way as calculated for the mark 1 (eq. 4.5), obtaining the value given in eq. 4.6.

$$L = 532,7\,[N] = 54,3\,[kg] \tag{4.6}$$

The lift distribution on the BWB Mark 2 can be seen in figure 4.11.

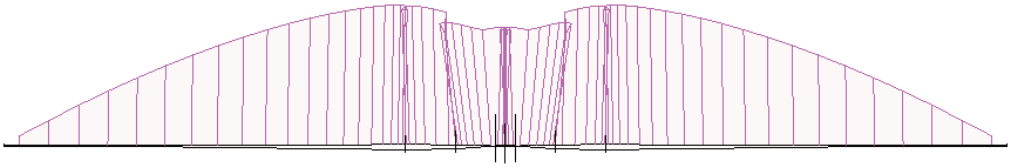

Figure 4.11: BWB Mark 2 lift distribution.

The elliptic distribution over the body is better achieved, but in the center, the reduction in lift is still present. However, the increased span and area of wings allow better lift characteristics.

The pressure distribution on the bottom and upper surface can be seen in figure 4.12.

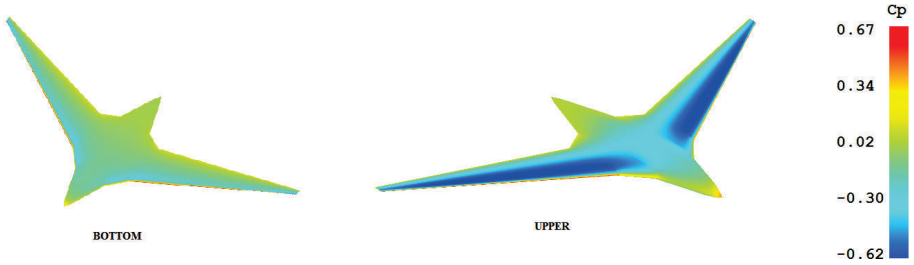

Figure 4.12: Pressure coefficients around the BWB Mark 2.

The pressure difference between the upper and bottom surfaces of the Mark 2 is bigger than that on the Mark 1. This is a direct indicator of the additional lift generated. The effect of the geometric twist can be seen, the pressure increases from the wing root to the tips. A large difference of pressure can be spotted between the core section and the wings, a spanwise secondary flow may appear. However, this flow will not reach the wing tips due to the washout of the wings.

4.3 COMPARATIVE PARAMETERS

Additional comparative parameters between the two models can be seen in figure 4.13, where the polars for both airplanes are presented.

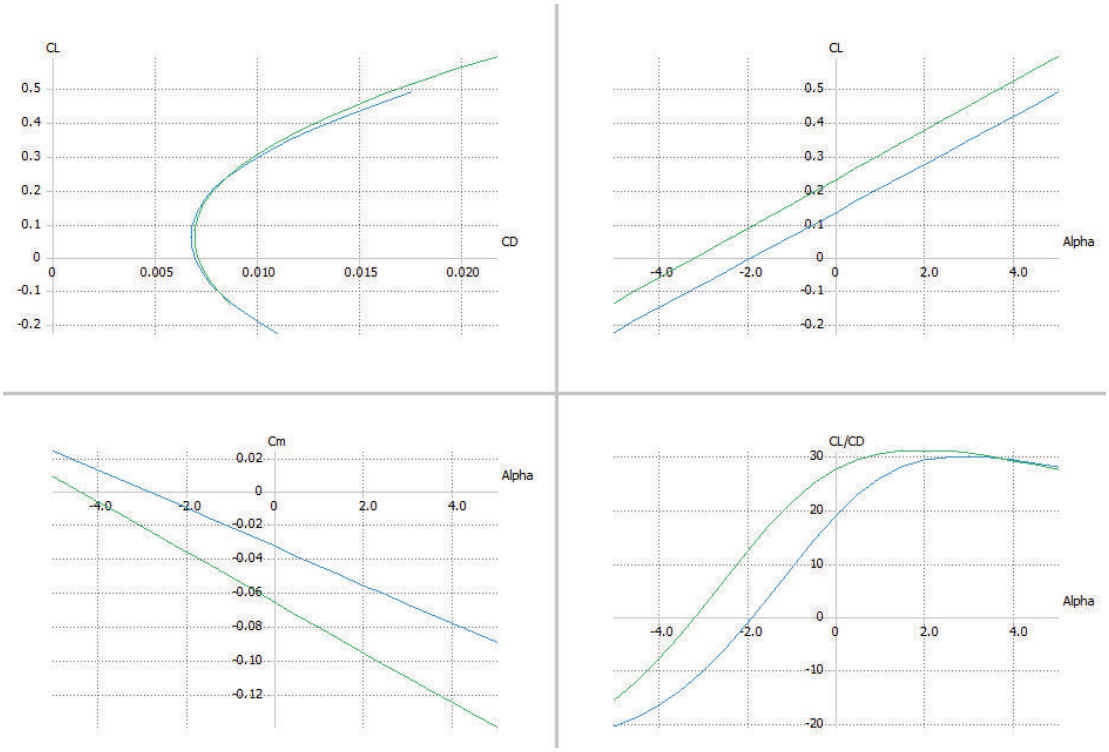

Figure 4.13: Comparative polars and curves between the BWB marks 1 (blue) and 2 (green).

The drag coefficient of both models are similar in the operating conditions. The Mark 2 possesses more lift: an increase of 75% in lift coefficient and 49% in total lift force. Both models have negative slope in the moment coefficient curve, this means both of them are stable. The Mark 2 presents better lift-to-drag characteristics, it offers more lift will nearly the same drag as the Mark 1.

Table 4.10: Comparative chart between the BWB marks 1 and 2

MODEL	Area	X CG	X CP	CL	CD	Total Lift	
	[m^2]	[m]	[m]			[N]	[kg]
BWB Mk 1	3,71	1,281	1,561	0,131	0,00706	358,1	36,5
BWB Mk 2	3,157	1,267	1,562	0,229	0,00837	532,7	54,3

MODEL	Total Drag		Twist	Sweep	MAC	AR	Taper Ratio
	[N]	[kg]	[°]	[°]	[m]		
BWB Mk 1	19,3	2,0	-6	30	1,16	6,739	7,667
BWB Mk 2	19,5	2,0	-6	34	1,05	7,92	26

In table 4.10, it can be seen that the BWB Mark 2 has a reduced surface and a larger aspect ratio, it also has higher lift coefficient. These are the reasons for the increased lift force produced by the Mark 2 ($54,3$ vs $36,5\,[kg]$), with virtually no increase in drag force. The lift-to-drag ratio of the Mark 2 is 28.6. The geometry of the Mark 2 is optimized from the Mark 1. Both models have the center of pressure behind the center of gravity, a stability condition established as necessary in previous sections.

4.4 CFD ANALYSIS

The BWB Mark 2 model obtained in the XFLR5 program will be analysed using ANSYS FLUENT CFD module. The CAD model was constructed using AUTODESK INVENTOR with the coordinates of the airfoils and the parameters set in table 4.7. The module ANSYS MESHING was used to construct the mesh for the analysis. For computational efficiency purposes, only a half-body model will be analysed, using a symmetry plane at mid-span.

The Meshing module was used since it offers an easy but precise meshing process around the complex body of the airframe. Effectively, inflation layers and density boxes are easier and faster to set in comparison to ICEM CFD or Gambit. These methods are used to capture the boundary layer effects around the BWB. Furthermore, the unstructured mesh constructed in the Meshing module reach the quality requirements for Fluent CFD simulation.

The full CAD model analysed is shown in figure 4.14.

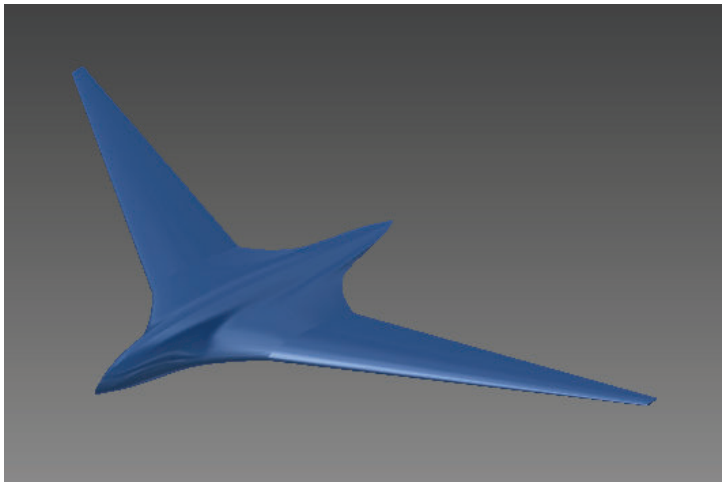

Figure 4.14: CAD model of the BWB Mark 2.

The mesh is built using ANSYS Meshing Tool, with prismatic layers to capture the boundary layer effects, as suggested in ref. (Lanfrit, 2005). The layered prismatic elements are aligned with the flow near the wall boundaries better than tetrahedral elements. The latter type of elements are used typically to envelop other cell types, since their unstructured nature allows them to increase in size while keeping good connectivity between elements. An overall growth ratio of 1.2 is used, a value also used in ref. (Lyu, 2013). A density box is constructed around the model to capture the wake, starting at near half body with a depth of the maximum chord length, the same as used in ref. (ANSYS, 2015).

The obtained mesh contains 4 297 295 elements. A previous analysis of convergence was conducted in order to obtain a mesh-independent solution. The sizing function is based on proximity and curvature, with medium smoothing and slow transition, in order to capture complexity of the NURBS surfaces of the BWB. An inflation of 2 centimetres of height and 13 layers was used to capture the boundary layer effects as suggested in ref. (Lanfrit, 2005).

The statistics for mesh quality is shown in table 4.11.

Table 4.11: Mesh overall quality

Mesh Metric	Skewness	Orthogonal Quality
Min	1.3E-10	0.113
Max	0.904	1
Average	0.236	0.855
Standard Deviation	0.121	0.085

The average values show a skewness of excellent cell quality (below 0.25) (Bakker, 2006) and minimum orthogonality of 0.113, larger than 0.01 as a value set by Fluent as acceptable (*Mesh quality criteria*, 2015).

A cut-plane detail of the mesh around the model is shown in figure 4.15.

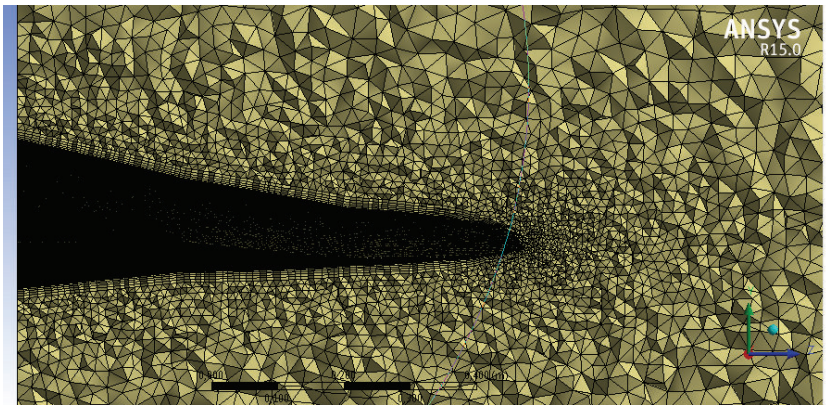

Figure 4.15: 3D mesh detail, cut-plane.

In figure 4.15, the inflation prismatic layers and the increasing size of the mesh elements as they move away from the model can be seen. Both these meshing controls allow to capture the boundary layer effects around the body.

The mesh around the body and in the wake region can be seen in figure 4.16.

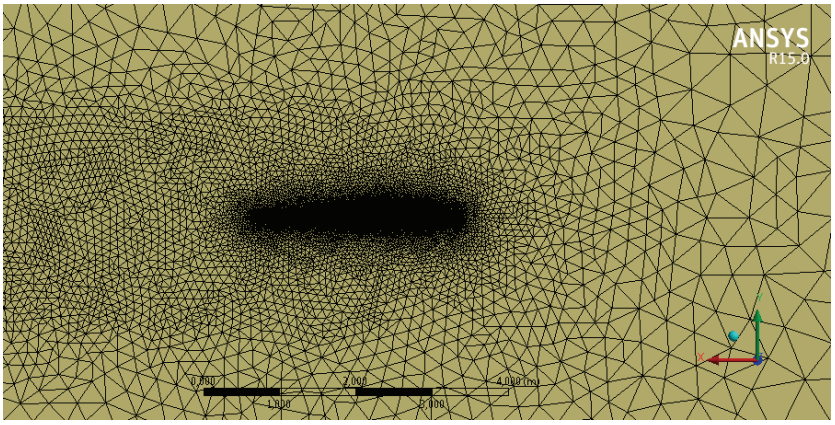

Figure 4.16: 3D mesh.

In figure 4.16, the different sizes of the mesh can be seen. In the right area of the figure, a larger size of the mesh is constructed. This area correspond to the approaching flow from the velocity inlet boundary to the surfaces of the BWB. The properties of said flow are practically non-variant, thus a local smaller size of the mesh would result inefficient.

The analysis conditions are shown in table 4.12.

Table 4.12: CFD analysis conditions

$V_\infty[m/s]$	$\rho_\infty[kg/m^3]$	$\mu_\infty[kg/m.s]$
50	0.5895	$1.561 \cdot 10^{-5}$

The calculation was performed using FLUENT with the turbulence model of Spalart-Allmaras. This RANS model uses a single variable for turbulence prediction, reducing the computational requirements and calculation time at high Reynolds numbers. Effectively, in ref. (Spalart & Allmaras, 1992, p. 17), the S-A model was tested using a RAE 2822 airfoil, obtaining ”solid convergence and mild differences” from experimental results up to 6.5 million Reynolds number. This model was developed in 1992 for aerospace applications with good results in accuracy and convergence for adverse pressure gradients in boundary layers. In FLUENT, the Enhanced Wall Treatment makes the S-A model independent of the near wall y^+ (Spalart & Allmaras, 1992). Further studies such as refs. (Argryopoulos, 2014) and (Walker-Horn, 2015) suggest the one-equation Spalart-Allmaras model for solving flow over airfoils and over aerodynamic bodies.

In a previous section, an analysis of the influence of the boundary layer in the studied BWB was performed, showing that the maximum boundary layer height was not profitable for BLI systems; thus, the analysis of the boundary layer using CFD has not been considered. If these effects were to be studied, the $k-\epsilon$ or $k-\omega$ models would prove more suited. However, in order to reduce the computational resources, the less demanding S-A model is selected for the present work.

The simulation is performed at an angle of attack of 0°. The reference area is set to be 1.579 square meters, as it is the half body area used in simulation. The reference length is chosen to be the mean aerodynamic chord of 1.05 meters. These reference values are used by the program to compute the aerodynamic coefficients.

The convergence was obtained at around 550 iterations, being the continuity residual the largest. The scaled residuals are shown in figure 4.17.

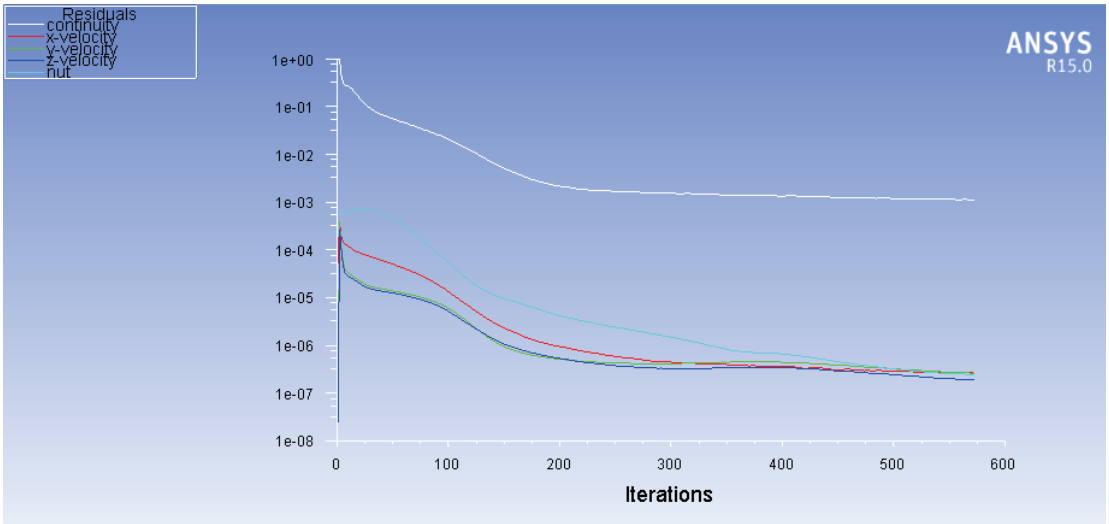

Figure 4.17: Scaled residuals of the CFD simulation.

The reported forces and coefficients for the half body simulation are shown in table 4.13.

Table 4.13: Reported results

Result	Force [N]	Coefficient
Lift	242.3	0.209
Drag	5.4	0.005

These results are only for the half body and to find the total forces on the entire BWB,

the forces on table 4.13 must be doubled. However, the coefficients are invariant since they are non-dimensional. The total forces are shown in table 4.14.

Table 4.14: CFD results for the entire BWB

Result	Force [N]	Force [kgf]	Coefficient
Lift	484.6	49.5	0.209
Drag	10.8	1.1	0.005

A comparison between the coefficients obtained with the XFLR5 analysis method (3D panels) and via CFD (Spalart-Allmaras turbulence model) are shown in table 4.15. The value of the lift coefficient is 8.7% smaller to that obtained in the XFLR5 (table 4.10). However, the values presented in table 4.14 are the result of a preliminary CFD analysis which can be improved with a structured mesh and using a better turbulent model as $k-\epsilon$, $k-\omega$ STLL or LES.

Table 4.15: Comparison of results: lift and drag coefficients

	XFLR5	CFD	Difference
Lift	0.229	0.209	8.73 %
Drag	0.0084	0.005	40.48 %

The distributions of the pressure coefficients around the upper and bottom surfaces are shown in figure 4.18.

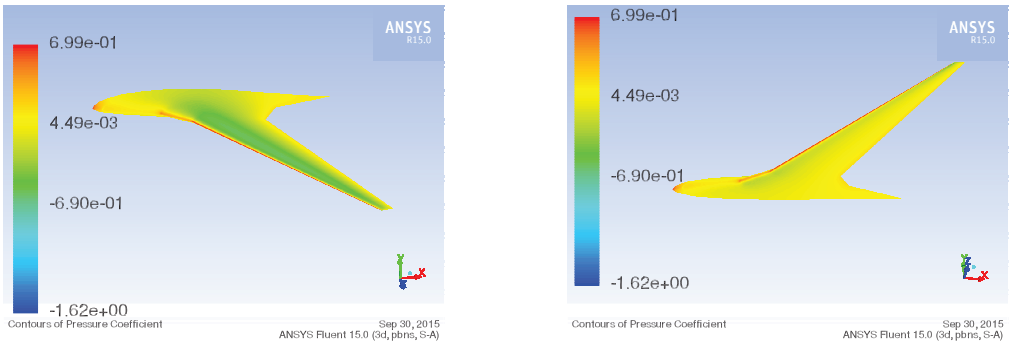

Figure 4.18: Pressure coefficients on the upper (L) and bottom (R) surfaces of the BWB.

The pressure coefficients on the upper surface are lower than those on the bottom surface, generating lift over all the BWB. The reflex effect of the MH45 and TL54 airfoils can be also seen, the pressure coefficient is lower near the trailing edge of

the center body and the wing root. These are the zones that provide a better longitudinal stability to the BWB configuration.

The isobaric lines on both upper and bottom surfaces can be seen in figure 4.19.

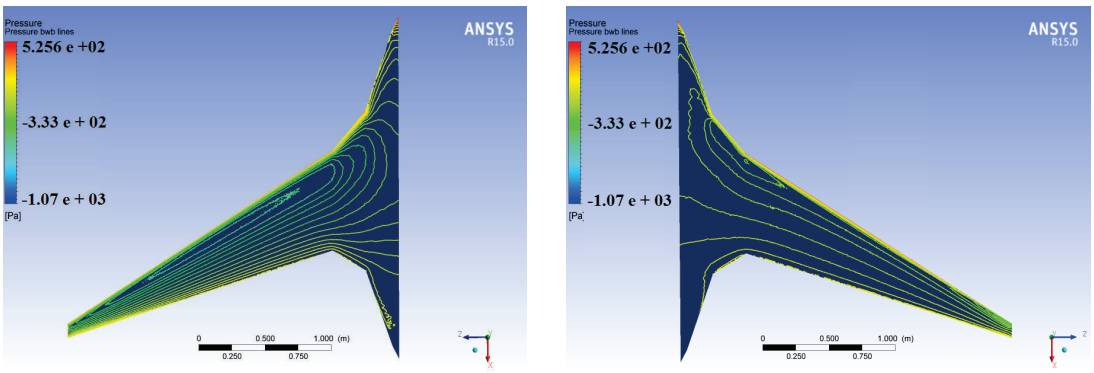

Figure 4.19: Pressure lines on the upper (L) and bottom (R) surfaces of the BWB.

The streamlines of the flow over the BWB can be seen in figure 4.20.

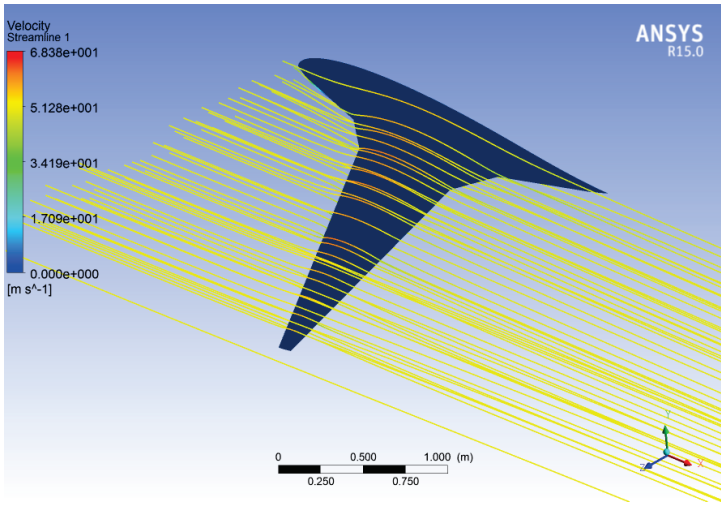

Figure 4.20: Streamlines over the BWB.

Figure 4.20 shows that the streamlines of the attached flow around the body do not present separation. However, these results are given due to the selected turbulence model and the steady state solution. Furthermore, the flow at the wing root show a decrease in velocity magnitude, which can lead to separation at higher angles of attack. This is the effect of the aerodynamic twist of the airfoils. Effectively, a 2° angle of attack was set for the wing at the transition in order to ensure stall at this section and not at the wing tips. This effect is more visible in figure 4.21.

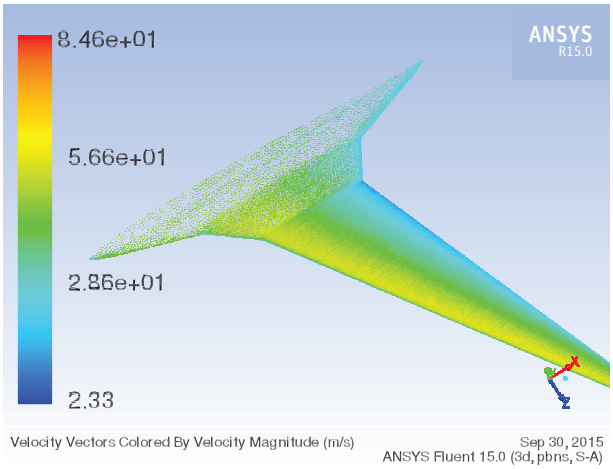

Figure 4.21: Velocity vectors on the upper surface of the BWB.

The validation of the results of the CFD simulation was the main issue in the development of this work. Effectively, the little amount of specialized information about the CFD settings and results for similar applications made the validation process difficult. However, in ref. (Thompson, 2011), the dynamic pressure contours around the upper surface of the BWB therein developed were shown for different angles of attack, including stall. These served as the main comparison point to validate the behavior of the BWB Mark 2 at different angles of attack, obtained via CFD.

Another comparison was performed, one between the lift-to-drag ratio of the different sections of the BWB and the 2D results of the corresponding airfoils. However, the effects of the flow around the airfoils are very different from those of the flow around a finite section of the body (increased drag particularly). Effectively, the center (MH45 airfoil)and the wing root (TL 54 airfoil) sections are merely 25 centimeters wide. Furthermore, the blending of the different airfoils, are responsible of the variation of the characteristics of the flow around the body, making them vary significantly form the two-dimensional flow around a given airfoil. For these reasons, this comparison would not result profitable to validate the CFD results.

In the future, an experimental analysis must be performed, using a 3D model in a wind tunnel. These results must be compared to those obtained using the CFD simulations developed in this work.
The dynamic pressure contours around the upper surface of the BWB at different angles of attack are shown in figure 4.22.

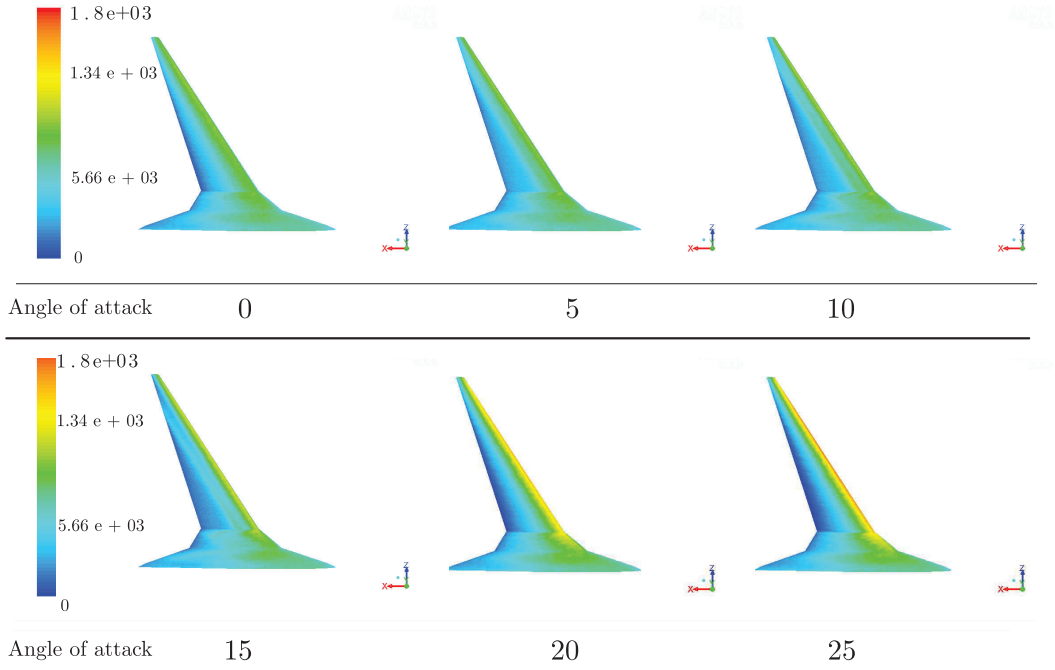

Figure 4.22: Dynamic pressure contours on the upper surface.

The lowest values of the dynamic pressure (deep blue) correspond to the zones of low velocity, i.e. where separation occurs. The dynamic pressure decreases from the trailing edge to the leading edge as the angle of attack increases. At an angle of attack of 20°, the lowest dynamic pressure is close to zero, at the trailing edge of the wing root. This shows the stall tendency of the aircraft near 20°. Furthermore, the stall begins at the root of the wing, where the separation of the boundary layer is evident. This is expected since the local angle of attack of the NACA 2412 airfoil at the wing root is higher than that at the rest of the BWB (aerodynamic twist). In ref. (Thompson, 2011), this tendency can also be seen, along with the evidence of the reverse flow. In the present thesis, the reverse flow was not evident, mainly due to the model used for CFD calculation. Effectively, the Spalart-Allmaras model does not predict boundary layer and separation effects as the $k-\epsilon$ or $k-\omega$ models used in ref. (Thompson, 2011) and (Lyu, 2013).

Anyhow, the overall trend of the results obtained in the present thesis and those found in ref. (Thompson, 2011) are very similar, which means that this thesis offers a good preliminary simulation process. However, as mentioned before, experimental results must be obtained and compared to the milestones set in this thesis.

5 CONCLUSIONS AND RECOMMENDATIONS

5.1 CONCLUSIONS

A baseline configuration of a blended wing body (BWB) airframe for an unmanned aerial vehicle (UAV) has been designed. This aircraft has profited from the blending of aerodynamic profiles to generate high lift capabilities (around 50 kg) with low drag. The BWB herein obtained can be used in the future for applications in agriculture, surveillance, medicine or cartography in Ecuador.

The design and longitudinal stability analysis of a BWB airframe for UAVs used in agriculture, surveillance, medicine and/or cartography has been conducted in the present work. The operating conditions (altitude, speed, payload...) established for the 2D aerodynamic performance and longitudinal stability analysis were obtained by studying those of existent UAVs used in similar applications. A high fidelity tool (CFD) was then used to assess the 3D effects around the BWB.

The selected airfoils offer a good starting point for the optimization of this system. Effectively, the MH45 reflex airfoil has good stability (low moment coefficient) with low drag and lift. This type of airfoil is well suited for the center of the body, where a large chord is needed. The NACA 2412 airfoil offers high lift and low drag capabilities but it has higher moment coefficients. These characteristics are suited for the wings. The characteristics of the TL54 airfoil are sort of a mid-point between the NACA 2412 and the MH45 airfoils, which makes it ideal for the transition section. These criteria must be applied in the optimization of the BWB. However, the use of different airfoils may result in better performance and stability. There are in fact self-stabilizing airfoils that can be used for a future BWB configuration, such as the Liebeck or EP airfoils.

The baseline configuration designed in this thesis has been obtained by following a simplified methodology extracted from the diverse and more specialized literature. The design process applied in this thesis is similar to the processes employed by various research centres, where thorough tests validated both the final designs and the design processes. The CFD modeling of the BWB in this thesis was performed following the criteria derived from the available computational and experimental data for BWB and aircraft design around the world. The obtained results were then compared satisfactory with those obtained via CFD in a similar work (ref. (Thompson, 2011), particularly the dynamic pressure distribution around the BWB. The BWB de-

sign and simulation processes conducted in this thesis can be assumed to be valid.

Even though the design process and the final configuration herein have been validated, this work is only a preliminary configuration of the entire aircraft and thus, further refinements and changes must be made. Effectively, this work conducted a preliminary analysis which intended to capture and develop a method suitable for the design of BWB airframes used in agriculture, surveillance, medicine or cartography. Only the longitudinal stability analysis of the 3D body has been conducted as it has been selected as the main stability criteria for this preliminary analysis. Roll and yaw stability has not be studied, but should be analysed in the future. The application of Thrust Vectoring and the addition of control surfaces can be selected in the future to enhance overall stability. The propulsion system for this aircraft has not been considered; merely an approach to the application of a BLI system has been presented. Additional propulsive solutions were not considered since this preliminary work focusses on the airframe development, not on the propulsive solutions. The adding of these different components to the aircraft will change the center of gravity of the airplane, affecting stability. Furthermore, when installing the propulsion system on the BWB, the lifting surfaces will be troubled, producing a lift reduction and an increase of drag. These changes must be considered for further analysis.

The airframe design is a multidisciplinary process, where different areas of knowledge are applied (aerodynamics, thermodynamics, control systems, among others). A methodology for the aerodynamic discipline has been established, using computational packages such as XFOIL, XFLR5, ANSYS and INVENTOR. However these software tools offered a major advantage for the design process and simulation, they do not encompass the whole spectrum of tools required for the UAVs design process.

5.2 RECOMMENDATIONS

Due to low computational resources available at the time of the development of the thesis, the selection of the model was made in basis of efficiency and calculation requirements. The Spalart-Allmaras turbulent model offers high convergence characteristics with low computational requirements, which makes it recommended for preliminary and relatively fast calculations.

This thesis has contributed by generating a design space for BWB airframes from the aerodynamic perspective, which could be used in UAVs in agriculture, medicine,

surveillance and other uses. However, this subjects requires the expertise of various engineering fields such as automatic control, propulsion and auxiliary systems and equipment. Therefore, a multidisciplinary team is necessary to conduct research and development tasks for UAVs.

The present work developed a computational model of a BWB for the established conditions. In the design process, this thesis utilized a high fidelity tool to assess the 3D effects that other airfoil assessment tools provided. However, experimental set ups are required in order to compare the experimental results with the CFD results obtained in this thesis.

During the development of this thesis, an issue was encountered in the blending process of the airfoils. The complex profiles of the airfoils, particularly in the reflex airfoils, are responsible of the generation of even more complex surfaces on the BWB. These surfaces present a problem when coupling the constructed geometry to the meshing tool. As a solution, these surfaces must be generated in the meshing software, not in the CAD. Furthermore, the mesh around these surfaces should be set with medium smoothing and slow transition. The blending of airfoils also represent an issue during the panelling process in the XFLR5 program. If the panels are not aligned in the transitions, large errors may be therein encountered. To fix this issue, the same number of panels in the chordwise direction must be set for the different airfoils.

A thorough analysis of the airfoils to be used in a BWB must be performed first-hand. However, some concepts and recommendations about airfoil selection were established throughout this work. Reflex airfoils are optimal for the center body section since they provide low pitching moment and low drag with large chord lengths. Airfoils with high lift and lift-to-drag ratio at a wide range of angles of attack (such as the NACA airfoils) are best suited for the wings. Self-stabilizing airfoils (such as EP or Liebeck airfoils) may be also used in order to stabilize the BWB.

The use of open source programs such as XFOIL and XFLR5 are recommended for the baseline design since they offer accurate solutions with very little calculation time compared to CFD.

In the meshing process, an inflation layer of the same height as the maximum boundary layer thickness is recommended to capture the boundary layer effects.

The BLI system integration was found not to be suitable for this aircraft configuration; however, there are other solutions that may be applied in the future, such as the propulsive wing. This configuration uses cross-flow fans distributed in a spanwise direction in order to ingest a larger amount of the flow around the body, which causes similar effects to those from a BLI system.

The implementation of control surfaces and control methods must be studied in the future. There are innovative solutions that involve multidisciplinary teams, such as the development of artificial intelligence and/or fuzzy logic control systems.

REFERENCES

1. Abbot I. H., e. a. (1945). *Summary of airfoil data* (Report No. 824). National Advisory Committee for Aeronautics NACA. Retrieved from http://ntrs.nasa.gov/archive/nasa/casi.ntrs.nasa.gov/19930090976.pdf
2. Abbot I.H., V. D. A. E. (1959). *Theory of wing sections* (2nd ed.). New York: Dover Publications, INC.
3. *Airfoil tools.* (2015). Web Page. Retrieved from http://airfoiltools.com/airfoil/details?airfoil=naca2412-il
4. Anderson Jr., J. D. (1991). *Fundamentals of aerodynamics* (2nd ed.; McGraw-Hill, Ed.). McGraw-Hill Series in Aeronautical and Aerospace Engineering.
5. ANSYS. (2015, January). Ansys icem cfd tutorial manual (16.0 ed.) [Computer software manual].
6. Argryopoulos, C. (2014). Recent advances on the numerical modelling of turbulent flows. *ScienceDirect*. Retrieved from http://www.sciencedirect.com/science/article/pii/S0307904X14003448suggesttheone-
7. AUVSI. (2013). *The economic impact of unmanned aircraft systems integration in the united states*. Author.
8. Baier, H. (2015). *Modeling and control for a blended wing body aircraft a case study* (1st ed.; M. K. A. Schirrer, Ed.). Springer.
9. Bakker, A. (2006). Applied computational fluid dynamics. In (chap. 7, Meshing). Fluent, Inc.
10. Blanks, M. (2014). Uas in agriculture. In *Unmanned aircraft systems.*
11. Bradley, K. (2004, September). A sizing methodology for the conceptual design of blended-wing-body transports. *NASA*(CR-2004-213016).
12. Calero, J. (2014). *En ecuador se construyen aeronaves no tripuladas.* Web Article. Retrieved from http://www.ecuadoracolores.com/ed2014_ene/pages/nac01.html
13. Creech, G. (2010, September). *Back in the air: X-48b resumes flight tests at nasa dryden.* Retrieved from http://www.nasa.gov/centers/dryden/status_reports/X-48B_status_09_21_10.html
14. Deperrois, A. (2013). Xflr5 v6.02 guidelines [Computer software manual].
15. Drela, M. (1989). Xfoil: An analysis and design system for low reynolds number airfoils. *AIAA*.
16. Drela, M. (2001). Xfoil 6.94 user guide [Computer software manual].
17. Dynamic Flight, I. (2002, December). *Airfoils in general.* Figure. Retrieved from http://www.dynamicflight.com/aerodynamics/airfoils/
18. ElUniverso. (2014, November). *A fin de año vence plazo para drones fabrica-*

dos en ecuador. Web Article. Retrieved from http://www.eluniverso.com/noticias/2014/11/09/nota/4199391/drones-fabricacion-nacional

19. Felder, J. (2011, January). An examination of the effect of boundary layer ingestion on turboelectric distributed propulsion systems. *AIAA*, *49*(300).
20. Gundlach, J. (2011). *Designing unmanned aircraft systems: A comprehensive approach* (2nd ed.; Schertz, Ed.). Amer. Inst. of Aeronautics.
21. Houghton, P. C. S. V. D., E.L.; Carpenter. (2013). *Aerodynamics for engineering students* (6th ed.; Butterworth-Heinemann, Ed.). Elsevier.
22. Kim, M.-S., H; Liou. (2013, January). Flow simulation of n3-x hybrid wing-body configuration. *AIAA*, *51*(0221).
23. Kuntawala, N. B. (2011). *Aerodynamic shape optimization of a blended-wing-body aircraft configuration* (Masters of Applied Science, Graduate Department of Aerospace Engineering). University of Toronto.
24. Lanfrit, M. (2005, February). *Best practice guidelines for handling automotive external aerodynamics with fluent.* Retrieved from https://drive.google.com/file/d/0B9w0rrFpsUb3d1YydGpDYW9ReTg/edit
25. LaRepública. (2015, June). *Correa dice que ecuador y bielorrusia producirán juntos aviones no pilotados.* Web Article. Retrieved from http://www.larepublica.ec/blog/internacional/2015/06/28/correa-dice-que-ecuador-y-bielorrusia-produciran-juntos-aviones-no-pilotados/
26. Liebeck, R. H. (2004, Jan-Feb). Design of the blended wing body subsonic transport. *AIAA*, *41*(1), 10-25.
27. Lyu, J., Z.; Martins. (2013, December). Aerodynamic design optimization studies of a blended-wing-body aircraft. *AIAA*. Retrieved from http://mdolab.engin.umich.edu
28. Marzocca, P. (2003). Document. Retrieved from http://people.clarkson.edu/~pmarzocc/AE429/The%20NACA%20airfoil%20series.pdf
29. *Mesh quality criteria.* (2015). Retrieved from http://www.cfd-online.com/Forums/ansys-meshing/82122-mesh-quality-criteria-icem.html
30. Mulder, e. a., J.A. (n.d.). *Flight dynamics.* Summary.
31. Mulder, e. a., J.A. (2007, February). *Flight dynamics.* Lecture Notes.
32. Paspuel, W. (2014, December). *La tecnología de los drones también llegó al agro.* Web Article. Retrieved from http://www.elcomercio.com/actualidad/tecnologia-drones-plantaciones-agricultura-ecuador.html
33. Plas, A. (2006). *Performance of a boundary layer ingesting propulsion system* (Unpublished doctoral dissertation). Massachusetts Institute of Technology.
34. *Propulsive wing technology.* (2015). Retrieved from http://www.propulsivewing.com/technology.shtml

35. Protter, J. C. B., M.H.; Morrey. (1970). *College calculus with analytic geometry* (Addison-Wesley, Ed.).
36. Roskam, E., J.; Chuan-Tau. (1997). *Airplane aerodynamics and performance* (1st ed.). DARcorporation.
37. Siegmann, H. (2015a, March). *Aerodesign.* Web Page. Retrieved from http://www.aerodesign.de/profile/profile_s.htm#tl54
38. Siegmann, H. (2015b, March). *Aerodesign.* Web Page. Retrieved from http://www.aerodesign.de/english/profile/profile_s.htm#mh45
39. Smith, H. (2000). College of aeronautics blended wing body development programme. In *Icas 2000 congress.*
40. Spalart, P. R., & Allmaras, S. R. (1992). A one equation turbulence model for aerodynamic flows. *AIAA*(92 0439).
41. Thompson, J. F. M. A.-M. S. D. D. G. F., D.J.;Feys. (2011). The design and construction of a blended wing body uav. In *49th aiaa aerospace sciences meeting including the new horizons forum and aerospace exposition.* AIAA.
42. Valencia, J. A. W. H. V., E.; Cisneros. (2015). Parametric study of a distributed propulsion system with boundary layer ingestion for unmanned aerial vehicles used for agriculture and mapping in the andean zone.
43. Walker-Horn, A. (2015, August). *3d transonic flow over a wing.* Retrieved from https://confluence.cornell.edu/display/SIMULATION/3D+Transonic+Flow+Over+a+Wing+-+Model+Setup
44. White, F. M. (1998). *Fluid mechanics* (4th ed.). McGraw-Hill.

APPENDIX A ATMOSPHERIC PROPERTIES

The atmosphere is a gaseous mix composed of oxygen (21%), nitrogen (78%), water vapour and other gases (1%). It behaves and can be modelled as a homogeneous ideal gas, which allows its properties to be accurately predicted via the perfect gas law, also known as the equation of state, this is given in equation A.1 (Roskam, 1997, p. 3).

$$p = \rho\, g\, R\, T \tag{A.1}$$

Where:
p: Atmospheric pressure
ρ: Air density
g: Acceleration of gravity
$R = 53,55[ft/R] = 29,26[m/K]$: Dry air gas constant
T: Absolute temperature

The atmosphere is commonly divided in four regions according to the altitude over sea-level ground. A schematic division of it can be seen in figure A.1. In each region, the atmospheric properties (air density, viscosity, pressure and else) can be found, however, for subsonic aircraft, only the troposphere and stratosphere are relevant (Roskam, 1997, p. 5).

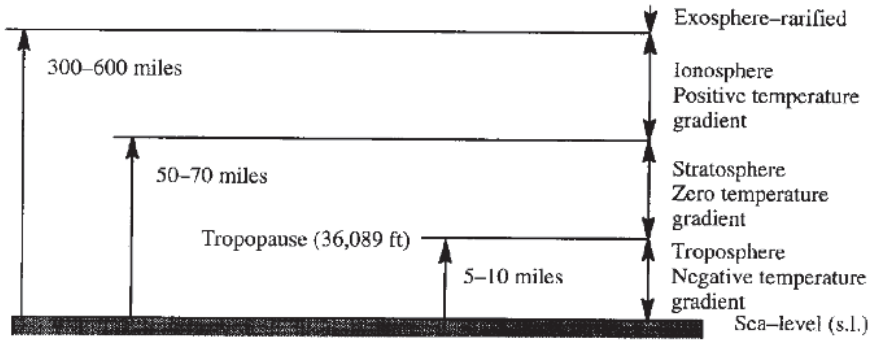

Figure A.1: The four regions of the atmosphere (Roskam, 1997, p. 5).

For an altitude below the tropopause, i.e., below $11000[m]$ or $36089[ft]$, the temperature drop a is constant, and temperature at any given altitude can be calculated from

sea-level conditions given in equations A.2a to A.2d.(Roskam, 1997, p. 5).

$$g_0 = 32.17[ft/s^2] = 9.806[m/s^2] \tag{A.2a}$$
$$p_0 = 29.92[inHg] = 101325[N/m^2] \tag{A.2b}$$
$$T_0 = 59°F = 518.7R = 15°C = 288.2K \tag{A.2c}$$
$$\rho_0 = 1.225[kg/m^3] \tag{A.2d}$$

The temperature can be computed via equation A.3. Above the tropopause, the temperature remains constant equal to $-57°C$ (Roskam, 1997, p. 5).

$$T = T_1 + a(h - h_1) \tag{A.3}$$

Where:
$a = -0.00356616[°F/ft] = -0.0065[K/km]$: lapse rate of the atmosphere
T_1: reference temperature at altitude h_1
h_1: reference altitude

There are several non dimensional parameters and relations established in order to obtain all the remaining properties of air as a function of the evaluated altitude h. These formulations apply for temperature, pressure, density, dynamic viscosity and speed of sound (Roskam, 1997, p. 6, 20, 38).

$$\frac{T}{T_0} = \theta = 1 - \frac{ah}{T_0} \tag{A.4}$$
$$\frac{p}{p_0} = \delta = \theta^{-\frac{1}{aR}} \tag{A.5}$$
$$\frac{\rho}{\rho_0} = \sigma = \theta.\delta = \theta^{(-\frac{1}{aR}-1)} \tag{A.6}$$
$$V_a = 340.3\sqrt{1 - 2.255 * 10^{-5} * h} \qquad h \text{ in meters} \tag{A.7}$$
$$\mu = (1.458 * 10^{-6}) * T^{3/2} * \left(\frac{1}{T + 110.4}\right)[N.s/m^2] \qquad T \text{ in Kelvins} \tag{A.8}$$

These relations will be used in a subsequent section in order to evaluate the flow around a studied aerodynamic body that will be tested at different operating conditions. Such conditions will primarily vary in altitude, hence the importance of obtaining explicit relations of air properties at different altitudes.

APPENDIX B NUMERICAL METHODS APPLIED IN AERODYNAMICS

In this subsection, two numerical methods used in aerodynamics are studied, the source panel method and the vortex panel method. The importance of studying these two particular methods is that both are used in the program XFOIL (Drela, 1989, p. 1).

The computational methods studied use two types of known flows, source and vortex. A schematic representation of these can be seen in figure B.1, along with a comparative table showing the velocity field, the velocity potential ϕ and stream function ψ (Anderson Jr., 1991, p.185).

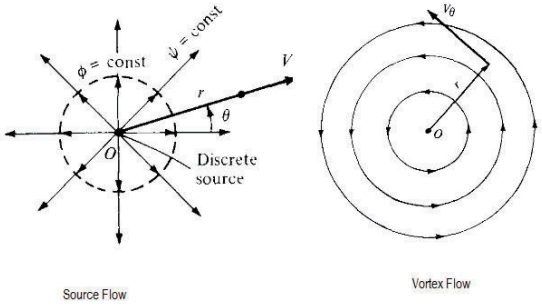

Type of flow	Velocity	ϕ	ψ
Source	$V_r = \frac{\Lambda}{2\pi r}$	$\frac{\Lambda}{2\pi}\ln r$	$\frac{\Lambda}{2\pi}\theta$
Vortex	$V_\theta = -\frac{\Gamma}{2\pi r}$	$-\frac{\Gamma}{2\pi}\theta$	$\frac{\Gamma}{2\pi}\ln r$

Figure B.1: Source and vortex (Anderson Jr., 1991).

B.1 SOURCE PANEL METHOD

The purpose of this method is to obtain the flow characteristics over an arbitrary body. The technique consists in joining an infinite number of source lines side-by-side, forming a source sheet. In figure B.2 is shown the distance s along the source sheet and $\lambda(s)$ the source strength per unit along s. The point P is an arbitrary point at which the velocity potential function is found (Anderson Jr., 1991, p. 220).

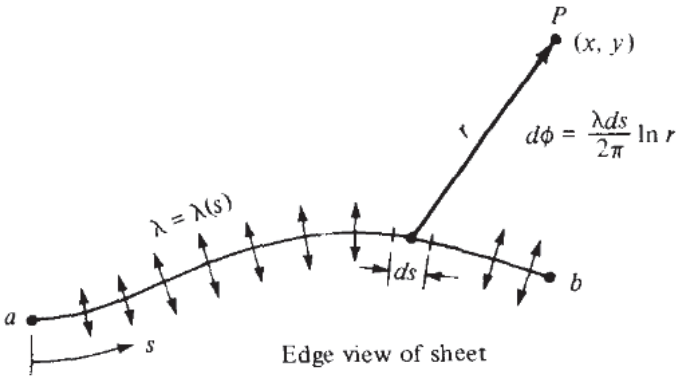

Figure B.2: Source sheet configuration (Anderson Jr., 1991, p. 219).

At point P, each section of the source section induces a differential of velocity potential $d\phi$. The complete velocity potential induced by the entire source sheet at point P, is found by integrating $d\phi$ from a to b, as shown in B.1 (Anderson Jr., 1991, p. 220).

$$\phi(x, y) = \int_a^b \frac{\lambda \, ds}{2\pi} \ln r \tag{B.1}$$

The next stage in the process is to cover the surface of the aerodynamic body with a source sheet where the source strength distribution $\lambda(s)$ is such as the combined action of the uniform flow and the source sheet makes the surface of the airfoil a streamline of the flow. The solution is carried out numerically by approximating the source sheet by a series of n straight panels around the body with a constant λ across the panel but different from one panel to another. Such a distribution is shown in figure B.3. (Anderson Jr., 1991, p. 220).

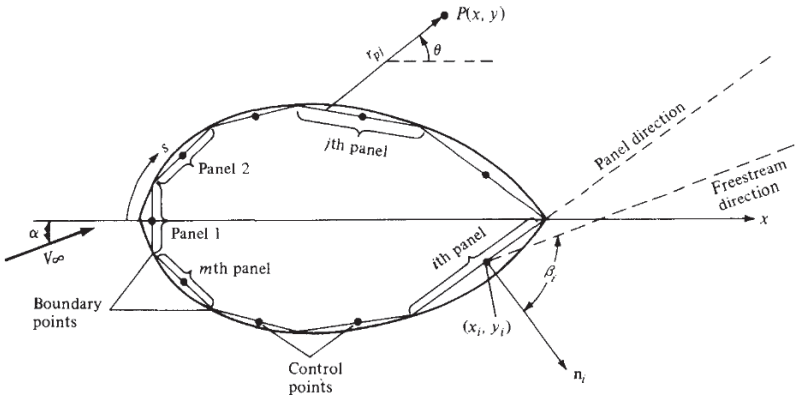

Figure B.3: Panel distribution over the surface of an aerodynamic shape (Anderson Jr., 1991, p. 221).

In order to find the panel strengths λ_j, a control point is defined in the middle of each panel, being (x_i, y_i) the coordinates of the control point of the ith panel. A boundary condition is applied at the control points, stating that the normal component of the flow velocity is zero. The velocity potential induced by all panels at any point is found by adding the induced velocity potential of each panel, given in equation B.1. The induced velocity potential of all panels at the ith control point is given in equation B.2 where r_{ij}, given in equation B.3, is its distance to the jth panel (Anderson Jr., 1991, p. 221).

$$\phi(x_i, y_i) = \sum_{j=1}^{n} \frac{\lambda_j}{2\pi} \int_j \ln r_{ij}\, ds_j \tag{B.2}$$

$$r_{ij} = \sqrt{(x_i - x_j)^2 + (y_i - y_j)^2} \tag{B.3}$$

The normal component to the ith panel of the freestream velocity V_∞ is obtained by inspection of figure B.3, and is defined as (Anderson Jr., 1991, p. 222):

$$V_{\infty,n} = \vec{V_\infty} \cdot \vec{n_i} = V_\infty \cos\beta_i \tag{B.4}$$

The normal component of velocity induced at (x_i, y_i) is the partial derivative of the potential about the normal direction and can be written as (Anderson Jr., 1991, p. 222):

$$V_n = \frac{\partial}{\partial n_i}[\phi(x_i, y_i)] = \frac{\lambda_i}{2} + \sum_{j=2}^{n} \frac{\lambda_j}{2\pi} \int_j \frac{\partial}{\partial n_i}(\ln r_{ij})\, ds_j \tag{B.5}$$

The boundary condition about the normal velocity at the control point states that the

sum of the normal components established at equation B.4 and B.5 must be zero. This condition, given in equation B.7, represents a linear algebraic equation of n unknowns ($\lambda_1, \lambda_2, \ldots, \lambda_n$) with n equations (one equation per panel), which can be solved by numerical methods (Anderson Jr., 1991, p. 223).

$$V_{\infty,n} + V_n = 0 \tag{B.6}$$

$$\frac{\lambda_i}{2} + \sum_{j=2}^{n} \frac{\lambda_j}{2\pi} \int_j \frac{\partial}{\partial n_i}(\ln r_{ij})\, ds_j + V_\infty \cos\beta_i = 0 \tag{B.7}$$

B.2 VORTEX PANEL METHOD

In this part, the complementary numerical method of the source panel method is explained. Both methods are similar in their application, but additional knowledge is required for this technique, the vortex panel method.

The concept of a vortex filament must be introduced, which is defined as a line perpendicular to the page with infinity of vortices of strength γ. By placing side-by-side an infinity number or vortex filaments, a vortex sheet is formed (similar to the source sheet studied in section B.1) (Anderson Jr., 1991, p. 256).

Considering a portion of vortex sheet as shown in figure B.4, the circulation around the dashed path can be written in terms of the tangential and normal velocities and also in terms of the vortex strength, as shown in equation B.8 (Anderson Jr., 1991, p. 258).

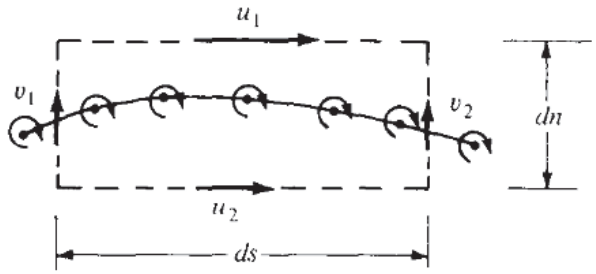

Figure B.4: Velocity representation across a vortex sheet (Anderson Jr., 1991, p. 258).

$$\Gamma = (u_1 - u_2)\, ds + (v_1 - v_2)\, dn = \gamma\, ds \tag{B.8}$$

Furthermore, as the dashed line approaches the vortex sheet, the normal differential approaches to zero and the local vortex sheet strength can be written as the

difference (or the jump) between tangential velocities outside and inside the vortex sheet, as shown in equation B.9 (Anderson Jr., 1991, p. 258)

$$\gamma = u_1 - u_2 \tag{B.9}$$

The strength of a vortex sheet γ varies along the measured distance s. A schematic representation of the vortex sheet is shown in figure B.5 (Anderson Jr., 1991, p. 256).

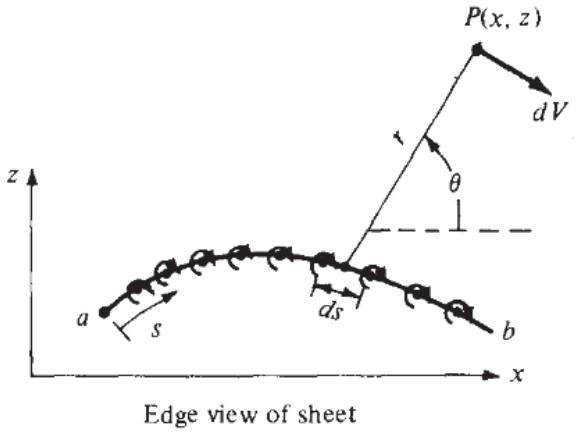

Figure B.5: Edge view of vortex sheet (Anderson Jr., 1991, p. 256).

At any point P having coordinates (x, z), the velocity potential induced by the complete vortex sheet is found by integrating the differential of velocity potential induced by each vortex sheet, as seen in equation B.10. The circulation around the vortex sheet is found using equation B.11 (Anderson Jr., 1991, p. 257).

$$\phi(x, z) = -\frac{1}{2\pi} \int_a^b \theta\gamma \, ds \tag{B.10}$$

$$\Gamma = \int \gamma \, ds \tag{B.11}$$

The present technique consists in wrapping the complete two dimensional body with a vortex sheet and in finding the vortex distribution $\gamma(s)$ such that the body surface becomes a streamline of the flow. This solution, as in the source panel method, is found numerically. The vortex strength is constant across a panel but it varies from one panel to another, giving the vortex panels strengths per unit length γ_1, γ_2, ..., γ_n. Furthermore, the Kutta condition must be satisfied and the midpoint of each panel is a control point at which the normal component of the flow velocity is zero (boundary condition) (Anderson Jr., 1991, p. 284).

The coordinates of the control point of the ith panel are (x_i, y_i), θ_{ij}, given in equation B.12, is the angle between the distance from the control point to the jth panel and the horizontal and the complete velocity potential induced at the ith control point is given in equation B.13 (Anderson Jr., 1991, p. 285).

$$\theta_{ij} = \tan^{-1} \frac{y_i - y_j}{x_i - x_j} \tag{B.12}$$

$$\phi(x_i, y_i) = -\sum_{j=1}^{n} \frac{\gamma_j}{2\pi} \int_j \theta_{ij}\, ds_j \tag{B.13}$$

The component of the freestream velocity normal to the ith control point is given in equation B.14 and the normal component of velocity induced at the same point is given in equation B.15 (Anderson Jr., 1991, p. 285).

$$V_{\infty,n} = V_\infty \cos\beta_i \tag{B.14}$$

$$V_n = \frac{\partial}{\partial n_i}[\phi(x_i, y_i)] = -\sum_{j=1}^{n} \frac{\gamma_j}{2\pi} \int_j \frac{\partial \theta_{ij}}{\partial n_i}\, ds_j \tag{B.15}$$

Applying the boundary condition given in equation B.16, an algebraic equation with n unknowns (the panel strengths) with n equations (one for each control panel) is obtained as shown in

$$V_{\infty,n} + V_n = 0 \tag{B.16}$$

$$V_\infty \cos\beta_i - \sum_{j=1}^{n} \frac{\gamma_j}{2\pi} \int_j \frac{\partial \theta_{ij}}{\partial n_i}\, ds_j = 0 \tag{B.17}$$

The main difference between the panel source method and the vortex panel method is in the application of the Kutta condition, which is at the trailing edge, i.e., $\gamma(TE) = 0$. In figure B.6, two panels are very close to each other (i and $i-1$) and in order to satisfy the Kutta condition, equation B.18 must be introduced in the algebraic system (Anderson Jr., 1991, p. 286).

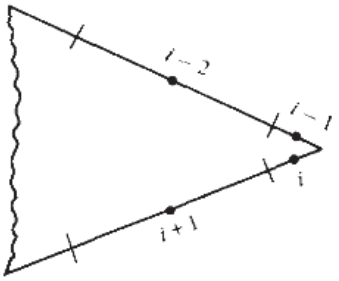

Figure B.6: Vortex panels at the trailing edge (Anderson Jr., 1991, p. 286).

$$\gamma_i = -\gamma_{i-1} \tag{B.18}$$

However necessary it is to satisfy equation B.18, one arbitrary control point must be discarded from the system in order to keep a determined system. By solving the system, all of the vortices strengths are determined and so can the tangential velocities. The tangential velocity inside the body is set to zero (u_2 in figure B.4), and equation B.9 is rewritten so that the local velocities tangential to the airfoil surface are equal to the local values of γ. The total circulation around the airfoil can be readily calculated and so can the lift per unit span as shown in equations B.19 and B.20, respectively (Anderson Jr., 1991, p. 287).

$$\Gamma = \sum_{j=1}^{n} \gamma_j s_j \tag{B.19}$$

$$L' = \rho_\infty V_\infty \sum_{j=1}^{n} \gamma_j s_j \tag{B.20}$$

These numerical techniques calculate the flow characteristics and the lift about an airfoil. The panel vortex method explained in this work is a first order numerical method, since the vortex strength remains constant along the same panel, and can be refined by letting the strength vary inside a panel. Another way to obtain better results is to increase the number of panels and to decrease panel size at leading edge and trailing edge (Anderson Jr., 1991, p. 287). These methods along with viscous and compressible corrections are applied in the XFOIL program, used in following sections (Drela, 1989).

APPENDIX C NAVIER-STOKES AND BOUNDARY LAYER EQUATIONS

The Navier-Stokes equations are a set of equations describing the motion of viscous Newtonian fluids, derived from Newton's second law of motion. The deduction of these equations involve the continuity equations in the three axis (x, y and z) with the addition of body forces caused by viscosity, named shear and normal stresses τ on a differential three dimensional body, as shown in figure C.1 (Anderson Jr., 1991, p. 651).

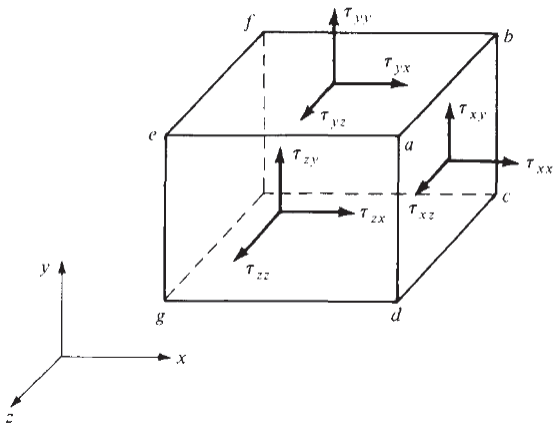

Figure C.1: Shear and normal stresses, effects of viscosity on a fluid element (Anderson Jr., 1991, p. 648).

The momentum equations for a viscous flow in its x, y and z components are given in equations C.1a to C.1c, respectively. These mpnlinear equations are scalar representations of the Navier-Stokes equations which in turn. (Anderson Jr., 1991, p. 654).

$$\rho\frac{Du}{Dt} = -\frac{\partial p}{\partial x} + \frac{\partial \tau_{xx}}{\partial x} + \frac{\partial \tau_{yx}}{\partial y} + \frac{\partial \tau_{zx}}{\partial z} \tag{C.1a}$$

$$\rho\frac{Dv}{Dt} = -\frac{\partial p}{\partial y} + \frac{\partial \tau_{yx}}{\partial x} + \frac{\partial \tau_{yy}}{\partial y} + \frac{\partial \tau_{zy}}{\partial z} \tag{C.1b}$$

$$\rho\frac{Dw}{Dt} = -\frac{\partial p}{\partial z} + \frac{\partial \tau_{zx}}{\partial x} + \frac{\partial \tau_{zy}}{\partial y} + \frac{\partial \tau_{zz}}{\partial z} \tag{C.1c}$$

The concept of bulk viscosity coefficient λ is given in equation C.2 and the dilation of fluid element (compressibility effects) being $\vec{\nabla} \cdot \vec{V}$, the Navier-Stokes equations can be written as shown from equations C.3a to C.3c (Anderson Jr., 1991, p. 654).

$$\lambda = -\frac{2}{3}\mu \tag{C.2}$$

$$\rho\frac{\partial u}{\partial t} + \rho u\frac{\partial u}{\partial x} + \rho v\frac{\partial u}{\partial y} + \rho w\frac{\partial u}{\partial z} = -\frac{\partial p}{\partial x} + \frac{\partial}{\partial x}\left(\lambda\vec{\nabla}\cdot\vec{V} + 2\mu\frac{\partial u}{\partial x}\right) + \frac{\partial}{\partial y}\left[\mu\Big(\frac{\partial v}{\partial x} + \frac{\partial u}{\partial y}\Big)\right] + \frac{\partial}{\partial z}\left[\mu\Big(\frac{\partial u}{\partial x} + \frac{\partial w}{\partial x}\Big)\right] \tag{C.3a}$$

$$\rho\frac{\partial v}{\partial t} + \rho u\frac{\partial v}{\partial x} + \rho v\frac{\partial v}{\partial y} + \rho w\frac{\partial v}{\partial z} = -\frac{\partial p}{\partial y} + \frac{\partial}{\partial x}\left[\mu\Big(\frac{\partial v}{\partial x} + \frac{\partial u}{\partial y}\Big)\right] + \frac{\partial}{\partial y}\left(\lambda\vec{\nabla}\cdot\vec{V} + 2\mu\frac{\partial v}{\partial y}\right) + \frac{\partial}{\partial z}\left[\mu\Big(\frac{\partial w}{\partial y} + \frac{\partial v}{\partial z}\Big)\right] \tag{C.3b}$$

$$\rho\frac{\partial w}{\partial t} + \rho u\frac{\partial w}{\partial x} + \rho v\frac{\partial w}{\partial y} + \rho w\frac{\partial w}{\partial z} = -\frac{\partial p}{\partial z} + \frac{\partial}{\partial x}\left[\mu\Big(\frac{\partial u}{\partial z} + \frac{\partial w}{\partial x}\Big)\right] + \frac{\partial}{\partial y}\left[\mu\Big(\frac{\partial w}{\partial y} + \frac{\partial v}{\partial z}\Big)\right] + \frac{\partial}{\partial z}\left(\lambda\vec{\nabla}\cdot\vec{V} + 2\mu\frac{\partial w}{\partial z}\right) \tag{C.3c}$$

This set of equations (C.3a to C.3c) stand as the complete Navier-Stokes equations for an unsteady, compressible, three-dimensional viscous flow (Anderson Jr., 1991, p. 654). The present work treats with incompressible flow and the Navier-Stokes equation are simplified as shown in equations C.4a, C.4b and C.4c (Houghton, 2013, p. 116).

$$\rho\Big(\frac{\partial u}{\partial t} + u\frac{\partial u}{\partial x} + v\frac{\partial u}{\partial y} + w\frac{\partial u}{\partial z}\Big) = \rho g_x - \frac{\partial p}{\partial x} + \mu\left(\frac{\partial^2 u}{\partial x^2} + \frac{\partial^2 u}{\partial y^2} + \frac{\partial^2 u}{\partial z^2}\right) \tag{C.4a}$$

$$\rho\Big(\frac{\partial v}{\partial t} + u\frac{\partial v}{\partial x} + v\frac{\partial v}{\partial y} + w\frac{\partial v}{\partial z}\Big) = \rho g_y - \frac{\partial p}{\partial y} + \mu\left(\frac{\partial^2 v}{\partial x^2} + \frac{\partial^2 v}{\partial y^2} + \frac{\partial^2 v}{\partial z^2}\right) \tag{C.4b}$$

$$\rho\Big(\frac{\partial w}{\partial t} + u\frac{\partial w}{\partial x} + v\frac{\partial w}{\partial y} + w\frac{\partial w}{\partial z}\Big) = \rho g_z - \frac{\partial p}{\partial z} + \mu\left(\frac{\partial^2 w}{\partial x^2} + \frac{\partial^2 w}{\partial y^2} + \frac{\partial^2 w}{\partial z^2}\right) \tag{C.4c}$$

The dimensional analysis tools can be applied to obtain a non dimensional form of the Navier-Stokes equations. A two dimensional flow is being considered for practical purposes. A set of non dimensional variables are introduced as follows, where the superscript $\prime$ indicates the dimensionless variable, the subscript ∞ stands for reference values (or freestream values) and c is the chord length (Anderson Jr., 1991, p. 659):

$$\rho' = \frac{\rho}{\rho_\infty} \qquad u' = \frac{u}{V_\infty} \qquad v' = \frac{v}{V_\infty} \qquad p' = \frac{p}{V_\infty}$$

$$\mu' = \frac{\mu}{\mu_\infty} \qquad x' = \frac{x}{c} \qquad y' = \frac{y}{c}$$

The Navier-Stokes equation in the x direction (C.1a) for two dimensional flow can be written in terms of the introduced non dimensional parameters as shown in equation C.5 (Anderson Jr., 1991, p. 659).

$$\rho' u' \frac{\partial u'}{\partial x'} + \rho' v' \frac{\partial u'}{\partial y'} = -\frac{1}{\gamma M_\infty^2} \frac{\partial p'}{\partial x'} + \frac{1}{Re_\infty} \frac{\partial}{\partial y'} \left[\mu' \left(\frac{\partial v'}{\partial x'} + \frac{\partial u'}{\partial y'} \right) \right] \tag{C.5}$$

The result of having a non dimensional Navier-Stokes set of equations similar to equation C.5 is very important. Assuming two flows having the same values of specific heats ratio γ, Mach number M_∞ and Reynolds numbre Re_∞ they will have the same coefficients of the derivatives (numerically identical flows). If additionally, two immersed bodies are geometrically similar, both flows will be dynamically similar. This means that the distributions of non dimensional pressure, velocity and so on, will be the same for non dimensional coordinates of the body. This principle is the fundamental reason for the wide use of dimensionless coefficients in aerodynamics (Anderson Jr., 1991, p. 660).

Next, the assumption that the boundary layer is negligible in size comparable to the chord length. The application of Navier-Stokes equation to these boundary layer settings yield the boundary layer equations: continuity equation (C.6a), x momentum equation (eq. C.6b) and y momentum equation (eq. C.6c) and energy (eq. C.6d) (Anderson Jr., 1991, p. 723).

$$\frac{\partial(\rho u)}{\partial x} + \frac{\partial(\rho v)}{\partial y} = 0 \tag{C.6a}$$

$$\rho u \frac{\partial u}{\partial x} + \rho v \frac{\partial u}{\partial y} = -\frac{dp_e}{dx} + \frac{\partial}{\partial y} \left(\mu \frac{\partial u}{\partial y} \right) \tag{C.6b}$$

$$\frac{\partial p}{\partial y} = 0 \tag{C.6c}$$

$$\rho u \frac{\partial h}{\partial x} + \rho v \frac{\partial h}{\partial y} = \frac{\partial}{\partial y} \left(k \frac{\partial T}{\partial y} \right) + u \frac{dp_e}{dx} + \mu \left(\frac{\partial u}{\partial y} \right)^2 \tag{C.6d}$$

The boundary layer equations are nonlinear as the Navier-Stokes but are simpler, hence easier to solve. However, these equations must be calculated via numerical

methods, such as finite-difference techniques, obtaining distributions of wall stress and wall heat trandfer. Boundary conditions must be provided at the wall and at the boundary layer edge (Anderson Jr., 1991, p. 723).

APPENDIX D NACA 2412 EXPERIMENTAL RESULTS

The results obtained with the XFOIL analysis in comparison with those available at (Abbot I. H., 1945) are compared in this section. The analysis carried out in the XFOIL software are as shown in table 3.2. In (Abbot I. H., 1945), the data is obtained using the Langley two-dimensional low-turbulence pressure tunnel(TDT), with a Reynolds number of 6 million.

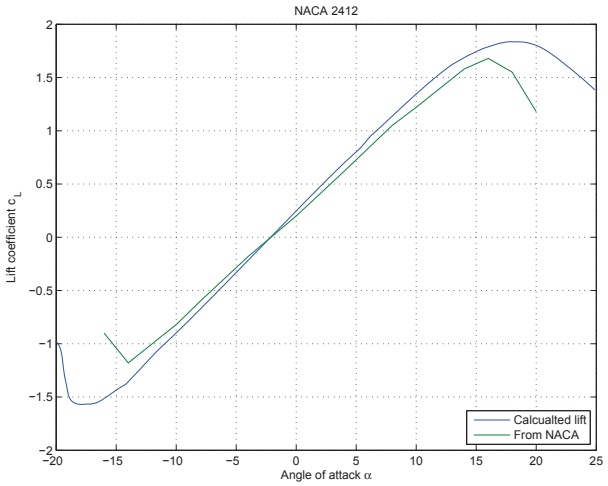

Figure D.1: Lift curve for NACA 2412.

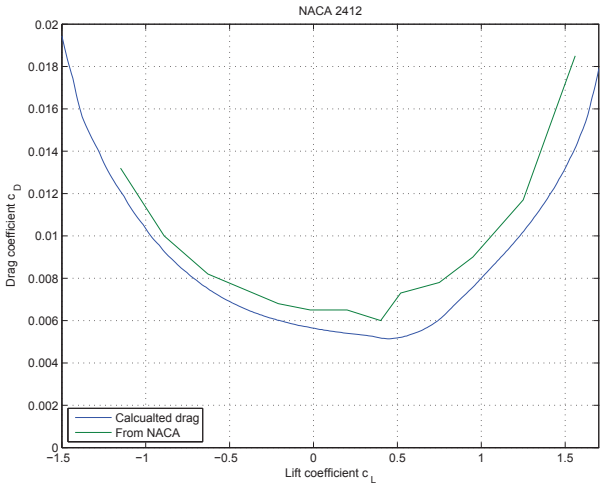

Figure D.2: Drag polar for NACA 2412.

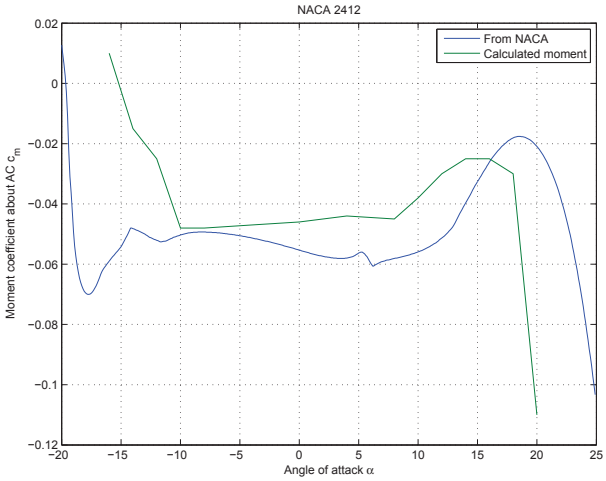

Figure D.3: Pitching moment curve for NACA 2412 at different angles of attack.

The polars differ slightly between the experimental data and the calculated results, mainly due to the different wind velocity used in both analysis. The Reynolds number variation is $300,000$, which leads to different results. Another reason is the use of the Karman-Tsiens compressibility correction in the XFOIL program, which uses a different Mach number than that obtained in the wing tunnel.
However the differences, the behaviour of the different curves is similar, therefore, the data obtained from the XFOIL software are valid for use in this work.

APPENDIX E THE XFOIL PROGRAM

In 1986, Mark Drela, the Head of the Aeronautics and Astronautics Department of the MIT, wrote XFOIL 1.0, a program that would enable to combine the speed and accuracy of high-order panel methods with a fully-coupled viscous/inviscid interaction method (Drela, 2001, p. 4). XFOIL is an interactive program used for the design and analysis of subsonic isolated airfoils. It is made of multiple menu-driven routines allowing the user to perform various tasks such as (Drela, 2001, p. 3):

- Viscous or inviscid analysis of an existing airfoil
- Airfoil design and redesign by specifying a surface speed distribution or geometric parameters
- Airfoil blending
- Drag polar calculation
- Plotting of geometry, pressure distributions and polars

The program code was developed in order to reduce computational requirements and times, thus increasing the design process productivity without loss of accuracy nor precision. It could have taken, in fact, about two hours to calculate a 20-point polar. Also, the analysis method demands for low Reynolds number airfoils (less than 500 000) are severe and the solution algorithm proposed in Xfoil would have been able to handle such demands (Drela, 1989, p. 1).

Xfoil employs an inviscid and viscous methodology and a Karman-Tsien compressibility correction into its calculations (Drela, 1989, p. 1). Such methods will be briefly presented.

E.1 INVISCID FORMULATION

The two-dimensional methodology for inviscid flow consists in the superposition of a freestream flow, a vortex sheet of strength γ on the airfoil surface, and a source sheet of strength σ on the airfoil surface and wake. The airfoil contour and wake trajectory are discretized into flat panels. In figure E.1 a schematic representation of the paneling of the airfoil surface is presented (Drela, 1989, p. 2). The inviscid formulation of the Xfoil program is a more refined method of those described in B (Anderson Jr., 1991), effectively, it is a linear-vorticity stream function panel method (Drela, 2001, p. 5).

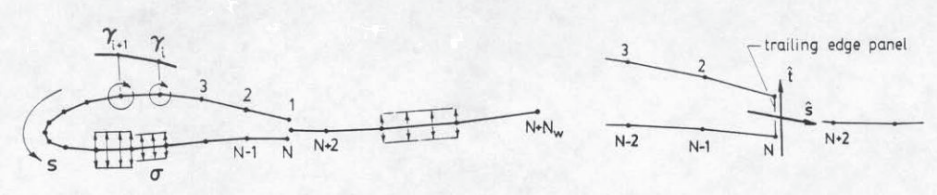

Figure E.1: Panels distribution along airfoil surface and wake (Drela, 1989, p. 2).

The unit stream functions ($\psi^{\gamma+}$, $\psi^{\gamma-}$ and ψ^{σ}) are calculated in terms of the panel's coordinates, obtaining a matrix with coefficients determined via the unit stream functions. The goal is to solve a linear system via Gaussian elimination, for fast processing (Drela, 2001, p. 5). The Kutta condition is added in the linear system (Drela, 1989, p. 4).

E.2 COMPRESSIBILITY CORRECTION

The XFOIL program uses the Karman-Tsien correction to approximately determine the compressible speed q and pressure coefficient C_p form th incompressible flow values q_{inc} and $C_{P,inc}$ by (Drela, 1989, p. 9):

$$C_P = \frac{C_{P,inc}}{\beta + \lambda(1+\beta)C_{P,inc}/2} \tag{E.1a}$$

$$q = \frac{q_{inc}(1-\lambda}{1-\lambda(q/q_\infty)^2_{inc}} \tag{E.1b}$$

where $\beta = \sqrt{1-M^2_\infty}$ and $\lambda = M_\infty 2/(1+\beta)^2$.

E.3 VISCOUS FORMULATION

The viscous formulation of the XFOIL program employs standard compressible integral momentum and energy shape parameters equations and a rate equation for the maximum shear stress coefficient. The fundamental variables governed by the boundary layer equations are the momentum thickness θ, displacement thickness δ^* and the shear stress coefficient C_τ (Drela, 1989, p. 7).

The total velocity at each point on the airfoil surface and wake, with contributions from the freestream, the airfoil surface vorticity, and the equivalent viscous source distribution, is obtained from the panel solution with the Karman-Tsien correction

added. Execution times are quite rapid, requiring a few seconds on a fast workstation for a high-resolution calculation with 160 panels. For a sequence of closely spaced angles of attack (as in a polar), the calculation time per point can be substantially smaller (Drela, 2001, p. 6).

APPENDIX F CFD SIMULATION PROCESS

F.1 GEOMETRY CONSTRUCTION

The geometry of the model was constructed using the ANSYS Design Modeler module, using the coordinates of the different airfoils. These coordinates were scaled to the designed chord length and offset designed in the XFLR5 software.
In the Design Modeler, the far field box surrounding the half body of the aircraft was constructed. A fluid body was set inside the bounding box. The geometry of the BWB was then subtracted using a Boolean operation, to imprint the faces of the BWB to the fluid body.

F.2 MESHING PROCESS

The mesh was built in the Meshing Module, with a proximity and curvature sizing function with medium smoothing, slow transition and overall fine mesh with 20% growth ratio. The boundary maximum boundary layer height was calculated for the entire BWB and then an inflation layer of the same height was stablished around the aircraft. The inflation was set with 13 layers. The complexity of the surfaces of the BWB require fine sizing of the mesh.

F.3 FLUENT SETUP

The material for the fluid body air was set with constant density and viscosity, according to the operating conditions. The turbulence model used was the RANS one equation Spalart-Allmaras model.
The boundary conditions were set as velocity inlet for the inlet section, with velocity magnitude of 50 meters per second. The x and y components were changed to vary the angle of attack of the aircraft. The far field was set as pressure inlet with zero gauge pressure and the velocity components according to the inlet boundary. The outlet was set as pressure outlet and the contour of the BWB was set as a wall boundary condition.
The reference area was set at 1.579 square meters, the half body area used in simulation. The reference length was set at the mean aerodynamic chord of 1.05 meters. The pressure gauge was set at 41060 Pascals, as obtained in the atmospheric properties calculations for the operating conditions.
Monitors for lift, drag and moment coefficients were created, in addition to the main residuals for the Spalart-Allmaras model (continuity, velocity and turbulent kinematic viscosity NUT).

The initialization was performed using the inlet as the reference conditions. The solution was then calculated.

F.4 POST-PROCESSING

The post-processing was performed in Fluent and in the CFD-Post modules of ANSYS. In Fluent, the forces were reported, as well as the pressure coefficients and the dynamic pressure around the BWB. In CFD-Post, the streamlines were made visible, as well as the isobaric lines for both upper and lower surfaces of the BWB.